FINAL REPORT

ON

EFFECTS OF POSITIVE ION IMPLANTATION INTO
ANTIREFLECTION COATING OF SILICON SOLAR CELLS

by

A. E. Middleton, J. W. Harpster, W. J. Collis and C. K. Kim

ELECTRONIC MATERIALS AND DEVICES LABORATORY
Electrical Engineering Department
The Ohio State Univeristy
Columbus, Ohio 43210

June 24, 1971

FINAL REPORT

ON

EFFECTS OF POSITIVE ION IMPLANTATION INTO
ANTIREFLECTION COATING OF SILICON SOLAR CELLS

by

A. E. Middleton, J. W. Harpster, W. J. Collis and C. K. Kim

ELECTRONIC MATERIALS AND DEVICES LABORATORY
Electrical Engineering Department
The Ohio State University
Columbus, Ohio   43210

June 24, 1971

Details of illustrations in
this document may be better
studied on microfiche

TECHNICAL CONTENT STATEMENT

This report contains information prepared by
The Electronic Materials and Devices Laboratory, Elec-
trical Engineering Department, The Ohio State University,
under JPL subcontract. Its content is not necessarily
endorsed by the Jet Propulsion Laboratory; California
Institute of Technology, or The National Aeronautics
and Space Administration.

ABSTRACT

The state of technological development of Si solar cells for highest obtained efficiency and radiation resistance is summarized. The various theoretical analyses of Si solar cells are reviewed. It is shown that factors controlling blue response are carrier diffusion length, surface recombination, impurity concentration profile in surface region, high level of surface impurity concentration (degeneracy), reflection coefficient of oxide, and absorption coefficient of Si.

The theory of ion implantation of charge into the oxide antireflection coating is developed and side effects are discussed.

The experimental investigations were directed at determining whether the blue response of Si solar cells could be improved by phosphorus ion charges introduced into the oxide antireflection coating.

This experimental work included (1) measurements of Centralab n on p solar cells as diodes; (2) preparation of thermally oxidized Si and implantation in the thermally grown oxide followed by evaluation as a MOS capacitor to determine the effect of implanted charge on flat band voltage shift or surface potential: As expected, the MOS characteristics shifted along the voltage axis to larger negative values as the implantation voltage and dosage increased; (3) illuminating the Si solar cell with an affixed transparent electrode and dielectric, across which both positive and negative voltages were applied, which shifted the surface potential in both directions but gave no observable effect on solar cell

iii

efficiency, (4) implanting at 20, 30 and 40 KeV dosages of 10^{12} - 10^{16} phosphorus ions into the oxide at calculated depths of 357, 520, and 682 $\overset{\circ}{A}$, respectively, for the different voltages and measuring the integrated response I-V characteristics and I_{SCC} and V_{OC}, and the spectral response of I_{SCC} from 3950-9000 $\overset{\circ}{A}$ before and after implantation, which revealed that with increasing dosage, I_{SCC} decreased, but also evidence of Si radiation damage and changes in the physical characteristics of the oxide layer were found and (5) determining the spectral response from 3200-6500 $\overset{\circ}{A}$ of the difference in absorption of the oxide layer before and after implantation showing both positive and negative values of this parameter which inferred that the physical characteristics of the oxide had been changed by implantation.

Thus, these investigations yielded inconclusive results concerning the possibility of improving Si solar efficiency by charge introduction into the oxide antireflection coating.

It is concluded, that phosphorus ion implantation as a technique of charge introduction does not fit the requirements for successfully monitoring the charge at the SiO-Si interface in the direction of lowering the Q_{SS} at the interface and because the oxide and Si damage produced by the ion implantation can not be readily annealed out of production solar cells owing to the presence of low melting contacts.

TABLE OF CONTENTS

LIST OF FIGURES

LIST OF TABLES

PURPOSE

Perform a preliminary theoretical study to determine the effects of surface characteristics on the blue response or spectral response of conventional N/P silicon solar cells and outline the physics underlying the approach of ion implantation as a technique to improve the surface recombination characteristics of the silicon solar cell.

Conduct an exploratory investigation of the effect of field and ion implantation introduction of charge into the antireflection covering of production Si solar cells on the surface recombination and spectral and integral response characteristics.

BACKGROUND ON SILICON SOLAR CELLS

The structure of the solar cells to be discussed here is shown in Figure 1. This is a n-on-p (n/p) cell fabricated by diffusing phosphorus donors into a silicon substrate of uniform acceptor doping to form the junction at a depth x_J. Electrical contact is made via an evaporated metal grid pattern on the incident surface and a continuous layer on the back of the cell. Shown also in Figure 1 is the evaporated SiO_2 antireflection coating.

Absorption of photons with energy greater than the bandgap (~ 1.1 eV for Si) creates excess hole-electron pairs. Low level injection conditions prevail for solar intensities and the large junction areas permit a one-dimensional analysis. Drift and diffusive forces determine the motion of the excess carriers to the junction region where the minority carriers are swept across, thus contributing to the short-circuit photocurrent I_{SC}. While excess carriers are created continuously throughout the cell thickness, essentially only those minority carriers generated within an effective diffusion length of the junction region will be collected as photocurrent.

Figure 2 is the equivalent electrical circuit for a solar cell supplying power to an external load R_L. The various series resistances (contact and sheet) have been combined in R_S. Leakage paths around the junction are represented in R_{SH}.

The I_L-V_L relationship is determined from the equation

$$I_L = I_{SC} - I_{oA} [\exp \{q(V_L+I_LR_S)/AkT\} - 1] - (V_L + I_LR_S)/R_{SH} \qquad (1)$$

1
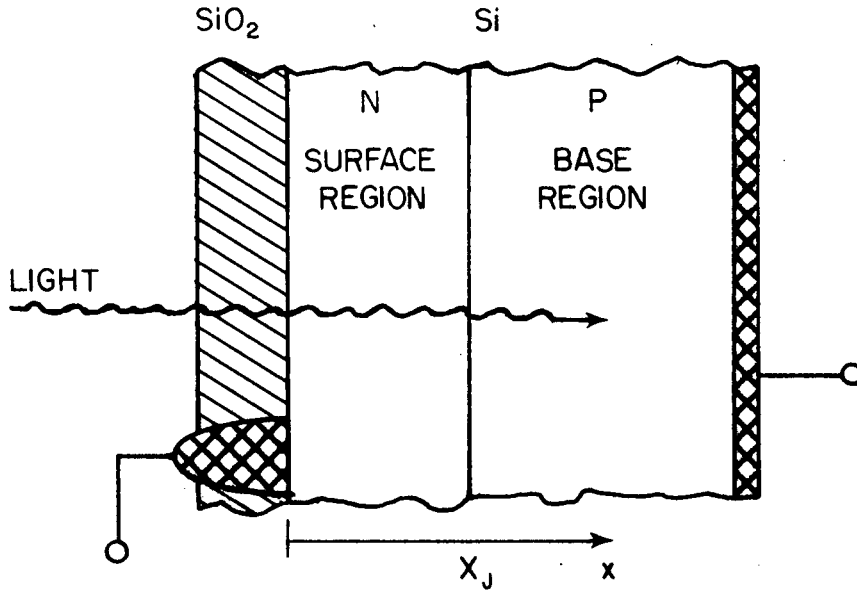
Figure 1. Solar cell structure.
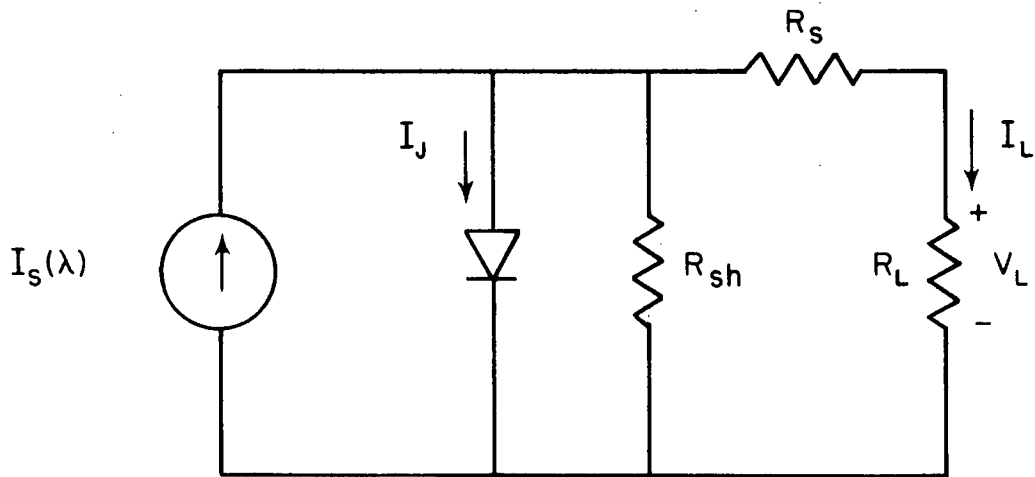
Figure 2. Solar cell equivalent circuit.

Because of the distributed nature of the series resistance R_S, as well as the shunt resistance R_{SH}, an ideal analysis should be performed on an incremental area basis. If R_S is quite high, those cell areas remote from the front surface contacts would be practically open-circuited. Normally the terms involving R_S and R_{SH} may be neglected by letting $R_S \rightarrow 0$, $R_{SH} \rightarrow \infty$. This assumption, of course, is largely dependent upon the optimization of fabrication techniques and device configuration. The second term on the right side of Equation (1) represents that amount of the photocurrent which flows through the p-n junction in parallel with the load. In particular, the factors I_{OA} and A are determined by the recombination mechanism which predominates at the operating cell bias. Recombination in the quasi-neutral regions on either side of the depleted junction is characterized by components of the constant I_{OA} proportional to the square-root of the reciprocal minority carrier lifetime $(\tau^{-1/2})$, and the factor A in the exponential is unity. In the surface layer, the I_{OA} component also has a complex dependence upon the surface recombination velocity. If recombination in the space charge region of the junction predominates due to recombination centers at the intrinsic Fermi level, then I_{OA} is proportional to the reciprocal lifetime (τ^{-1}) and A = 2.

Although the forward junction current will increase more slowly with increasing voltage when A = 2, the magnitude of the I_{OA} factor is much larger than when A = 1. Early predictions of ideal silicon cell efficiency of approximately 22% at 298 °K were based upon the diffusion current dominating the junction behavior (A = 1)[1]. Similar calculations considering only the space charge recombination current indicate an ideal efficiency of

approximately 16%. Mandelkorn, et.al.[2] in discussing their work with some of the first phosphorus-diffused n/p Si solar cells mention the factor A as being a sensitive parameter for optimizing the fabrication process. Typical cell forward characteristics exhibited A values of 1.95. In a study of boron-diffused p/n cells Queisser[3] observed the A value exceeding 3. Apparently the large and varying value of A is common for the boron diffusion cell. It was postulated that this behavior was due to a nonuniform distribution of recombination centers. Queisser demonstrated that precipitation of impurities during the initial cell fabrication may be the cause of the excessive values of A. He heated cells at 825°C in a hydrogen flow and then quickly quenched them to room temperature. The quantity A was found to be reduced to practically 2. At an operating voltage of 0.4-0.5V, n/p production cells today are reported to exhibit values of A lying between 1 and 2. Thus, it appears that any detailed analysis of a Si solar cell operating at maximum efficiency should include both of the components of forward current mentioned above.

The following are considered to be the important design factors which control conversion efficiency of Si homojunction solar cells:

1. Reflectivity

2. Absorption coefficient

3. Surface recombination

4. Impurity profiles

5. Lifetime of minority carriers

6. Surface layer sheet resistance

7. Contact resistance.

Several of these factors will be discussed in the succeeding sections.

4

Combining the absorption coefficient of Si, the solar spectrum and the relatively long minority carrier diffusion lengths leads to the fact that the silicon solar cell is primarily a base-response cell. This can be contrasted with gallium arsenide devices in which, because of the higher absorption coefficient across the active portion of the solar spectrum, the surface region shares an equal role with the base in the overall collection efficiency. In Figure 3, the relative number of solar photons with energies greater than 1.1 eV (AMO) which are absorbed as a function of depth in Si is shown[4]. (It should be recalled that these photons represent about one-half of the total number of photons in the outer space solar spectrum.)

When a solar cell is designed to operate in a hostile radiation environment, a further compromise must be made to minimize the relative change in the characteristics (usually output power) over the useful operating life of the cell. From the results of early space satellite studies and laboratory radiation experiments with high energy electrons and protons (MeV range), three statements can be made: (1) The output of the cell is quite sensitive to radiation, (2) The current decreases much more rapidly than the voltage, and (3) n/p cells are more resistant to radiation degradation than p/n cells. By observing the spectral response of a cell before and after irradiation, it has been determined that the initial decay in output is due to a decrease in minority carrier diffusion length, L, in the base region. The relationship between L after bombardment by a particle flux ϕ and the prebombardment diffusion length L_O is

$$L^{-2} = L_O^{-2} + K\phi \qquad (2)$$

5
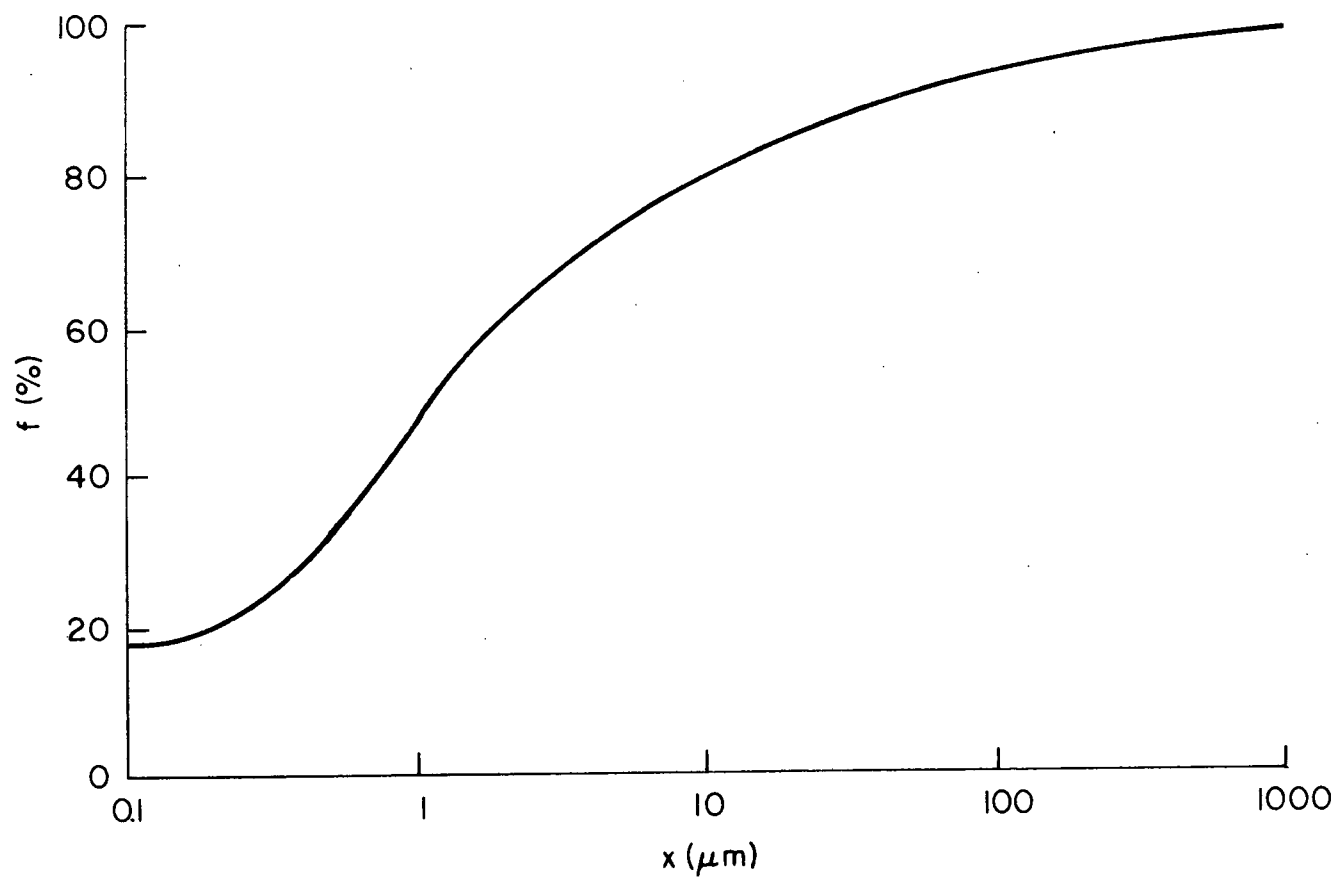
Figure 3. Portion f of the solar photons with energies greater than 1.1 eV which can be absorbed in Si films of variable thickness x.

where K depends upon the type and energy of radiation, and upon the semi-conductor material. Base region sensitivity to radiation is due to the depth of absorption and creation of damage by the bombarding particles, the base-response nature of the Si cell, and the fact that the diffused surface layer has such a poor lifetime (or diffusion length) even before experiencing any radiation flux. Radiation resistance can be increased somewhat by increasing the resistivity of the base region, compromised by increased temperature sensitivity and a reduced initial cell efficiency [an increase in the I_{OA} factor in Equation (1)].

Thus, any improvement in surface region response which may be possible not only increases the absolute efficiency (for fixed junction depth), but also will tend to increase the useful cell life under radiation bombardment. Obviously, the surface region loss mechanisms are related to surface recombination velocity and the effective bulk diffusion length.

REVIEW OF THEORETICAL ANALYSES FOR Si SOLAR CELLS

The solar cell efficiency analysis performed by Wysocki and Rappaport[1] in 1959, established the optimum range of semiconductor energy gap (1.4-1.6 eV). In this computation, series resistance and reflection losses were neglected, and a unity collection efficiency was assumed for all carriers generated by photons with energies greater than the bandgap. State-of-the-art bulk properties were utilized. Of the common semiconductors available GaAs is probably the most ideal choice for a solar photovoltage device. Three sets of calculations were performed to determine the effect of the junction I-V characteristics upon efficiency (diffusion-controlled, recombination-controlled, and a combination of these two). The optimum energy gap remained essentially the same but the efficiency varied considerably with the various types of junction behavior.

Dale and Smith[5] analyzed the spectral response of p/n Si solar cells, including a constant electric field in the surface p-layer. Constant bulk parameters were assumed for the diffused layer. The conclusions were that, in order to match experimental results, very large surface recombination velocities, of the order of 10^5 cm/sec, are required, or alternatively a very low bulk lifetime in the surface material. Experimentally etching cell surfaces to reduce the recombination velocity had very small effect on spectral measurements; therefore, the latter alternative above was assumed. Surface region lifetimes on the order of 10^{-10} sec are necessary to fit the calculated spectral response to experimental device characteristics.

The study by Wolf[6] includes drift fields due to impurity density gradients both in the diffused region and the base region. It further develops a two-layer model for each of the regions, which permits investigations of drift fields in only a portion of each region and effects of spatial variations of the field strength. As in the Dale and Smith analysis, the spectral collection efficiency is computed, individual calculations being performed for the base and diffused regions.

The minority carrier lifetime and surface recombination velocity of the diffused region can only be determined indirectly. In an experimental situation, knowing the parameters of the base region permits a reliable calculation of the partial collection efficiency (essentially short-circuit current/ number of incident photons vs. wavelength). The difference between the measured collection efficiency and that calculated for the base region is the contribution of the diffused surface layer. Wolf compares this surface layer collection efficiency (p/n) with his one- and two-layer models which have recombination velocity and lifetime as parameters. Experimentally obtained spectral response curves for the diffused region can be matched equally well by considering the existence of a drift field or by assuming collection to consist purely of diffusion of minority carriers. However, inclusion or omission of the drift field necessitates a change of the minority carrier lifetime by a factor of about 4.4. Again, constant average values were used for the electrostatic fields and bulk parameters.

After recognition of the fact that cells experiencing irradiation degraded because of a decrease in base region lifetime, interest developed

in the inclusion of an aiding drift field in this region. Kaye and Rolik[7] made linear approximations to the electric field and diffusion constant variations with distance from the junction. Various constant lifetime values were used as a calculation parameter in computing the collection efficiency. The purpose of their study was to optimize the drift field strength and distance. Experimentally fabricated devices incorporating a near-optimum field configuration demonstrated the anticipated minimum short-circuit current degradation due to fluences of 1 MeV electrons. This was at the expense of 18% less short-circuit current than a standard field-free cell at the beginning of bombardment.

Calculations similar to those of Kaye and Rolik were performed by Bullis and Runyan[8]. A smooth curve relating the diffusion coefficient D_n to the logarithm of acceptor concentration N_A was generated in order to obtain the necessary values of D_n and dD_n/dx. Also, a linear function of log τ_n vs. log N_A (τ_n = lifetime of minority carriers) was determined from experimental data. It was discovered that only a slight reduction in collection efficiency resulted in going from an exponential impurity distribution to the erfc case. Short-circuit current degradation under 1 MeV electron bombardment in the base region was calculated for various field configurations. In calculating the total cell short-circuit, it is necessary to include contributions from wavelengths as short as 0.22 μm. If the K factor in Equation (2) is increased as a result of increasing acceptor concentration in the field region, as indicated by experimental data, the result is to reduce the improvement due to the electrostatic field at high fluence levels. In an

experimental study of base region drift fields (n/p) by Runyan and Alexander[9] it is stated that not only does the field not enhance cell performance after bombardment, but because of poor initial values of short-circuit current, the cells with base-region drift fields are generally inferior.

Van Overstraeten and Nuyts[10] use better approximations for the electric field and mobility variations than Kaye and Rolik, and Bullis and Runyan in their calculations of short-circuit current improvement due to a base region electric field. Optimum drift field region widths are determined for various lifetime assumptions. Criticisms and comparisons with the two preceding analyses are offered.

In the three previous analyses the emphasis has been placed on maximizing the collection efficiency or short-circuit current of the base region of the solar cell, or in minimizing the variation of these quantities with degrading radiation. (Van Overstraeten and Nuyts do not consider the latter design problem directly.) Since solar cells are utilized as power sources, a more realistic calculation would be that of power conversion efficiency. A quantitative analysis of the conversion efficiency (η) of GaAs and Si solar cells has been presented by Ellis and Moss[11]. The labors involved in their extensive calculations have been decreased somewhat by avoiding such approximations as used by References 7,8, and 10), assuming instead constant average values for electric fields, diffusion constants and lifetimes. The source intensity distribution is derived from a 140 mW/cm^2 6000 °K blackbody and no energy is lost due to reflection. First, Ellis and Moss develop the currents existing in both the surface and

base regions, and then determine the efficiency by maximizing the V_L-I_L product. Surface recombination is included in the n-layer (n/p cell) contributions to short-circuit and junction diffusion currents. Space-charge region recombination current is calculated by assuming a single trapping level located in the energy gap at the intrinsic Fermi level.

The equation of the short-circuit current generated in the surface layer, J_{SC}^+, derived by Ellis and Moss is essentially the same as developed by Wolf in his single layer model[6].

$$J_{SC}^+ \text{ (surface)} = q \int_{\lambda=0}^{\lambda=\lambda_\infty} \frac{\alpha N(\lambda)}{(\alpha^2+2\alpha\beta-1/L_p^2)} \{- (\beta+\alpha) e^{-\alpha a}$$

$$+ \frac{fe^{\beta a}(s/D_p+2\beta+\alpha) - fe^{-\alpha a}[(s/D_p+\beta) \cosh fa + f \sinh fa]}{f \cosh fa + (\beta+s/D_p) \sinh fa} \} d\lambda, \quad (3)$$

where E_s is the (constant) electric field in the surface region, λ is wavelength, $N(\lambda)$ is the spectral density of photons, α is the absorption coefficient, a is the junction depth, and

$$\beta = qE_s/kT, \quad f^2 = \beta^2 + 1/L_p^2 .$$

A similar equation exists for the base layer contribution to the short-circuit current.

Since Ellis and Moss have a primary interest in GaAs solar cells, they do not treat the Si cell extensively. The result of

12

efficiency calculations for a Si cell with constant impurity densities in both regions is shown in Figure 4. Here the abscissa is measured in terms of the junction depth. Independence of surface recombination velocity, s, even in the absence of an aiding surface field, is demonstrated by the very small variation in efficiency between the curves for s = 0 and s = 10^3 cm/sec. The fact that the efficiency appears to increase to 15% as a → 0 is a result of neglecting the series resistance. Separate calculations by Ellis and Moss for various front surface contact grid spacings indicate an efficiency of 11.5% at a = 0.3 μm for a 4 mm contact separation.

In a cell fabricated by impurity diffusion of the surface layer, the values assumed in obtaining Figure 4 are no doubt unrealistic. In particular, a strong electric field will exist (∿ 5000 V/cm) which is counteracted by a greatly reduced hole diffusion length L_p.

For purposes of comparison, the Ellis and Moss efficiency calculations (neglecting series resistance) for GaAs n/p solar cells are presented in Figure 5. Here the effects of surface recombination and electric fields are more apparent than in the case of Si.

It should be noted that the rather high efficiencies predicted by Ellis and Moss for GaAs cells are the result of assuming a negligible contribution to the junction current due to recombination in the space charge region. Since the forward current-voltage characteristics of GaAs diodes exhibit a considerable degree of space-charge region recombination dependence at the operating solar cell voltage[12], this assumption is perhaps not valid.
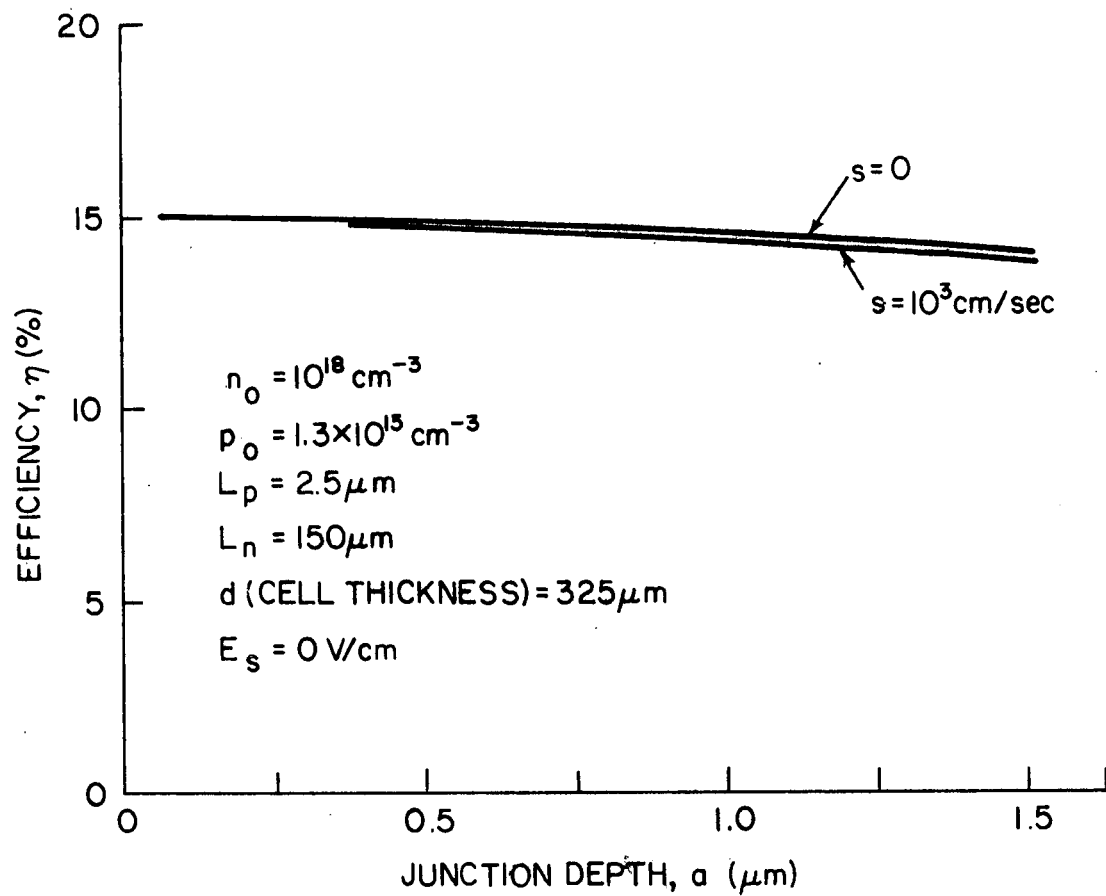
Figure 4. Efficiency of silicon n/p solar cell as a function of junction depth.
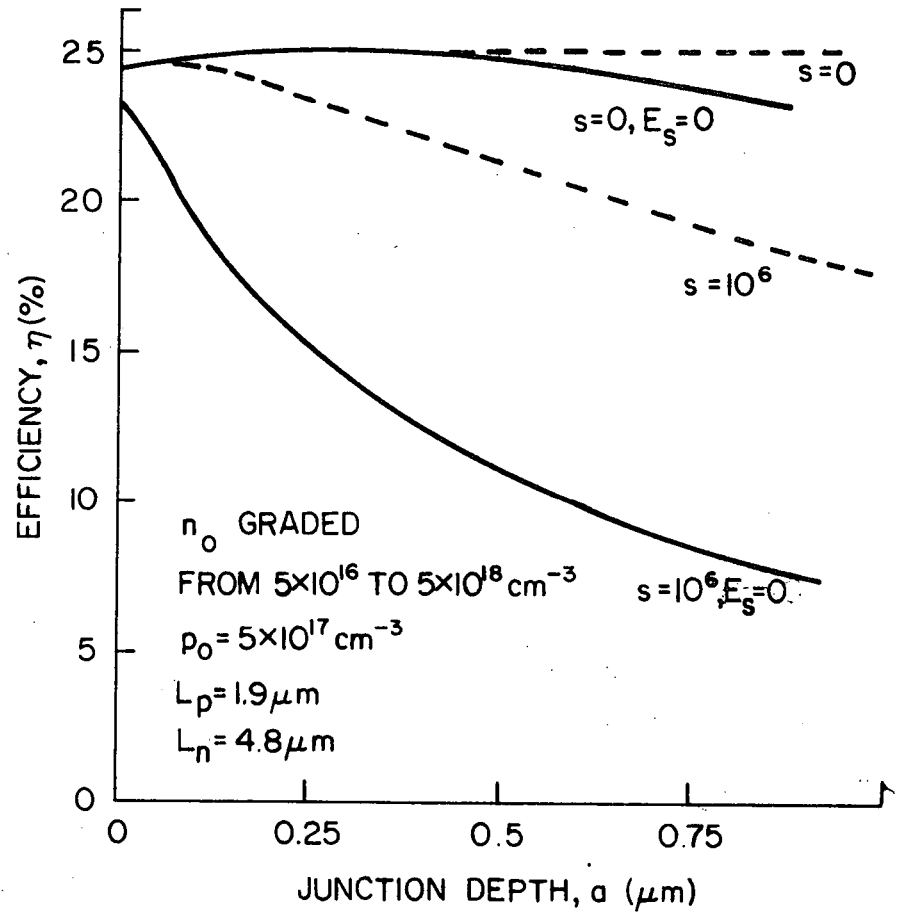
Figure 5. Efficiency of GaAs n/p solar cell as a function of
junction depth.

Sahai and Milnes[12a] have considered efficiency calculations for Si homojunction n/p solar cells in conjunction with their heterojunction solar cell work. They calculate the spectral reflection losses of the antireflection coating for SiO_2 and evaporated SiO. They consider three cell regions: (1) surface layer, (2) depletion region at the junction, and (3) the base region. No attempt was made to incorporate drift fields or impurity density dependent transport parameters. For a 0.5 μm junction depth their "practical" efficiency is 11.69%. This includes series resistance losses (R_S calculated on the basis of a standard 2 x 1 cm contact grid configuration), reflection losses, imperfect collection, and reduction of active area by front surface contact grid. Although the importance of junction recombination currents, J_{rec}, are emphasized, it is not clear just how (or whether) these have been incorporated into the calculation of efficiency. For the ideal case of perfect collection in the Si and no losses of photons or carriers, Sahai and Milnes calculate the cell efficiency to be 20.25%.

Production solar cells presently indicate efficiencies of 10-11% for Si and 7-9% for GaAs.

FACTORS CONTROLLING SURFACE REGION RESPONSE

In terms of reducing the dependence of the Si solar cell efficiency on changes in base region parameters due to the effects of radiation damage, it is desirable to maximize the surface region response. When one examines the collection efficiencies of the surface and base regions of the cell (see Figure 6 for a p/n example), it can be seen that the surface contribution is quite small. This contribution represents the blue response (< 0.5 μm) of a Si solar cell. Of course the maximum ideal surface response is predetermined by the Si absorption coefficient, the solar spectrum and the junction depth. Fabrication of the device determines ultimately the losses due to surface reflection, surface recombination and bulk recombination.

The succeeding sections will consider the absorption coefficient reflectivity, impurity density profile, and surface recombination. These are factors which are associated with the surface and the surface region. A complete discussion of the surface region processes is limited by the lack of information concerning the degenerate layer introduced by the impurity diffusion. The analysis and control of this degenerate layer represents one of the last frontiers in Si solar cell technology.

Absorption Coefficient

Fundamental abosrption of photon energy to create hole-electron pairs occurs for energies greater than the bandgap of a semiconductor. Combining the absorption coefficient of Si with the solar spectrum results in
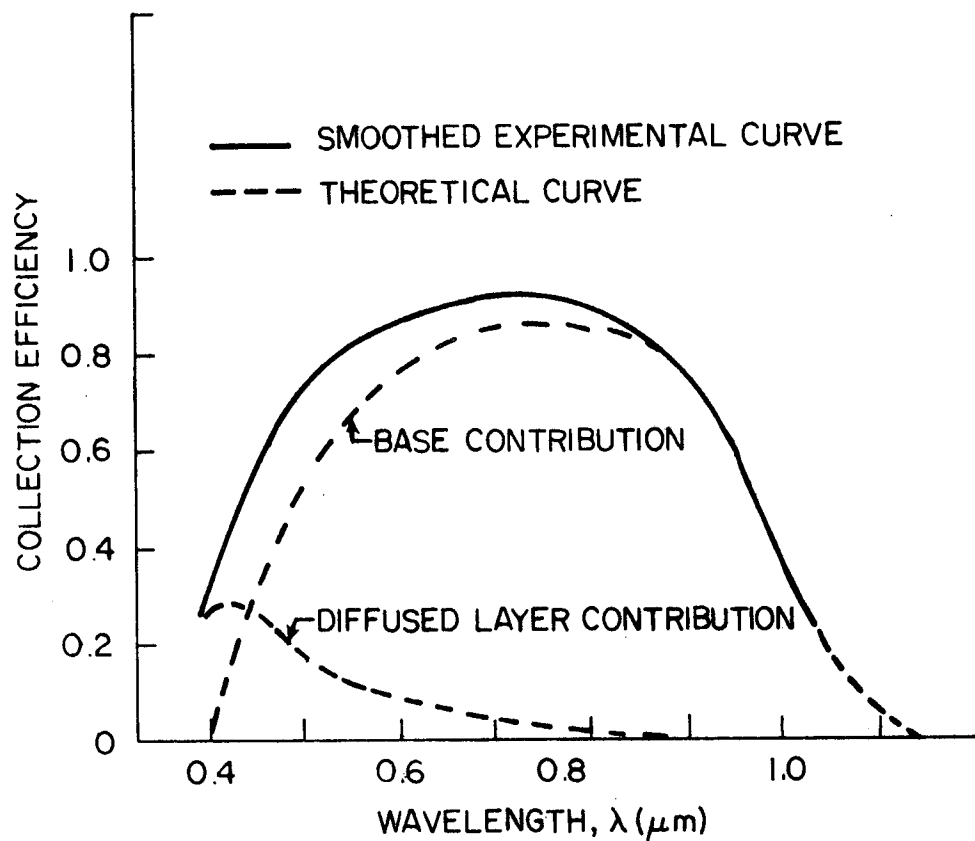
Figure 6. Measured collection efficiency vs. wavelength for p/n Si solar cell, with calculated contribution from the base region, difference curve to be matched by calculated curve for surface layer, $x_J = 0.5$ μm [after M. Wolf, Proc. IEEE, 51, 677 (1963)].

Figure 3 which illustrates the rate of absorption in the depth of silicon. Of 6×10^{17} photons/cm^2-sec in outer space, approximately 2.8×10^{17} have energies sufficient to produce excess carriers. A 0.3 μm surface region collects 21.3% of the active photons in a 350 μm thick cell (neglecting reflection from back surface).

Near the absorption edge ($\simeq$ 1.1 eV for Si) the absorption coefficient appears to increase with increasing impurity concentration. This increase is due to internal scattering and free carrier absorption[13]. Since the diffused layer is very thin compared to the reciprocal absorption coefficient at these wavelengths, this impurity dependence is negligible.

Reflection Coefficient

The reflection coefficient of Si varies between approximately 38% and 30% across the 0.4 - 1.1 μm wavelength range. Since phosphorus-diffused n-on-p solar cells do not exhibit the very low reflection coefficient (< 5%) of boron-diffused p-on-n cells, a quarter-wavelength antireflection coating is necessary. The wavelength of minimum reflection is empirically chosen to optimize the cell efficiency. In a study of thermally oxidized Si[14] the reflection coefficient minimum was 7% for oxide thicknesses matching the 0.5-0.8 μm range. However, the reflection at 0.4 μm still rises to 38-40%. In the case of a heavily doped surface region the smallest reflection coefficient obtainable this way will increase somewhat with carrier density. Improvement of the effectiveness of the antireflection

coating results from the use of evaporated SiO_2 since its refractive index is almost the desired geometric mean of the Si and free space indices.

No doubt a considerable amount of proprietary research has been directed toward the development of a satisfactory evaporated SiO_2 antireflection coating, but little has been reported about such a material interfaced with a semiconductor. (In this discussion, SiO_2 refers to the compound formed at the substrate as a result of evaporating SiO; the actual compositional structure is determined by conditions during deposition.) York[15] studied the transmission of 920 Å-thick SiO_2 films evaporated onto Vycor glass. For wavelengths greater than 0.5 μm the transmission percentage for various deposition rates varied between 85% and 95%. At 0.4 μm the films deposited at rates greater than 50 Å/sec exhibited a 65% transmission. However, no distinction is made between transmission losses due to reflection and those due to absorption.

Of course, unless the increased processing complexity of multiple-layer dielectrics is incorporated, incomplete cancellation of the reflected component must be accepted. However, it does seem that this loss should be considered when attempting to align theoretically efficiency calculations with experimentally derived cell characteristics.

Impurity Profile in Surface Region

Iles and Leibenhaut[16] examined submicrometer solar-cell type diffusions by the technique of sectioning and sheet resistance measurements. They discovered that the impurity profile of the diffused layer did not

follow the theoretical error function complement distribution (erfc) which their diffusion conditions would predict. For a 0.6 μm junction depth, approximately the first 0.2 μm beneath the surface had either a constant impurity concentration with increasing depth (based upon mobility decreasing toward the surface), or a concentration which actually decreased as the surface was approached (if a constant mobility was assumed). This agrees with Tannenbaum[17]. The immediate consequence of the two possibilities is either a) the aiding drift field due to an impurity concentration gradient is nonexistent in a region of the diffused layer adjacent to the surface, or b) there is actually a drift field in this region which enhances the flow of minority carriers to the surface. Beyond this surface layer in the region approaching the junction, the impurity profile appears to be more sharply graded than that expected from the erfc distribution.

The anomalous impurity distribution has been ascribed to the effects of impurity precipitation at the high-concentration surface and field-aided impurity diffusion which is significant in that region where the impurity density exceeds the intrinsic carrier concentration at the diffusion temperature[12,17].

The electric field, E, created by the impurity concentration gradient is proportional to the gradient of the Fermi level. For the one-dimensional solar cell situation at room temperature (assuming all impurities are ionized) with nondegenerate doping, the Fermi level is proportional to the logarithm of the impurity density. Thus the electric field is given by

$$E(x) = \frac{kT}{q} \frac{d \ln N_D(x)}{dx}$$
(4)

where kT/q = 25.9 mV at 300°K, and $N_D(x)$ is the (donor) impurity distribution. If $N_D(x)$ is proportional to $e^{\alpha x}$, then $E(x)$ will be constant with respect to x.

Equation (4) will be valid when the majority carrier concentration is nondegenerate. For silicon at room temperature the transition to degeneracy occurs when $N_D \simeq$ 1-2 x 10^{18} cm^{-3} [13,18]. With increasing donor impurity concentration above this value, the Fermi level increases less rapidly than ln N_D. Thus, an impurity gradient at degenerate concentrations will create a smaller electric field than would a similar gradient at a lower, nondegenerate concentration. As suggested by Iles' results in Figure 7, there is an appreciable portion of the surface region in which a drift field is not present. Wolf[6] considers this situation in his two-layer model for the diffused region in calculating the short-circuit current for a solar cell. The possibility of a positive impurity gradient near the surface has never been analyzed, but presumably this situation could be accommodated by many of the numerical analyses, such as Wolf's.

The problem of computation of theoretical cell performance for analysis or optimization is complicated by the dependence of electrical transport parameters upon the impurity concentration. Functional approximations for the electric field and diffusion constant have been assumed in calculations of short-circuit current[7,8,10]. These calculations usually consider only the base region of the cell incorporating a drift field layer. Minority carrier lifetimes are more difficult to incorporate into an analytical expression since this parameter is also dependent upon the device technology in the region of the diffused surface layer.

22
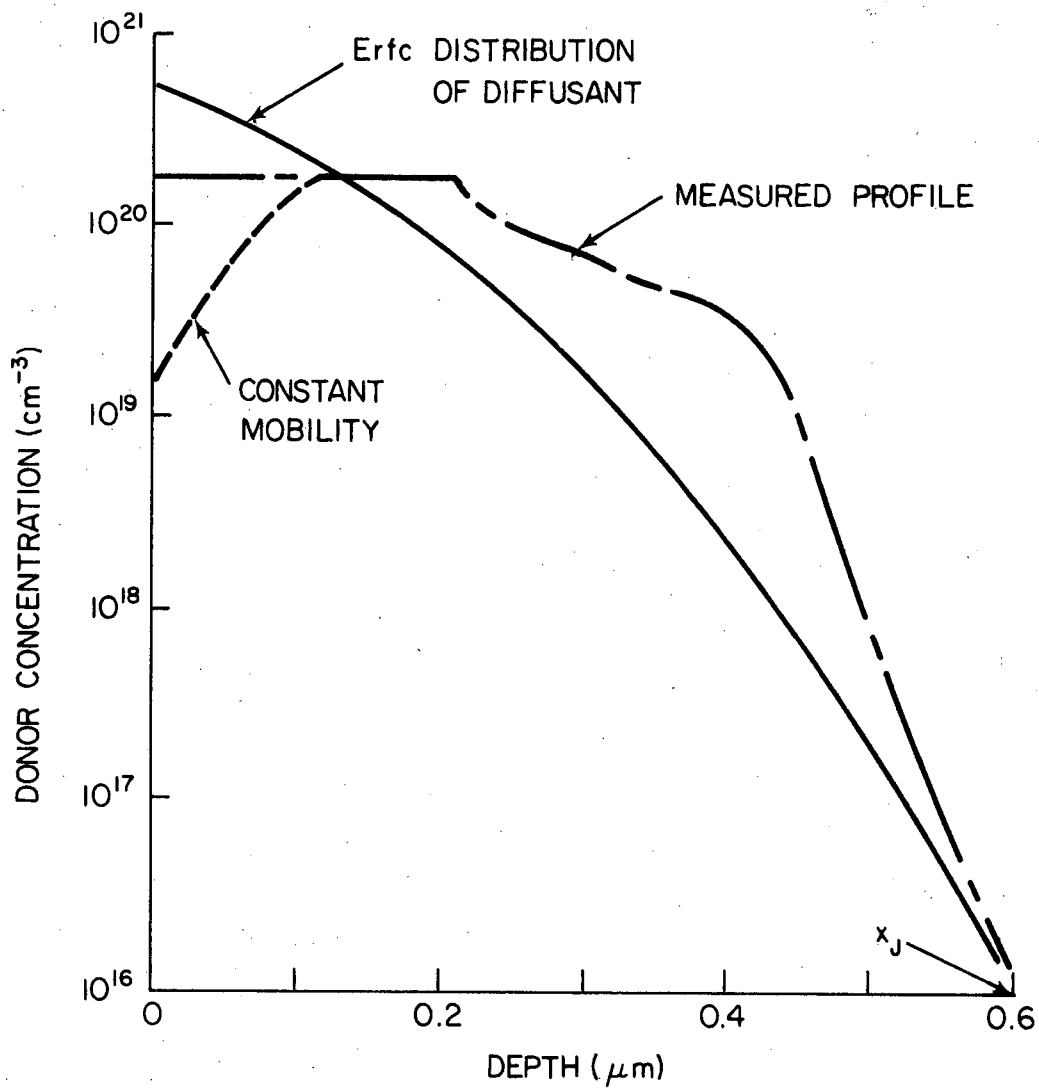
Figure 7. Theoretical and experimental impurity concentration profiles for high temperature diffusion into Si.

Surface Recombination

When the density of free carriers in a semiconductor exceeds the thermal equilibrium value, as in an illuminated solar cell, the excess carriers recombine in the bulk and at the surface. The primary recombination process in both regions has been found to proceed through centers at energy levels within the forbidden gap. Shockley and Read[19] have analyzed statistically indirect bulk recombination by assuming discrete energy levels for the centers. The analogous problem of surface recombination via surface states is similarly treated by Brattain and Bardeen[20]. First, a summary of the derivation of the dependence of the surface recombination velocity upon the properties of the surface states will be presented. Then the methods of altering the recombination rate by varying the surface potential will be discussed. An extensive presentation of semiconductor surface phenomena has been made by Many, Goldstein, and Grover[21] detailing references to both theoretical and experimental work.

Consider a homogeneous semiconductor under uniform steady excitation. The bulk densities of excess holes and electrons are assumed equal. Surface recombination results in equal fluxes of holes or electrons to the surface. The ratio of the rate of electron (or hole) flow into a unit surface area to the excess carrier density in the bulk just beneath the surface is the surface recombination velocity s:

$$s = \frac{U_{n,p}}{\Delta n_b, p_b}$$

where $U_{n,p}$ is the electron or hole flux (number/cm^2 sec), and $\Delta n_b = \Delta p_b$

is the bulk excess carrier density. If the density of excess carriers can be neglected with respect to the total bulk thermal equilibrium density, i.e., $\Delta n_b = \Delta p_b \ll n_b + p_b$, then s is given by [21]

$$s = \frac{[K_n K_p]^{1/2} \, N_t (n_b + p_b)}{2n_i^* \{ (n_i/n_i^*) \cosh [(E_t^f - E_i)/kT - u_o] + \cosh (u_s^* - u_o) \}} \quad (5)$$

where

$K_{n,p}$ = probability per unit time that an electron or hole will be captured by a vacant state,

$u_o = 1/2 \ln (K_p/K_n)$,

N_t = surface density of recombination centers, all at an energy E_t,

n_b, p_p = bulk thermal equilibrium electron and hole densities,

n_i = intrinsic carrier density,

E_i = intrinsic Fermi energy,

$n_i^* = n_i \exp [(F_n - F_p)/2kT]$,

$F_{n,p}$ = quasi-Fermi levels for electrons and holes,

$E_F^* = 1/2 (F_n + F_p)$, the steady-state mean Fermi level,

$u^* = (E_F^* - E_i)/kT$, the steady-state potential,

$E_t^f = E_t + kT \ln (g_o/g_1)$

g_o, g_1 = the number of degenerate quantum states of the center when it is vacant and occupied, respectively.

The subscript b refers to the bulk semiconductor beneath any surface space charge region, and the subscript s refers to the surface. If more than one

energy level E_t is involved, then (5) must be summed for the various levels.

The surface recombination velocity not only depends upon the properties of the surface states, but also upon the bulk properties n_i and $n_b + p_b$, and on the level of excitation. The dependence upon bulk doping was experimentally observed in etched Ge by Schultz[22] and in thermally oxidized Si by Rosier[23].

Surface preparation and subsequent atmospheric exposures determine strongly the distribution and density of surface states within the semiconductor forbidden gap as well as the capture cross section of the states.

Traditionally, the surface centers have been divided into two groups, fast states and slow states, depending upon their relaxation times. The fast states can follow disturbances up to tens of megahertz, while the slow states may require hours or days to achieve equilibrium with the semiconductor excess carrier density. Since clean surfaces do not exhibit slow states, these states are normally considered to exist at some depth in the thin oxide layer on the surface of semiconductors exposed to the normal atmosphere. Fast states are associated with the abrupt discontinuity in the crystal lattice at the semiconductor surface. The early studies of surface states utilizing etched surfaces exposed to various gaseous ambients were hampered by very high densities of slow states which prohibited the alteration of the surface potential of the semiconductor with respect to the bulk under d-c or low frequency excitation conditions. Thermally oxidized Si is unique in that the slow state density is very low, thus making field effect devices possible. The basic model for surface recombination has evolved from consideration of quantitative studies of the fast surface states.

26

In thermal equilibrium the presence of acceptor- or donor-like surface states will affect the energy bands in the vicinity of the surface. An acceptor state introduced below the Fermi level will acquire electrons from the conduction band. Thus, the surface becomes negatively charged and a positive space charge region forms beneath it bending the bands upward until overall charge neutrality prevails. This process is illustrated for a surface state at E_t in Figure 8. Analogously, donor-like states introduced above the Fermi level cause a downward bending of the energy bands at the surface. The extent of the space charge region is characterized by the extrinsic Debye length L,

$$L = [\frac{\epsilon kT}{q^2 (n_b + p_b)}]^{1/2} ,$$

(6)

where ϵ is the dielectric constant of the semiconductor.

An energy-level diagram indicating the various parameters used to characterize the surface space charge region for an n-type semiconductor is shown in Figure 9. Assuming a homogeneously doped semiconductor, the bending down of the energy bands at the surface indicates an accumulation of electrons forming a negative space charge region. The potential is defined by $q\phi = E_F - E_i$. The potential barrier with respect to the bulk is $V = \phi - \phi_b$, and at the surface the barrier height is $V_s = \phi_s - \phi_b$. For convenience two dimensionless potentials are defined:

$$u = q\phi/kT; \quad v = qV/kT.$$

When $v < -2u_b$, an inversion layer exists. If the disturbance to thermal equilibrium is small compared to even the minority carrier density, then the starred energies and potentials defined in Equation (5) will approach the thermal equilibrium values defined above. However, in the case of optical generation due to the solar flux this approximation is not justified.

27
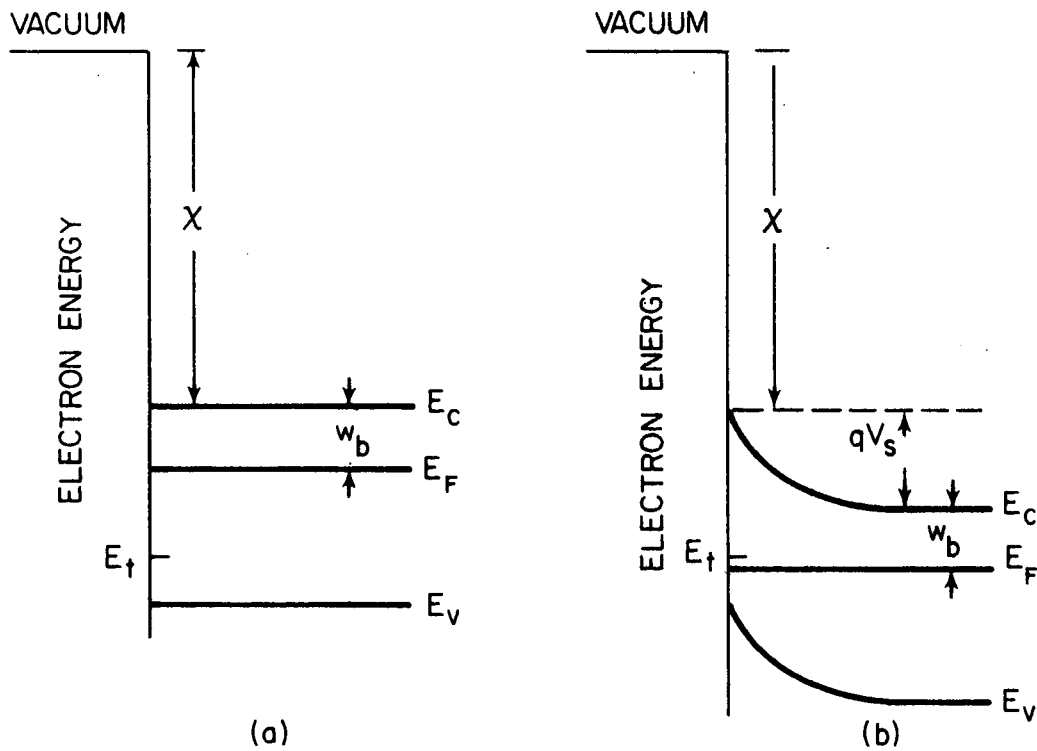
Figure 8. N-type semiconductor in presence of acceptor-like surface
state at energy level E_t. (a) immediately following intro-
duction of surface (b) after thermal equilibrium.

$$V_s = \phi_s - \phi_b > 0$$
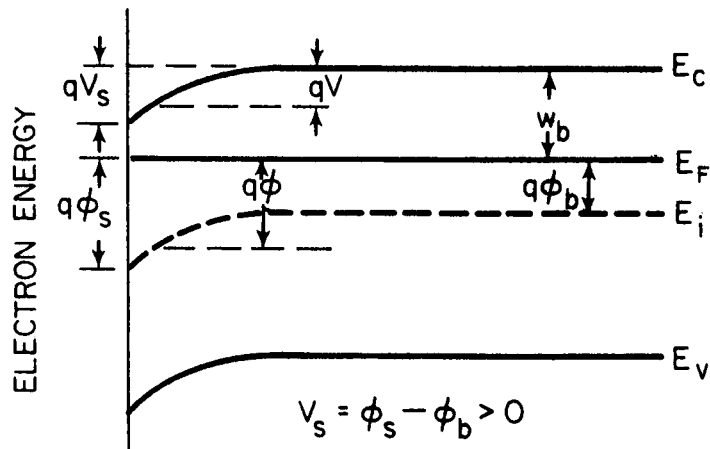
Figure 9. Energy-level diagram indicating the various energy
parameters. N-type accumulation layer.

The equilibrium value of u_s is determined by the requirement for charge neutrality between the surface states and the space charge region of the semiconductor: $Q_{ss}^0 + Q_{sc}^0 = 0$; Q_{ss} is the surface state charge density (per unit area) and Q_{sc} is the space charge density. The superscript zero refers to the absence of any external field normal to the surface. Under thermal equilibrium conditions,

$$Q_{ss}^0 = q \, N_t \, f(E_t^f), \tag{7}$$

and

$$Q_{sc}^0 = q(n_b + p_b) \, LF_s . \tag{8}$$

The Fermi distribution function is

$$f(E_t^f) = \frac{1}{1 + \exp \{\pm [(E_t^f - E_i)/kT - u_s]\}} , \tag{9}$$

where the positive sign refers to acceptor-like states and the negative sign to donor-like states. The function F_s is derived from Poisson's Equation assuming nondegenerate statistics:

$$F_s(u_b, v_s) = \sqrt{2} \left[\frac{\cosh (u_b + v_s)}{\cosh u_b} - v_s \tanh u_b - 1 \right]^{1/2} . \tag{10}$$

Acceptor-like states contribute negative surface charge.

By Equations (7) and (8), the equilibrium surface potential is determined, in principle.

Now consider the situation in which an electric field is applied normal to the surface, perhaps by placing a plane electrode close to the semiconductor. An external potential between the field electrode and the

29

bulk of the semiconductor will induce an electrode charge Q_M which must be equal to the $Q_{ss} + Q_{sc}$:

$$Q_M/q = \mp (n_b + p_b) \, LF_s \mp N_t \, f(E_t^f) \tag{11}$$

The sign of the first term is that of Q_{sc} (negative for $v_s > 0$). Acceptor-like states employ the minus sign before the second term. Obviously, Eq. (11) is difficult to solve for u_s. The rate of change of v_s with respect to the induced charge Q_M is obtained by differentiating Equation (11)

$$\frac{dv_s}{d(Q_M/q)} = \frac{-1}{(n_b + p_b)L|dF_s/dv_s| + N_t|df(E_t^f)/dv_s|} \tag{12}$$

Equation (12) demonstrates the "anchoring" effect of a large surface state density N_t. The derivative $|df(E_t^f)/dv_s|$ is greatest when the Fermi level E_F passes through E_t^f. Similarly, accumulation and inversion layers exhibit anchoring since $|df_s/dv_s|$ varies exponentially with v_s in these regimes.

An n-type semiconductor with a surface-state induced accumulation layer is considered in Figure 10 to demonstrate the effect of an external electric field upon the surface potential. A set of uncharged acceptor states are assumed to exist above the Fermi level in Figure 10a. With the application of a field directed from the electrode to the surface, majority carrier accumulation rapidly increases the space charge at the surface as shown in Figure 10b. The acceptor levels are now below the Fermi level and begin to trap electrons from the conduction band. After equilibrium is achieved, the energy level diagram is that of Figure 10c.
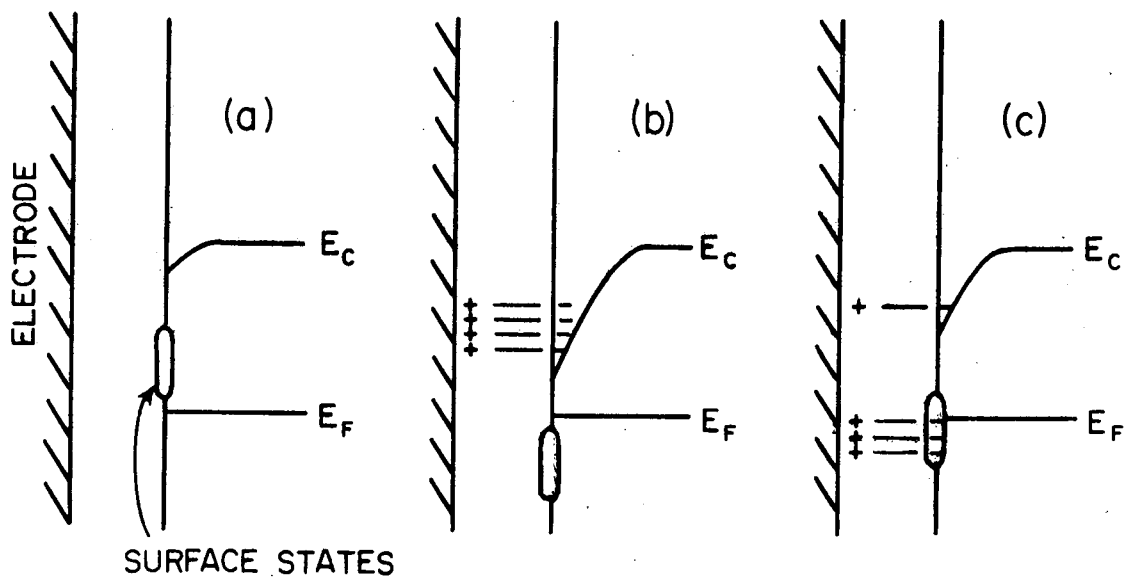
Figure 10. Shape of conduction band edge in n-type semiconductor under step function electric field applied normal to surface.
(a) Prior to application of field.
(b) Just following onset of the field.
(c) Under steady-state conditions.
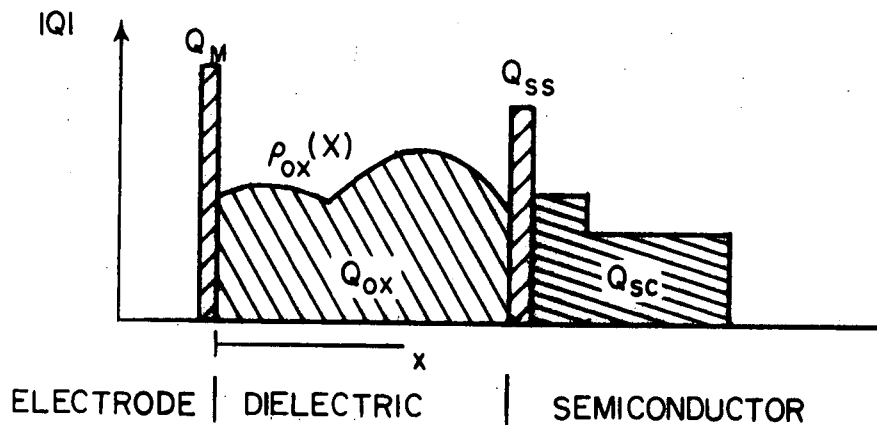
Figure 11. Distribution of charge in a metal-dielectric-semiconductor system.

31

An extension of the electrode-dielectric semiconductor situation would include the presence of stationary charge in the bulk of the dielectric. The distribution of bulk and surface charges is illustrated by Figure 11, in which Q_{ox} represents a general charge distribution within the dielectric, $\rho_{ox}(x)$. Again charge neutrality requires that $Q_M + Q_{ox} + Q_{ss} + Q_{sc} = 0$.

Perhaps at this point it would be beneficial to review the nature of the insulator-semiconductor interface by considering the extensive work on thermally oxidized silicon surfaces. Besides the possibility of fixed or mobile ions in the bulk of the oxide (Q_{ox} in Figure 11), the interface region is associated with various types of charges and states. The fast surface states have already been discussed with respect to their relation to surface recombination. Usually they are symbolized by their surface density N_{st}, and the amount of charge contained for a particular surface potential has been previously denoted in this work by Q_{ss}.

A second characteristic of the SiO_2-Si system is the existence of a fixed charge located within 200 Å of the interface. This fixed charge density, Q_{fc}, is a strong function of the oxidation and annealing conditions, and the orientation of the silicon crystal. Goetzberger, et.al.[24] hypothesize, as the result of experimental observations, that this fixed charge, which appears to be due to excess ionic Si in the oxide, actually induces the surface states, N_{st}. The coulombic field of the oxide charges is assumed to give rise to localized donor or acceptor states. This hypothesis requires the accumulation of more experimental evidence to put it on firm grounds.

Another source of charge near the interface is the drifting of mobile ions to this region as the result of a suitable bias electric field (usually at temperatures somewhat above room temperature). Drifting alkali ions have been a considerable problem in the development of stable oxide-passivated device structures.

Under bias conditions a positive space charge of trapped holes near the oxide-silicon interface results from exposure to ionizing radiation.

Thus, for a more general situation, the charge density Q_{ss} shown in Figure 11 would be the sum of surface state charge, fixed charge, impurity ions and ionized traps.

Swystun and Tickle[25] observed an instability in field-effect transistors fabricated with vacuum deposited SiO_2 as the gate insulator. This instability was observed as a voltage shift in the transistor transfer characteristics after bias-temperature stressing. The results are accounted for by a model in which mobile ions are located predominantly in traps at the SiO_2 interfaces (metal and semiconductor).

So, having related the surface recombination velocity to the surface potential in Equation (5), and the surface potential to an external electric field at the surface, it is now possible to consider the control of s by an external field. As mentioned previously, the equilibrium surface potential of a surface with a high density of slow states is effectively anchored against the influence of an external field. Thus, the early measurements of etched Ge and Si utilized pulsed or high frequency techniques

33

to obtain large deviations of u_s from its equilibrium value. Simultaneous measurement of the lifetime and change in conductance of a filamentary sample subjected to a transverse electric field is one method used to determine the s vs. u_s characteristics[26,27]. The reverse saturation current of a thin planar diode has also been used in conjunction with a sinusoidal field to measure the surface recombination velocity in Ge and Si[28,29,30]. Rosier[23] used a forward-biased planar diode to study the inversion region recombination velocity and surface state characteristics of Si-thermal SiO_2 interfaces. Goetzberger and Sze[31] present a review of the methods incorporating MOS devices to study surface characteristics by means of capacitance-voltage measurements. With this method no information is obtained concerning the surface recombination velocity.

In Figure 12[21] the relative value of surface recombination velocity as a function of $u_s - u_o$ [see Equation (5)] is shown for a discrete surface state level at E_t. Figure 13 shows the experimental results for the distribution of surface-state density at a Si-SiO_2 interface obtained by Goetzberger, et.al.[24]. Frankl[32] disagrees with the simple interpretation of data used to obtain the state densities indicated near the band edges. Obviously, the behavior of s/s_{max} shown in Figure 12 becomes more complex when density distributions like those of Figure 13 are analyzed.

It should be recalled that the $F_s(u_b, v_s)$ function defined in Equation (10) is valid only for nondegenerate conditions, both in the bulk and at the surface. An extension for degenerate surface conditions is made in Chapter 4 of Reference 21.
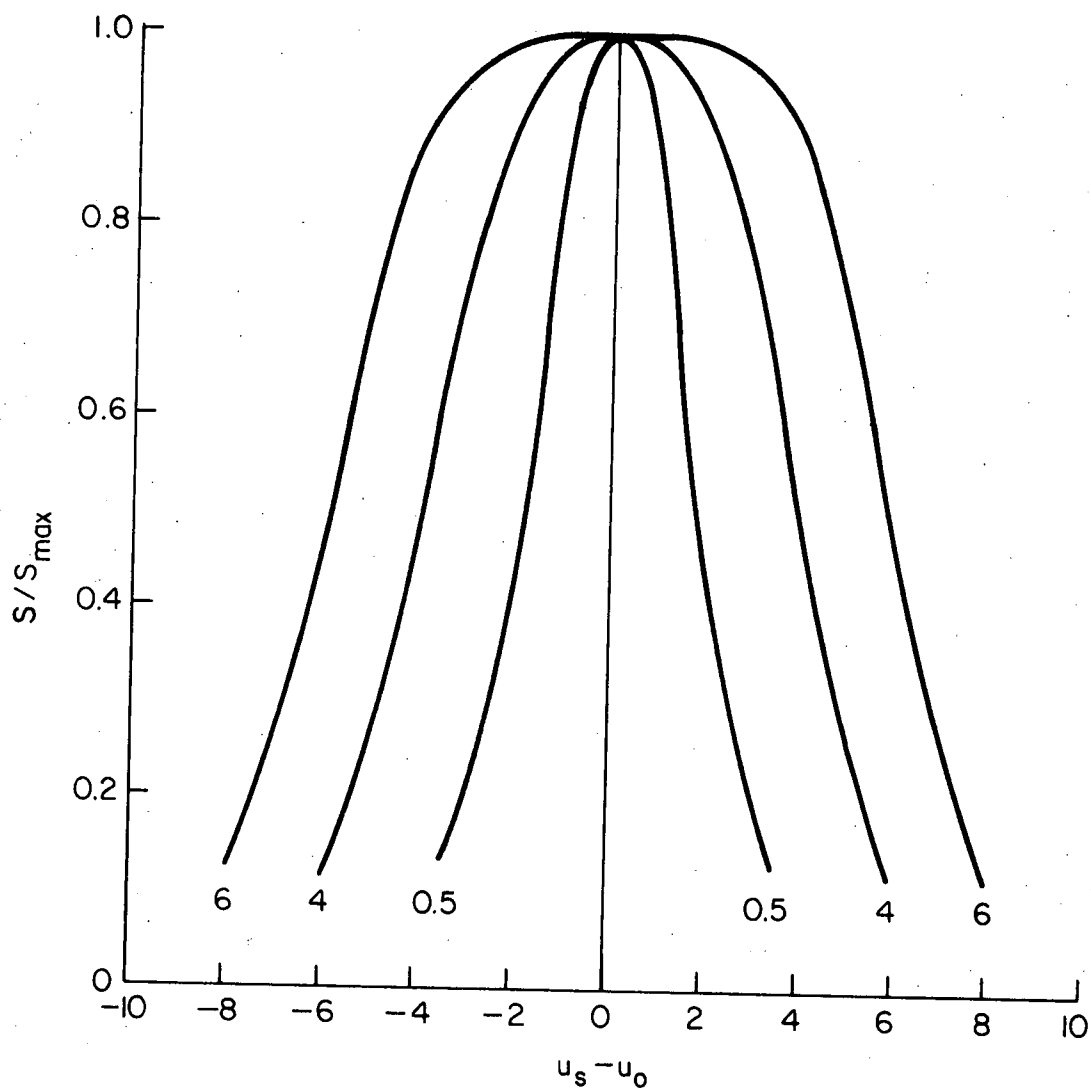
Figure 12. Relative values of surface recombination velocity as a function of u_s-u_o for single-charge centers at an energy E_t. The different curves are for various values of $|(E_t^f - E_i)/kT - u_o|$.
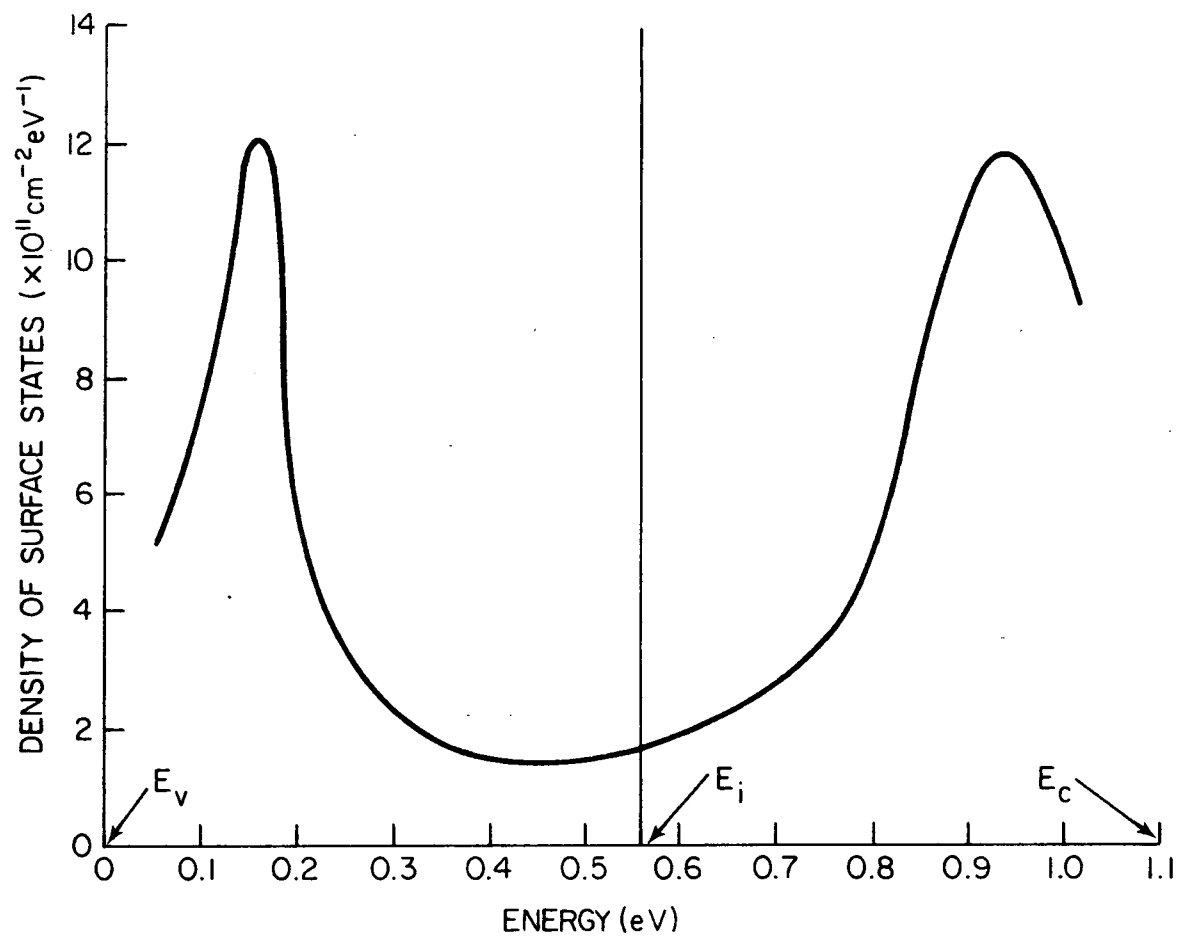
Figure 13. Surface-state density of a SiO₂-Si interface.

Surface Recombination in a Solar Cell

The extensive, although somewhat idealized, solar cell efficiency calculations by Ellis and Moss[11] will be considered here. They have assumed constant values for mobility, diffusion length and electric field throughout the surface region. Nondegenerate impurity concentrations have been chosen for the diffused surface layer of the cell. With these conditions their short circuit current density contribution due to the surface layer absorption of photons is given by Equation (3).

When the cell is operating at forward bias, the junction currents must be subtracted from the short-circuit current. One contribution to the forward-biased junction current is the diffusion current J_d expressed as

$$J_d = J_o \ [\exp \ (qV/kT) \ -1] \ ,$$

where $J_o = J_o^+ + J_o^-$, the diffusion current components from the surface and base regions, respectively. (It should be noted that V is the bias on the junction which may be greater than the external load voltage due to the effects of series resistance.) J_o^+ is also dependent upon the surface recombination velocity:

$$J_{diff.} = j_o^+ + j_o^- \ ; \tag{13}$$

$$j_o^+ = p_o D_p \ \{ \ \frac{f[f \ \sinh \ fa + (s/D_p + \beta) \ \cosh \ fa]}{(s/D_p + \beta) \ \sinh \ fa + f \ \cosh \ fa} - \beta \ \} \ q \tag{14}$$

The second contribution to the junction current is the recombination of carriers in the junction region, J_{rec}. This current, which does not

depend upon s, is considered to be responsible for the observed $e^{qV/AkT}$ (1 < A < 3) behavior of the forward current of the solar cell operating as a diode.

From Equation (3)[11] it is seen that surface recombination enters in the factor $(\beta + s/D_p)$, or $(qE_s/2kT + s/D_p)$. With a junction depth of 0.3 μm, and an exponential impurity concentration graded from 10^{19} cm^{-3} at the surface to 10^{16} cm^{-3} at the junction (neglecting degeneracy; p-type base region doped to 1 ohm-cm) the electric field E_s is 5770 V/cm. Thus, β becomes 1.16×10^5 cm^{-1}. Assuming the values s = 10^3 cm/sec, D_p = 1 cm^2/sec, the ratio s/D_p = 10^3 cm^{-1}. Thus, the term involving s is negligible under the conditions assumed above. Unfortunately, Ellis and Moss do not perform efficiency calculations for the case of an electric field in the surface region for Si cells. Their results for a constant donor concentration (n-on-p cell) are shown in Figure 4. The difference between s = 0 and s = 10^3 cm/sec does not become significant until the junction depth exceeds 1 μm.

The insensitivity of cell efficiency upon surface recombination in the absence of an electric field in the diffused region illustrated in Figure 4 is attributed to the dominant base region response of a Si solar cell (because the electron diffusion length is so great).

For the material parameters and electric field suggested by Figure 5 for GaAs, $s/D_p \approx 10^5$ cm^{-1} vs. $\beta = 3 \times 10^4$ cm^{-1}. In this situation the surface recombination is predominant over the effect of the electric field.

Experimentally, the cell parameter which should be observed to determine the effect of altering the surface recombination velocity is the short circuit current. Since the surface region response is being studied, spectral measurements should be made at the shorter wavelengths to determine the variations in collection efficiency.

The proposed approach to modifying the surface recombination velocity is shifting the surface potential by means of an external electric field. This field is to be introduced by ion implanting a fixed positive charge in the oxide antireflection coating. Under this condition the n-type silicon surface interfaced with the oxide will tend to accumulate, the total oxide charge being equated to the sum of the surface state charge and the semiconductor space charge.

Another method of experimentally obtaining the desired external field is to place a transparent conducting electrode upon the surface of the oxide layer. In the absence of any charge trapped in surface states the space charge induced in the semiconductor surface (charge per unit area) will be $Q_{sc} = \varepsilon_{ox} E_{ox}$, where ε_{ox} and E_{ox} refer to the oxide permittivity and electric field, respectively. If the relative dielectric constant of the oxide is 3.9 and the breakdown field strength $\simeq 2 \times 10^6$ V/cm, the maximum induced space charge is $Q_{sc(max)} = 6.9 \times 10^{-7}$ C/cm^2. The shift in surface potential can be obtained by referring to Equation (8). If the bulk electron concentration is assumed to be 10^{18} cm^{-3} (approximately the limit of nondegeneracy; L = 40 Å), then $F_s = 10.75$. Entering Figure 4.7 of Reference 21 (see Figure 14) with this value of F_s (with $\omega_b = 4$) yields $v_s \simeq 4.3$.
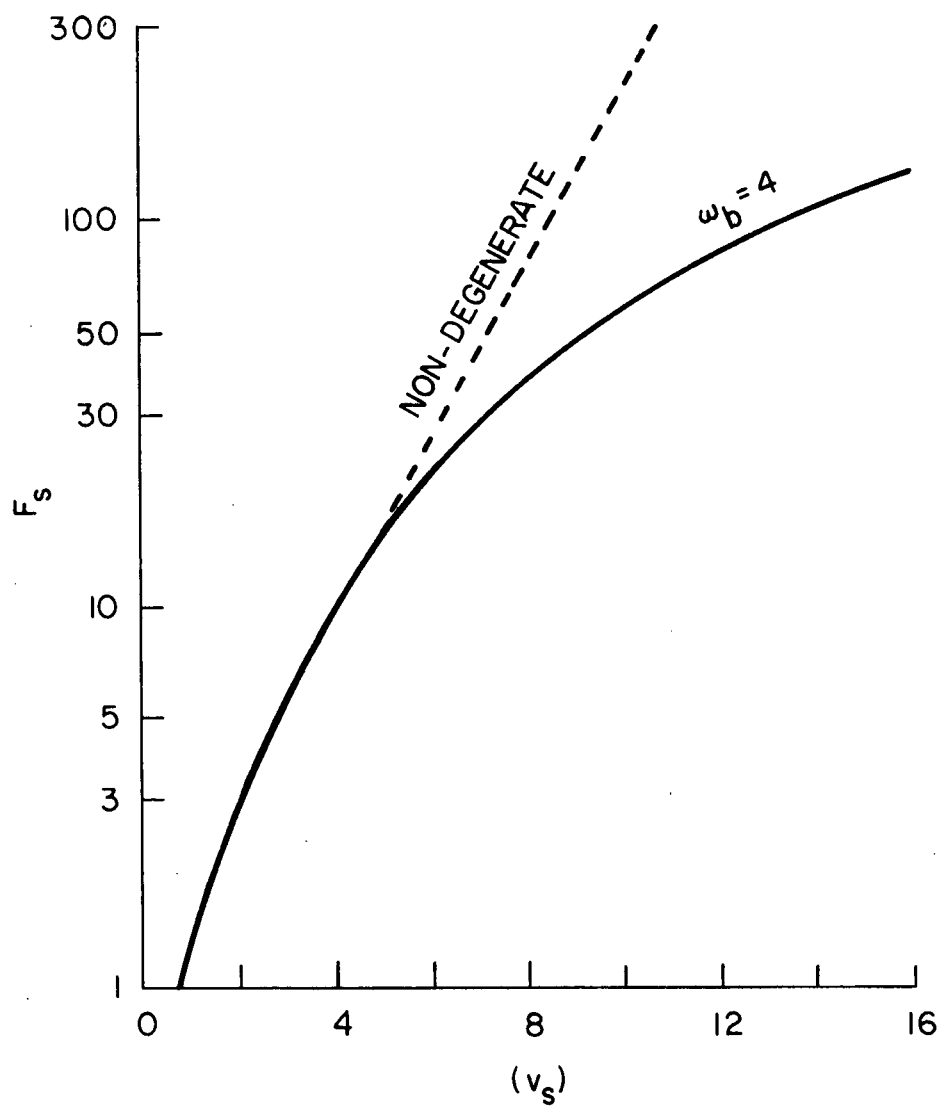
Figure 14. Function F_S vs. barrier height $|v_s|$ in accumulation layers. For $w_b = 4$ surface space charge layer is degenerate.

This graph of F_s vs. v_s takes into account degeneracy in the space charge region. As indicated following Equation (11), the case of additional charge present in surface states is, in general, untenable. For degenerate values of n_b, Seiwatz and Green[34] have integrated Poisson's equation to obtain an expression for F_s. This expression requires tabulated Fermi integrals.

Variations of surface recombination velocity due to an external field have been observed experimentally. However, the results are often difficult to explain with the simple models presented above. Henisch, et.al.[27] measured s for etched n- and p-type germanium surfaces. The field plate was insulated from the surface with mica. In both types of material s was observed to increase for positive plate voltages. From this they concluded that the recombination process is dependent on the electron concentration at the surface. A similar arrangement was used by Snitko[23] to observe surface recombination in etched n-type silicon. The surface recombination velocity was determine by the relaxation of photoconductivity after a light pulse. As can be seen in Figure 15, the values decrease with increasing positive voltage on the field plate (opposite to the germanium experiments mentioned above).

In the preceding analyses the semiconductor was assumed to be in thermal equilibrium. Any disturbance that results in carrier excitation generally modifies the surface space charge. However, as long as the excess majority carrier density is much less than the equilibrium value n_b, (low-level injection) this modification can be considered negligible. This is the situation in a solar cell under normal illumination.
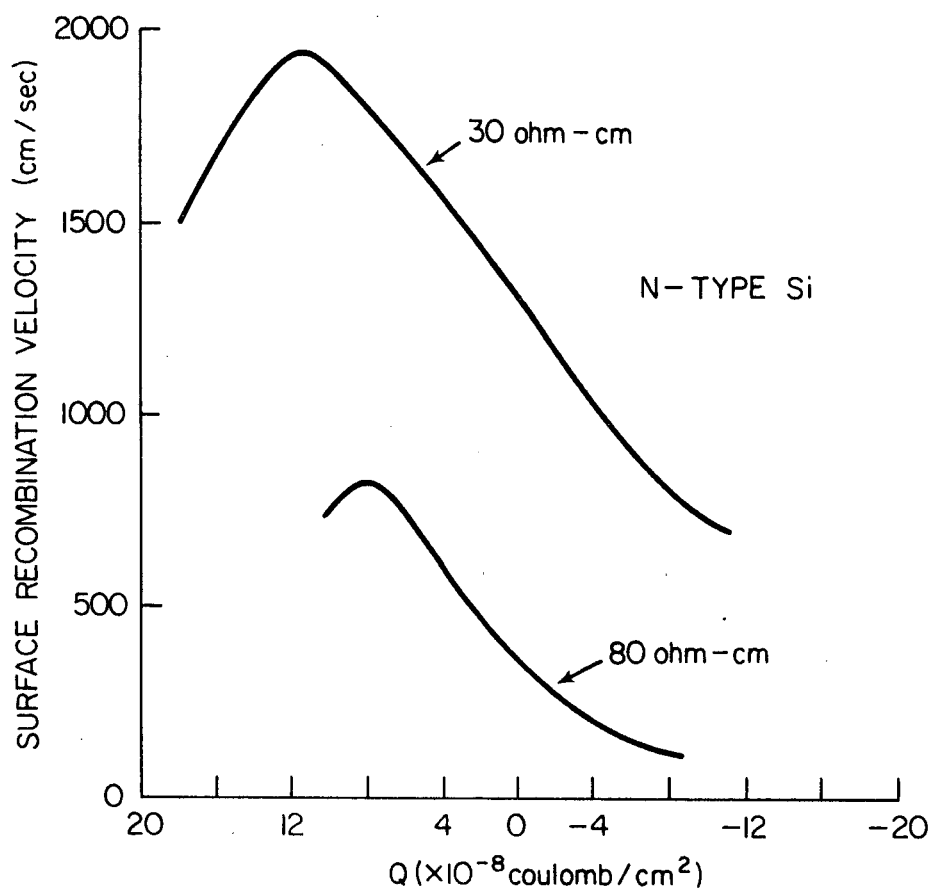
Figure 15. Dependence of surface recombination velocity on the amount of charge induced on Si surface by an external electric field.

ION IMPLANTATION

Ion implantation is the introduction of atoms into the surface region of a solid substrate by bombarding the solid with high energy (keV-MeV) ions. The theoretical and experimental aspects of this process are covered extensively in the book by Mayer, et.al.[35]. Typically, ions of the bombarding species are accelerated in a vacuum and mass-separated by a magnet before impinging upon the substrate surface. Factors affecting the final implanted distribution are the mass and energy of the incident ions, and the atomic mass of the substrate material. As the incident ion strikes the substrate and slows down, it experiences many collisions with the host lattice, displacing the lattice atoms in the process. The result is a region of vacancies, interstitial atoms, and other types of lattice disorder around the track of each ion. If the density of these tracks is sufficient to cause overlap, an amorphous surface layer is created.

Generally, it is possible to anneal the lattice damage at elevated temperatures which do not cause significant diffusion of the impurity ions. This annealing is especially important when implantd ions are to behave as electrically active dopant atoms in a semiconductor device. If the implanted density is sufficiently low to prevent an amorphous region, the disorder can be annealed continuously by heating the substrate ($\sim$ 300°C for Si) during implant.

Ion implantation has been used as a general technique of semi-conductor device fabrication and has been applied in the areas of solar cells, radiation detectors and MOS field effect transistors. Burrill, et.al.[36]

43

E

describe the production of n/p Si solar cells with AMO efficiencies greater than 9.3 percent by implanting variable energy phosphorous ions into Al-doped substrates. Reduction of the gate-drain capacitance in a MOS field effect transistor has been achieved by using the aluminum gate electrode as a mask during the ion implantation of the source and drain regions[37]. In this situation, the dopant ions are implanted into the silicon substrate through the oxide layer.

One feature of ion-implanted silicon surfaces is the appearance of a hazy or milky color[35]. Two proposed mechanisms for this visual change are Rayleigh scattering by small disordered regions[38] and a change in reflectivity due to a change in the average dielectric constant[39]. Peaks in the optical reflectivity in the 3-6 eV range are considerably reduced by implanting 10^{13} ions/cm^2. However the latter reference does not extend the spectral measurements of reflectivity into the visible region. Of course, these two mechanisms are correlated to Si surfaces, but presumably similar effects due to lattice disorder would be present in other materials. Annealing at elevated temperatures returns the optical reflectivity to essentially its pre-implant value, unless the implant density is sufficient to cause surface pitting.

Theory predicts that the concentration profile of implanted ions is a Gaussian distribution characterized by a projected range R_p, and a standard deviation ΔR_p. Thus, the density $N(x)$ (number of ions/cm^3) at a distance x from the surface is

$$N(x) = N_{max} \exp \left[- (x-R_p)^2/2\Delta R_p^2\right],$$

(15)

where N_{max} is the maximum density at the peak of the distribution. N_{max} can be obtained approximately from

$$N_{max} \simeq N_i / \sqrt{2\pi} \; \Delta R_p \; ,$$

where N_i is the total number of ions implanted per unit area. These equations are first-order approximations for the region within a few ΔR_p of the peak at R_p, particularly in an amorphous substrate. When the incident ion beam is directed along one of the major axes of a crystalline substrate, nuclear energy losses decrease and the ion penetrates relatively more deeply than R_p before coming to rest. This process is known as channeling. A secondary peak occurs in the distribution profile. This channeling is difficult to analyze theoretically and control experimentally.

The range of a given projectile, expressed in units of mass/cm^2, varies only slowly with the atomic number of the target. Thus, for the case of SiO$_2$ on silicon, the SiO$_2$ layer can be converted to an equivalent thickness of silicon for distribution calculations. Since the mass densities are so similar (2.33 gm/cm^3 for Si vs. 2.27 gm/cm^3 for SiO$_2$), it is assumed in this research that the two materials behave identically with respect to the bombarding phosphorus ions.

A plot of the computer calculations of Johnson and Gibbons (Reference 35) for phosphorus ions implanted into Si are shown in Figure 16. To aid in visualizing the distribution, the full-width at half-maximum, R_{hm}, is given rather than ΔR_p, where $R_{hm} = 2.36 \; \Delta R_p$. The information in Figure 16 was used to determine the phosphorus ion distribution in the
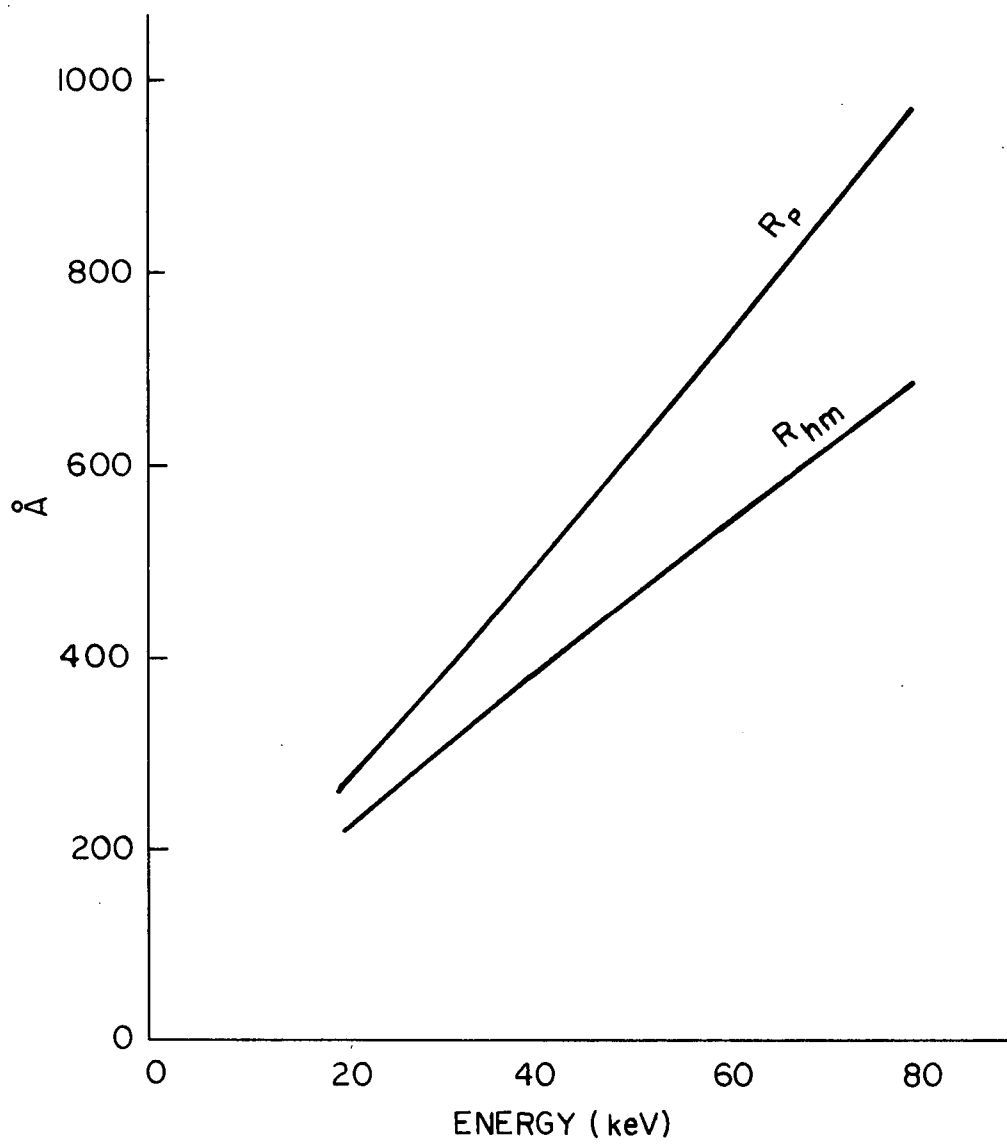
Figure 16. Projected range, R_p, and full width at half-maximum $(2.36 \times \Delta R_p)$, for phosphorus ions in Si as a function of ion energy.

solar cell structures in the current research. Figure 17 represents a normalized Gaussian distirbution with the abscissa in units of R_{hm}.

The amount of charge implanted into the insulating oxide layer is determined by the integral for Q_{ox}:

$$Q_{ox} = q \int_{x=0}^{d} N(x) \, dx, \qquad (16)$$

where $N(x)$ is given in Equation (15), q is the electronic charge, and d is the thickness of the oxide layer. By letting the upper limit in the integral go to infinity the total implanted charge is determined.

Referring again to Figure 16, placing the peak of the ion distribution at the center of a typical 700 Å thick oxide layer would require a 28 KeV energy, resulting in a R_{hm} of 280 Å ($\Delta R_p = 119$ Å). From Figure 17, the density of ions at the SiO_2-Si interface will be $10^{-2} \, N_{max}$. For this example more than 99% of the implanted charge is within the oxide layer [see Equation (16)]. By Gauss' law the maximum electric field in the oxide, which appears at the SiO_2-Si interface, will be

$$E_{ox}(max) = Q_{ox}/\varepsilon_{ox} \simeq qN_i/\varepsilon_{ox}, \qquad (17)$$

where ε_{ox} is the oxide permittivity. For $N_i = 10^{13}$ cm^{-2}, $E_{ox}(max)$ becomes 4.6×10^6 V/cm.

During ion implantation, ejection of substrate atoms (sputtering) occurs. Southern, et.al.[40] measured the sputtering yield of metals and single crystal Si and Ge targets bombarded with 1-5 KeV argon ions. The sputtering yield of Si (atoms/ion) approached 1.3 for the highest

47
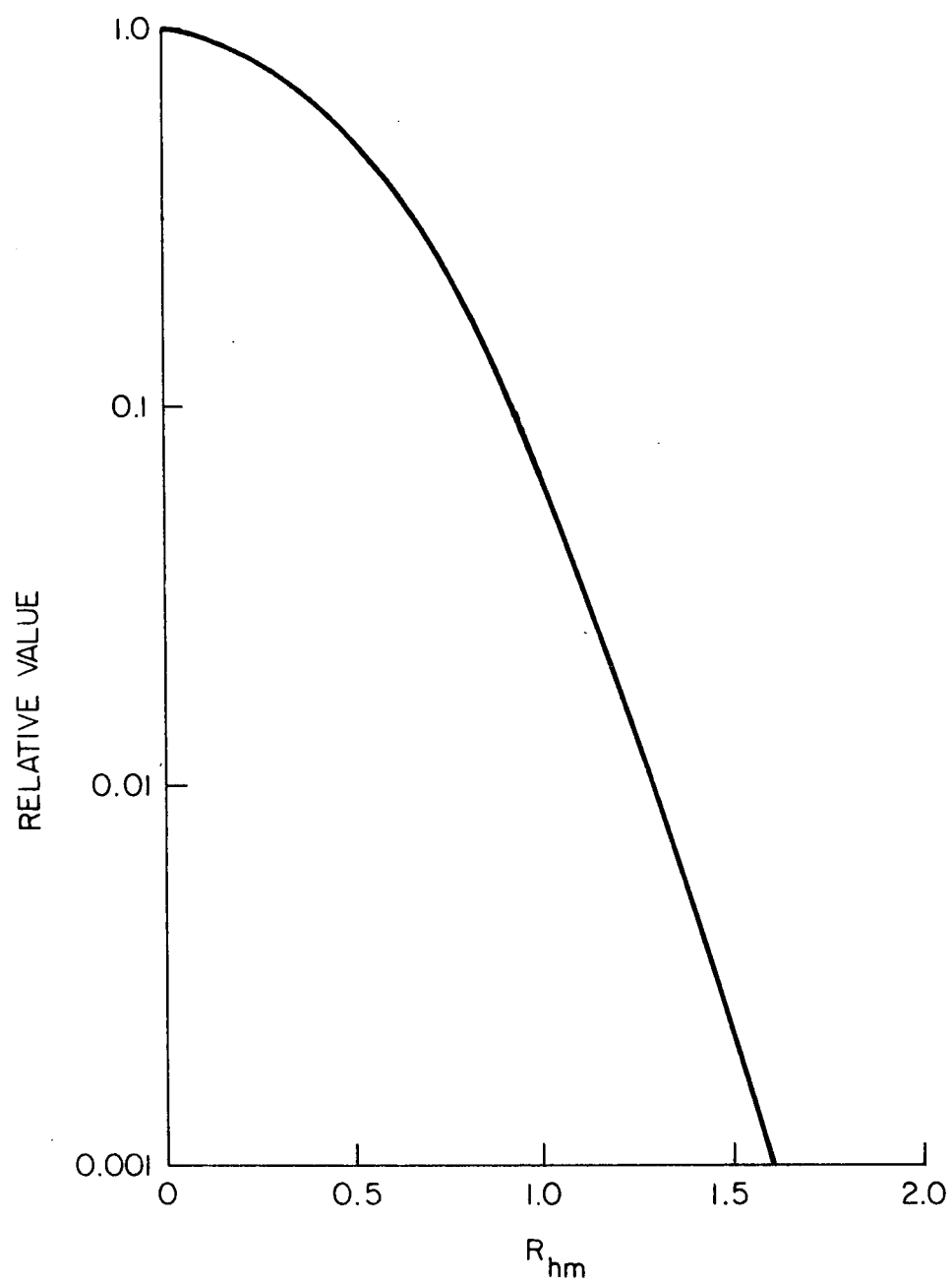
Figure 17. Normalized Gaussian distribution in terms of full
width at half-maximum (Rhm) units.

48

energies in their study. If this result can be applied approximately to SiO_2 bombarded by phosphorus ions in the 20-30 KeV energy range, then roughly one atomic layer will be sputtered off with the incidence of 6 x 10^{14} ions/cm^2 ($SiO_2 \sim 2.33$ x 10^{22} atoms/cm^3).

Contrary to the sputtering effect is the observed elevation of the surface of ion-irradiated materials[41]. This volume expansion is attributed to the highly disordered region at the peak of the impurity distribution at a distance R_p beneath the relatively undamaged surface. Silicon implanted with 400 KeV Xe ions experienced an expansion of 30-125 Å over a fluence range of 10^{13} - 10^{16} ions/cm^2.

In the present research, it is desired to implant a fixed charge in the deposited 700 Å SiO_2 antireflection coating on the surface of a production n/p solar cell. Phosphorus ions are chosen because of the ease of plasma generation, relative immobility in the SiO_2 and compatibility with the surface layer doping. Experimental variables are the position of the peak of the ion density distribution and the total implanted charge.

Several aspects of the ion implantation process limit or affect the proposed benefit of reducing the surface recombination factor which degrades solar cell efficiency.

1. The effective charge in the oxide must be limited to a quantity which does not cause dielectric breakdown. Presumably an excessive electric field at the oxide-Si interface would result in some mechanism such as tunneling of electrons from the silicon to neutralize the implanted ions near the interface.

2. An intangible quantity is the energy and density distribution of the surface states at the surface of the diffused layer. It is well known that high concentrations of impurities will cause lattice strains which not only reduce bulk lifetime, but also contribute to surface states. Local precipitations of diffusant or diffusant-silicon complexes should be considered as well. How well the post-diffusion etch will improve these conditions is unknown. Similarly, apparently vacuum-deposited SiO_2 has not been studied with regard to its influence upon a silicon surface.

3. Possible damage to the silicon surface and bulk due to the tailing of the ion distribution may actually increase the fast surface state density. Gianola[42] has measured the surface recombination velocity by the photomagnetoelectric technique of silicon bombarded with 30 KeV helium ions. It was found that the surface recombination velocity increased by 50 times. Snow, et.al.[43] examined the effects of high and low energy electrons, x-ray and ultraviolet radiation on Si surfaces. One interesting point is the annealing by ultraviolet light (energy $\geq$ 4.3 eV) of the x-ray induced oxide space charge. There is a rather sharp annealing threshold at the 4.3 eV $Si-SiO_2$ barrier energy. Thermal annealing becomes apparent at temperatures above 125°C.

The volume density of implanted ions at the $Si-SiO_2$ interface is down by a factor of one hundred from the peak density for a Gaussian ion distribution centered in a 700 Å oxide layer. For an implant dose of 10^{12} cm^{-2}, this density at the interface is $\simeq$ 3.5 x 10^{16} cm^{-3}.

Implantation would be expected to decrease the Si bulk and surface lifetimes because of the residual lattice damage. Thermal annealing simply converts the implanted ions (P^+ in the present investigation) into additional donor centers in the silicon. However, the relatively high annealing temperatures required (400-500°C) would probably eliminate the oxide charge distribution as well.

4. A final extraneous feature of the oxide processing is the alteration of its optical properties. Thickness changes may occur as a result of sputtering or expansion during bombardment. An increase in scattering and a change in index of refraction are the consequences of introducing an impurity into the oxide. These parameters control the antireflection nature of the oxide layer.

NATURE OF EXPERIMENTAL INVESTIGATIONS

Some of the experimental questions which need to be answered in an investigation of the contribution of surface or interface recombination losses in the surface n region of n on p solar cells using charge introduction by ion implantation into the oxide antireflection coating to monitor charge effects on surface recombination include the following:

1. What is the value of the A factor in the $I = I_0 \exp \frac{eV}{AkT}$ relationship characterizing the cells investigated; that is, what role do junction recombination currents play in controlling I_{SCC} of the cells.

2. Does the method of charge introduction into the oxide actually produce negative or positive charge effects which shift the surface potential. MOS capacitor measurements on implanted and nonimplanted oxides will reveal by the shift along the voltage axis the quantity and polarity of charge that has been introduced into the oxide.

3. Will illuminated transparent electrode-insulator-solar cell structures show variation in solar cell efficiency as a function of applying positive and negative voltages across this MOS structure. If surface potential variation by induction is effective in changing N_{st} occupancy and surface recombination velocity, this experiment should show changes in I_{SCC} with applied voltage.

With such information available for validation and reference, ion implantation of charge at various depths into the oxide layer and for various dosages along with measurements of I_{SCC}, V_{OC} and I-V integral response characteristics and spectral response characteristics before and after implant with particular attention focussed on the blue response region can be conducted to obtain data which should be interpretable as to whether charge introduction by ion implantation will produce an increase or decrease in the blue response efficiency of solar energy conversions by the Si solar cell.

The experimental investigations undertaken in this preliminary study were directed at providing the above types of information.

These investigations are reported in this order in the following sections. First however, the experimental apparatus, procedures and techniques are described.

EXPERIMENTAL APPARATUS AND PROCEDURES

Nonilluminated Cell Current-Voltage Measurements

Nonilluminated Si solar cell I-V characteristics were measured by varying the forward bias on the cell as shown in Figure 18. The contact jig for the cell was the same one used in recording the I-V characteristics of these cells under various levels of illumination in order to determine the series resistance. These illuminated I-V characteristics were recorded with a X-Y plotter to facilitate the series resistance calculation.

MOS Capacitor Measurements

When the bias voltage on a metal-oxide-semiconductor (MOS) capacitor is varied, the resulting capacitance-voltage characteristics for an ideal device will analytically depend upon the uniform impurity density in the semiconductor, N_d, and the oxide thickness, x_o. A significant point on the C-V curve is the value of capacitance for which the semiconductor surface potential is zero, i.e., the energy bands are flat from the bulk to the surface. Ideally this occurs for a zero gate bias voltage, $V_g = 0$. If the semiconductor doping and oxide thickness are known, it is possible to calculate the ratio of the flatband capacitance to the oxide capacitance, C_{FB}/C_{ox}[31]. In experimental devices the C_{FB}/C_{ox} ratio does not appear at zero gate bias. This is the result of a metal-semiconductor contact potential, surface charge at the oxide-semiconductor interface and charge in the bulk of the oxide. This latter effect results in a flatband voltage shift of

54
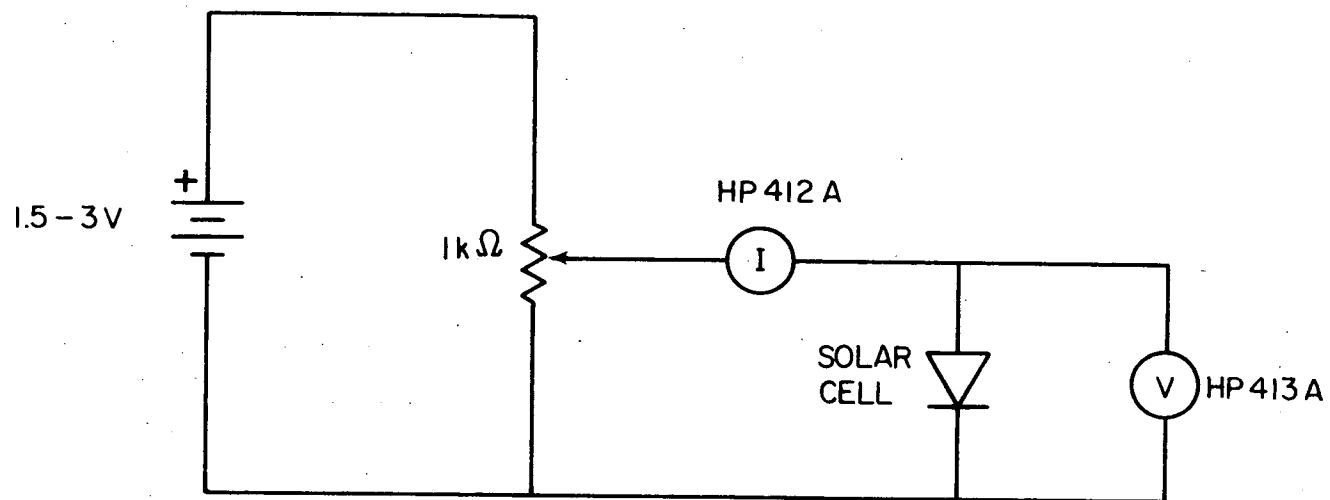
Figure 18. Circuit for measuring nonilluminated solar cell current-
voltage characteristics under forward bias.

$$\Delta V_{FB} = - \frac{1}{C_{OX}} \int_0^{x_O} \frac{x}{x_O} \rho(x) \, dx, \tag{18}$$

where C_{OX} is the oxide capacitance per unit area, x is distance measured into the oxide from the metal gate electrode, and $\rho(x)$ is the volumetric charge distribution within the oxide[12].

By assuming the Gaussian distribution of implanted positive ions in the oxide it is possible to calculate the flatband voltage shift due to the implanted charge.

N-type 1-4 ohm-cm polished Si wafers were oxidized in dry oxygen at 1050°C and quenched in nitrogen gas. The resulting thermal oxide thickness was approximately 1000 $\overset{o}{A}$ by comparison with oxide color charts. Gold was evaporated and alloyed into the back Si surface. Sections of these wafers were ion implanted at various energies and fluences. Aluminum dots 0.5 mm in diameter were evaporated through a mask to form the gate electrode after implantation.

Capacitance-voltage measurements were performed on a Boonton Capacitance Bridge 74C-S8 (100 KHz) which contains a variable bias supply. In some cases the wafers were heated, either under bias or open-circuited, to various temperatures to determine the stability of the implanted ions. The contribution to flatband voltage due to the contact potential and surface state charge was determined by measuring nonimplanted MOS capacitors.

Transparent Field Electrode-Insulator-Solar Cell Structure Measurements

By applying an electrostatic field normal to the surface of an illuminated solar cell, it is possible to observe the effects of surface

56

potential variations upon the cell output characteristics. Presumably, since surface potential variations are expected to alter the diffused region short-circuit current via changes in recombination velocity, the output parameter to be observed is the short-circuit current due to short wavelength (blue) optical excitation. The maximum variation in surface potential will be determined by dielectric breakdown, and the density and distribution of semiconductor surface states.

A liquid electrolyte was first tried as the field electrode on the oxide-coated solar cell. A small glass tube ($\sim$ 7 mm I.D.) was waxed to the cell to provide an electrolyte reservoir. It is necessary to insulate the cell surface contact grid from the electrolyte solution. Various waxes, photoresists and resins were tried but conduction still occurred between the electrolyte and the cell surface. It also appeared that the oxide layer had pinholes which formed conducting electrolyte paths to the cell surface.

Anodic oxidation was considered as a remedy for the pinhole problem, but a suitable contact grid insulator was still necessary in order to anodically oxidize any appreciable area of the cell, as well as during the application of the electric field.

Because of the above difficulties, the liquid electrolyte field electrode was discarded in favor of a glass plate with a transparent electrically conducting coating (Corning Glass Works). A contact grid insulator was still necessary; this was either 1/2-mil Kapton or approximately

F

1/2-mil mica. Silicone oil was used to improve the dielectric contact to both sides of the insulating spacer. The cell current was measured under tungsten lamp illumination (and various filters) as the voltage applied to the field electrode was varied. The experimental configuration is shown in Figure 19. Cell output was measured across the 15-ohm load resistance with a Leeds and Northrup K-3 potentiometer.

Besides the n/p Si solar cells supplied by JPL, we also had available some p/n GaAs solar cells (approximately 7% efficiency).

Most illuminated measurements were made with a blue CS 5-61 glass filter (Corning Glass Works).

Ion Implantation Apparatus

The ion implantation apparatus employed in this research is shown schematically in Figure 20 and in perspective in Figure 21. The target holder is shown in Figure 22. The phosphorus source is powdered red phosphorus which is heated by means of a tungsten halogen lamp in a focusing reflector to increase the vapor pressure. An external coil couples a 12 MHz oscillator to the vapor to produce ionization. Focusing and defining apertures form the accelerated P^+ ions into a 5 mm-diameter beam at the substrate plane. Since the amorphous SiO_2 layer on the solar cells stops (and scatters) the majority of the ions, no attempt was made to angle the solar cell with respect to the incident beam in order to reduce channeling effects.
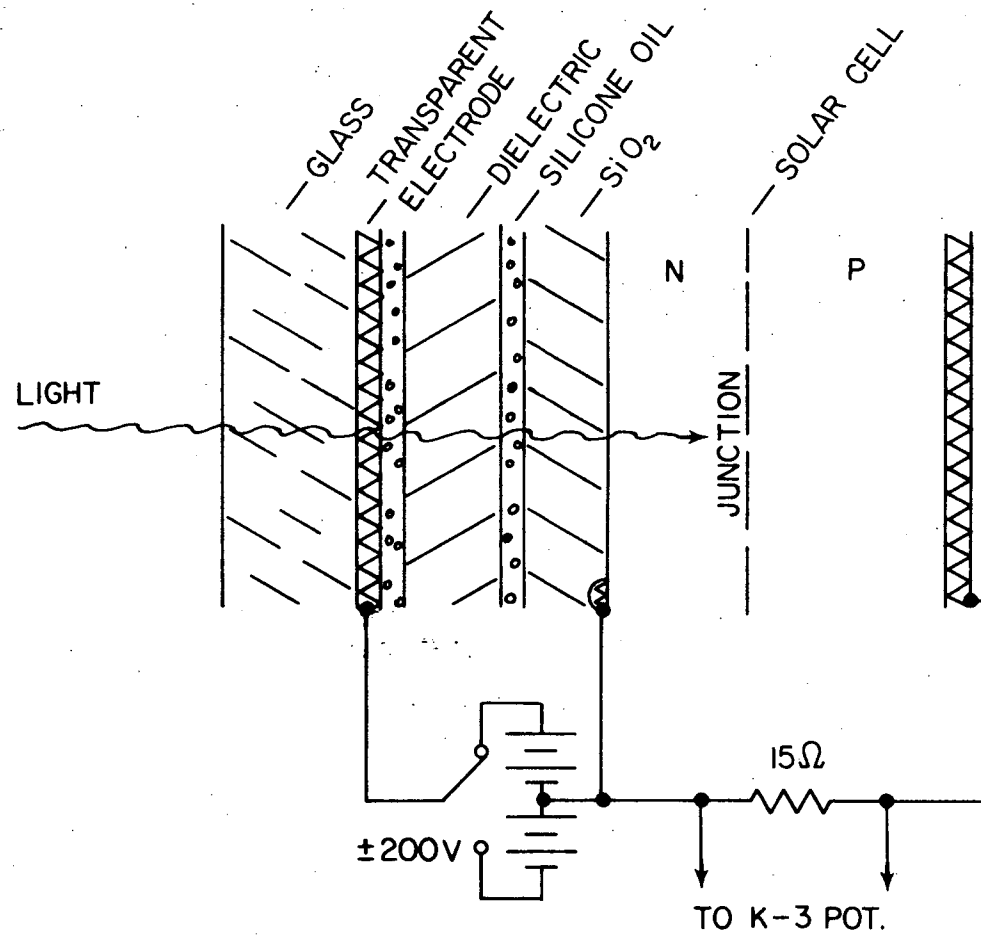
Figure 19. Schematic of transparent field electrode measurements on solar cell.
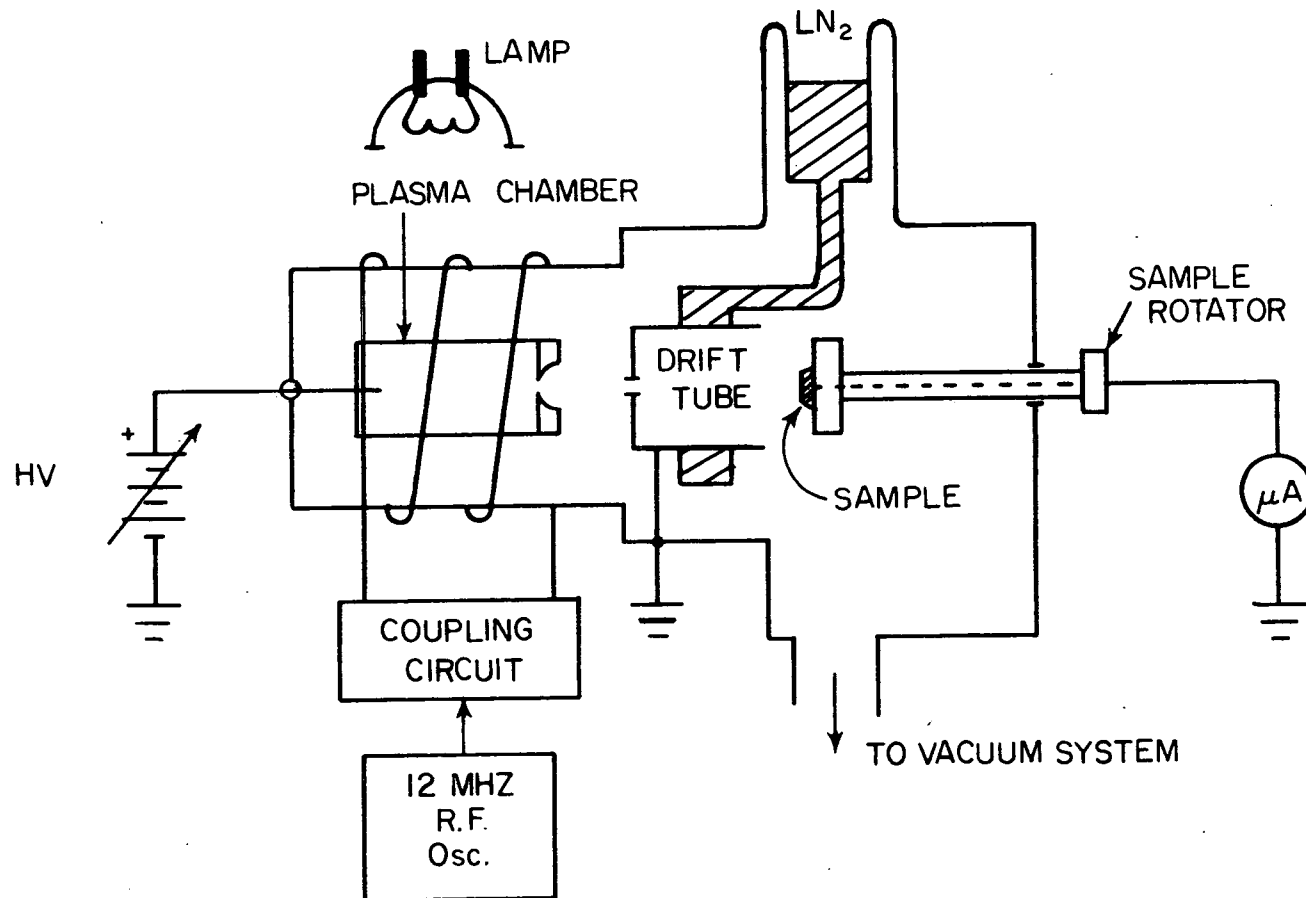
Figure 20. Schematic of ion implantation apparatus.
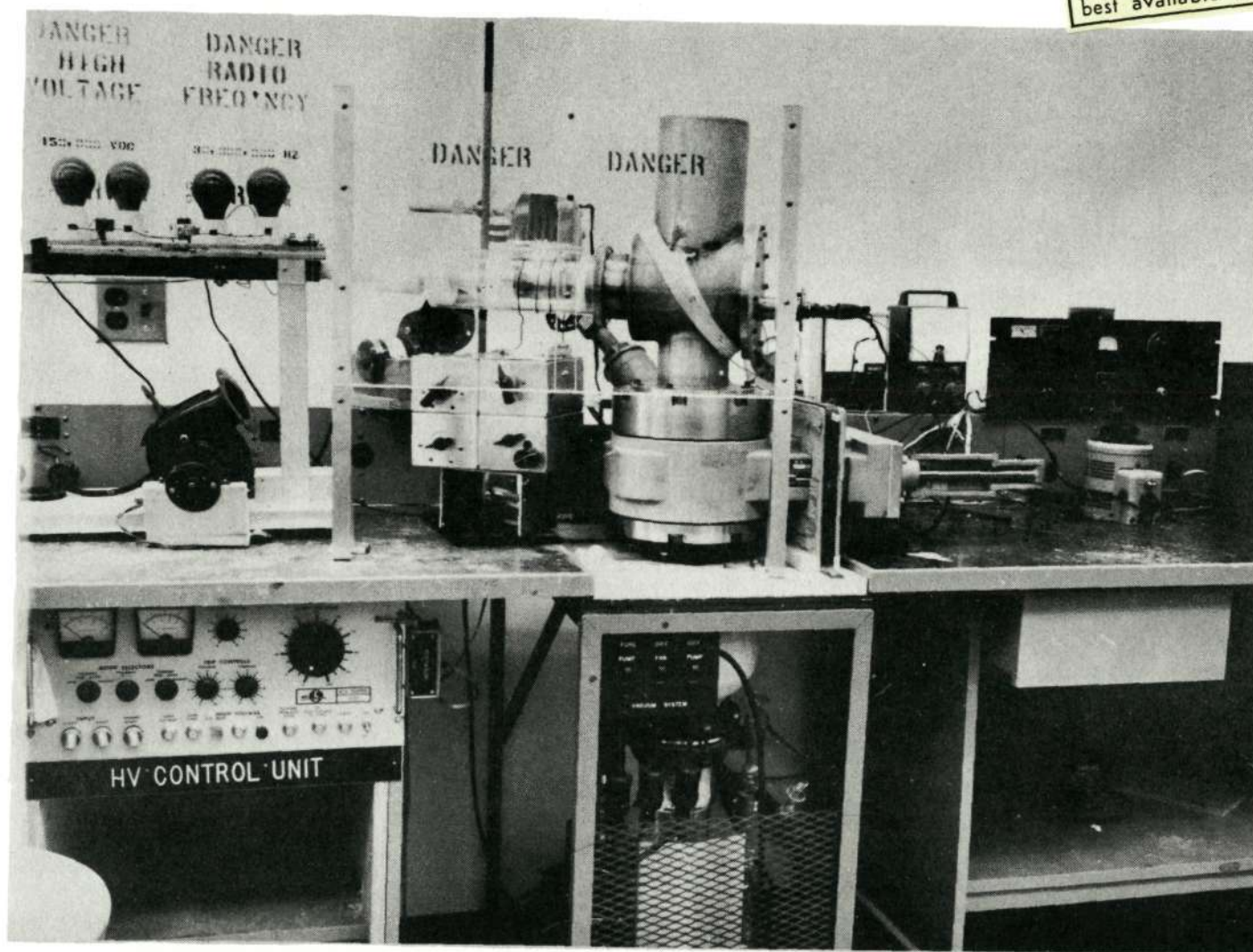
Figure 21.   Ion implantation system.
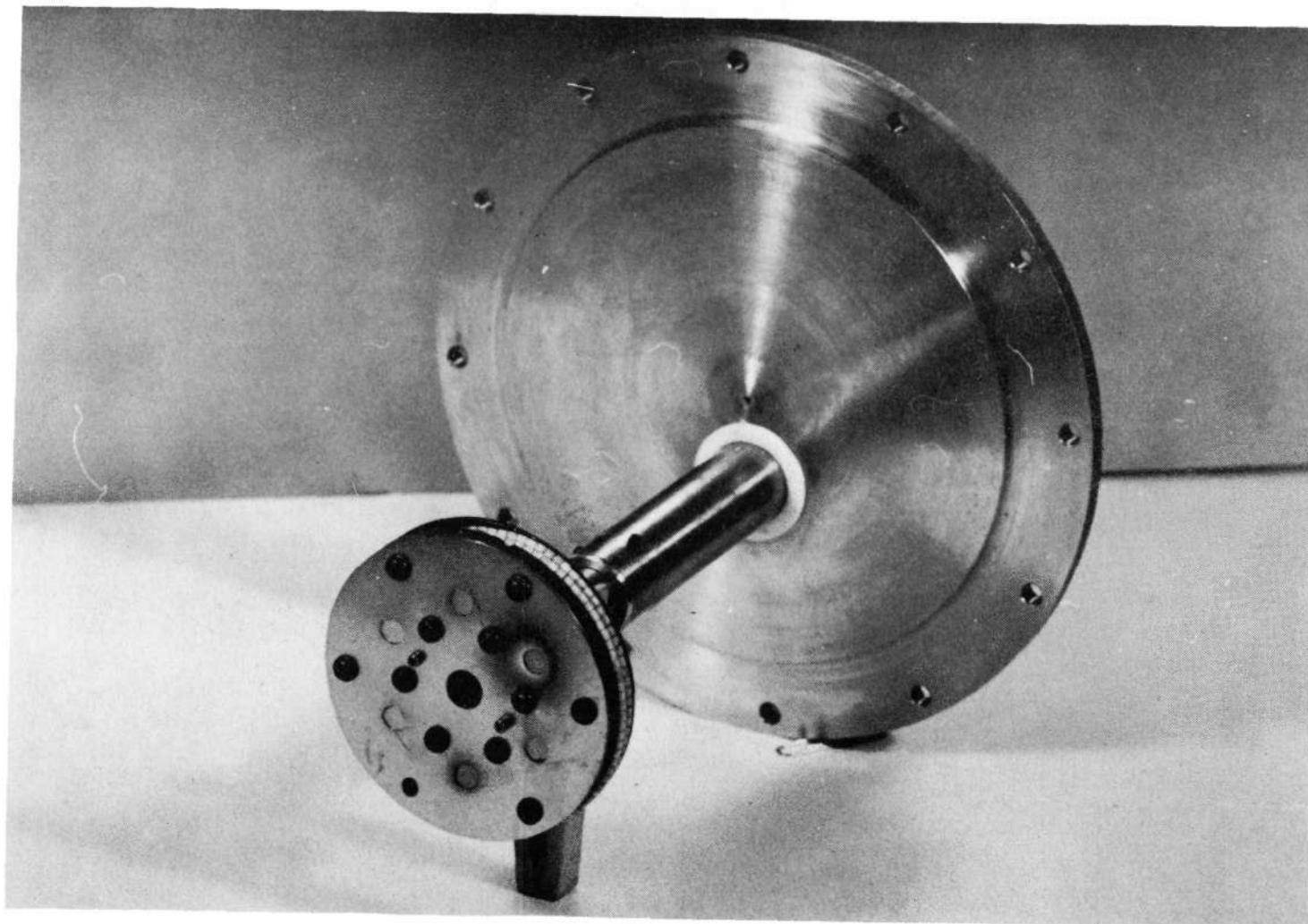
Figure 22. Substrate holder for ion implantation.

System vacuum of 10^{-5} Torr with the plasma are obtained with an oil diffusion pump and liquid nitrogen cold trap. Additional liquid nitrogen trapping surrounds a portion of the implantation chamber. A feedthrough electrode connects the plasma to the variable high voltage power supply. The drift tube and substrate are at ground potential. Since the ion current is fairly constant, it is possible to obtain the quantity of implanted charge from the product of implantation time with the current in the microammeter coupling the insulated sample holder to ground. The indexed rotating vacuum seal enables up to six samples to be implanted during a single pumpdown.

Previously, the system described above has been used in studies of phosphorus-ion-implanted CdS[44].

Power Supply for I-V Monochromator Measurements

The power supply used to provide power for the lamps used in both I-V and monochromator measurements is shown in Figure 23. The 10A autotransformer controls the line power up to 1 kW. The 5A is connected in parallel such that a fine adjustment is possible by connecting 110 V to a 6.3 V transformer in series with the main power line.

An ammeter with a mirror background is in series to help obtain accurate readings of the line current. A Sola constant voltage transformer is used to eliminate small fluctuations in the line voltage.

Set Up for Monochromator Measurements

Monochromator measurements were made on all cells as shown in Figure 24. To have a uniform beam over the face of a solar cell, cells

63

AMMETER (0−10A)

MONOCHROMATOR LAMP OR
SUN LAMP, GE 39, I kW HIGH
INTENSITY LAMP

10 A
VARIAC

IIOV : 6.3 V

5A
VARIAC

SOLA CONSTANT
VOLTAGE TRANSFORMER
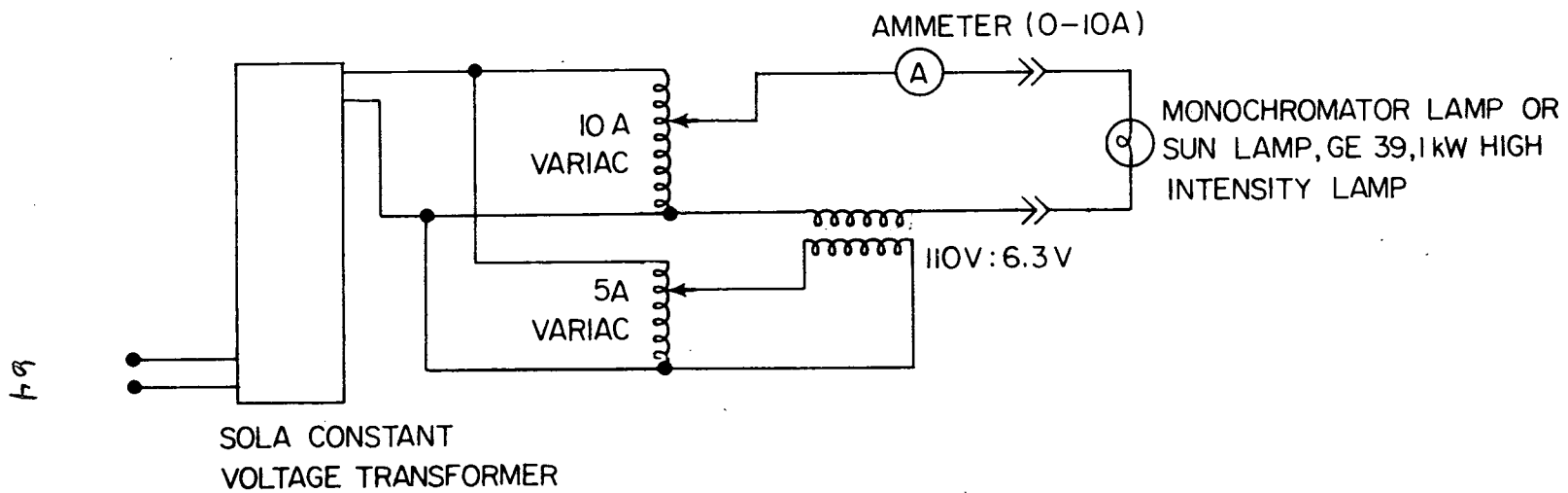
Figure 23. Power supply for I-V and monochromator measurements.

B & L 33−86−02
MONOCHROMETER

EPPLEY THERMOPILE
FOR CALIBRATION

148 KEITHLEY
NANOVOLTMETER

3500Å −8000Å

56.2 Ω
1%

CELL HOLDER
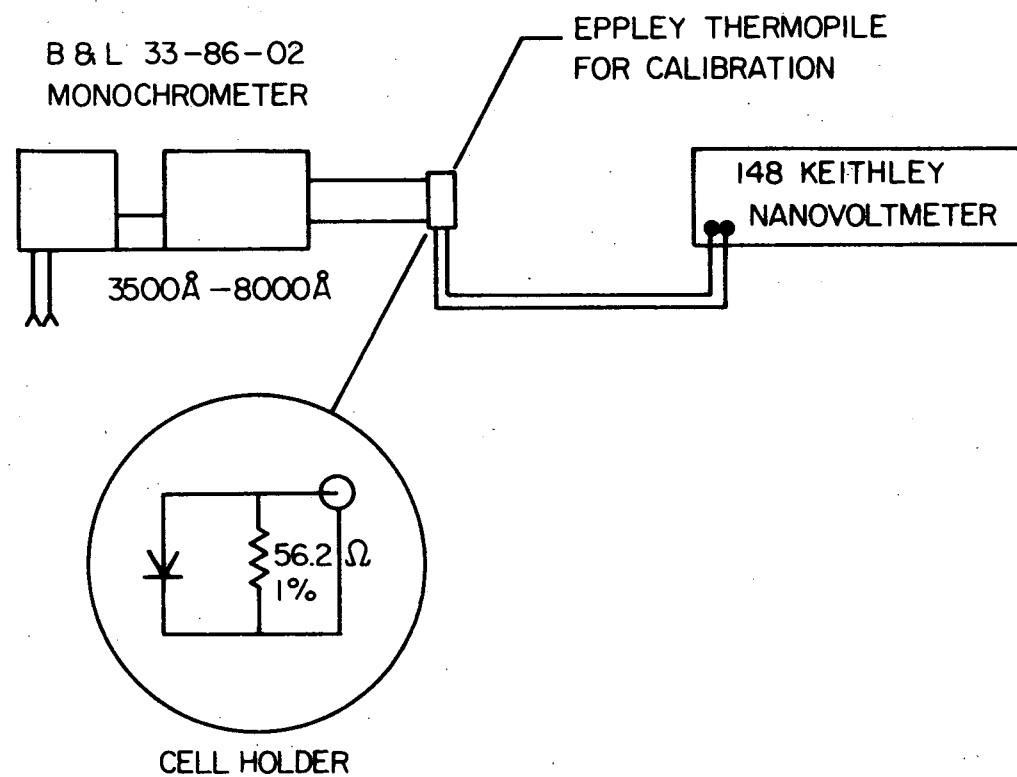
Figure 24.   Set-up for monochromator measurements.
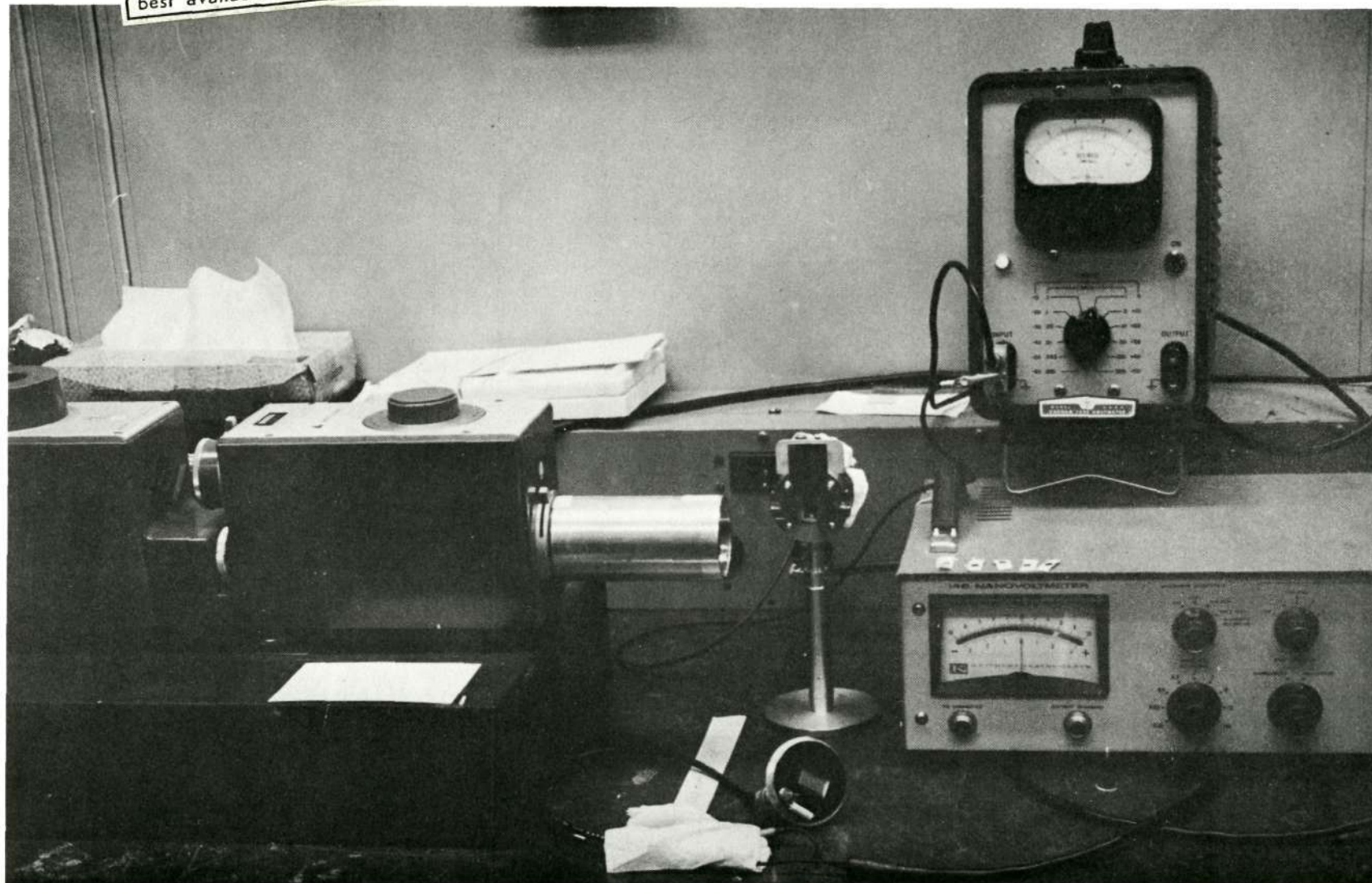
Figure 25. Spectral response measurement apparatus.

are separated by 4-3/4" from the monochromator exit slit guided by a cylinder painted black inside. Cells are mounted at the end of the cylinder.

An Eppley thermopile was used to calibrate the system and a Keithley 148 nanovoltmeter was used for the measurements of cell response. All the connections and wires are appropriately shielded from the environment during the measurements. A photograph of the arrangement is shown in Figure 25.

I-V Measurement Apparatus and Method

OCV, I_{SCC} and I-V measurements were made as shown schematically in Figure 26. A secondary standard cell and a test cell are mounted on the same brass holder with a relatively large volume to provide a heat sink. These are connected with a switch S, which allows a quick check with the secondary standard cell of the flux level whenever necessary. The secondary standard cell was calibrated with a standard cell obtained from JPL.

The short circuit currents are measured by extrapolating currents through the set of calibrated resistors ranging in values from 1Ω-9Ω under 139.6 mW/cm^2 sec radiation level.

Two 1.5V batteries in series with 1 KΩ, 10-turn potentiometer, is used as a cell biasing circuit for X-Y recorder plots of the I-V characteristics. A 27 Ω resistor in series with a solar cell is used to determine cell current. A photograph of the arrangement is shown in Figure 27. Figure 28 shows a close up view of the sample and secondary standard cell holder along with the standard calibrating cell and lamp.

1.5 V

1.5 V

1 kΩ
10-TURN
POTENTIOMETER

SUN LAMP
G E 39. 1 kW
HIGH INTENSITY LAMP

27Ω

MOSELEY
7005 A

X-Y RECORDER

TEST CELL

S

STANDARD CELL

KEITHLEY 602
ELECTROMETER

ACCURATE RESISTANCE
1-9Ω

SWITCH
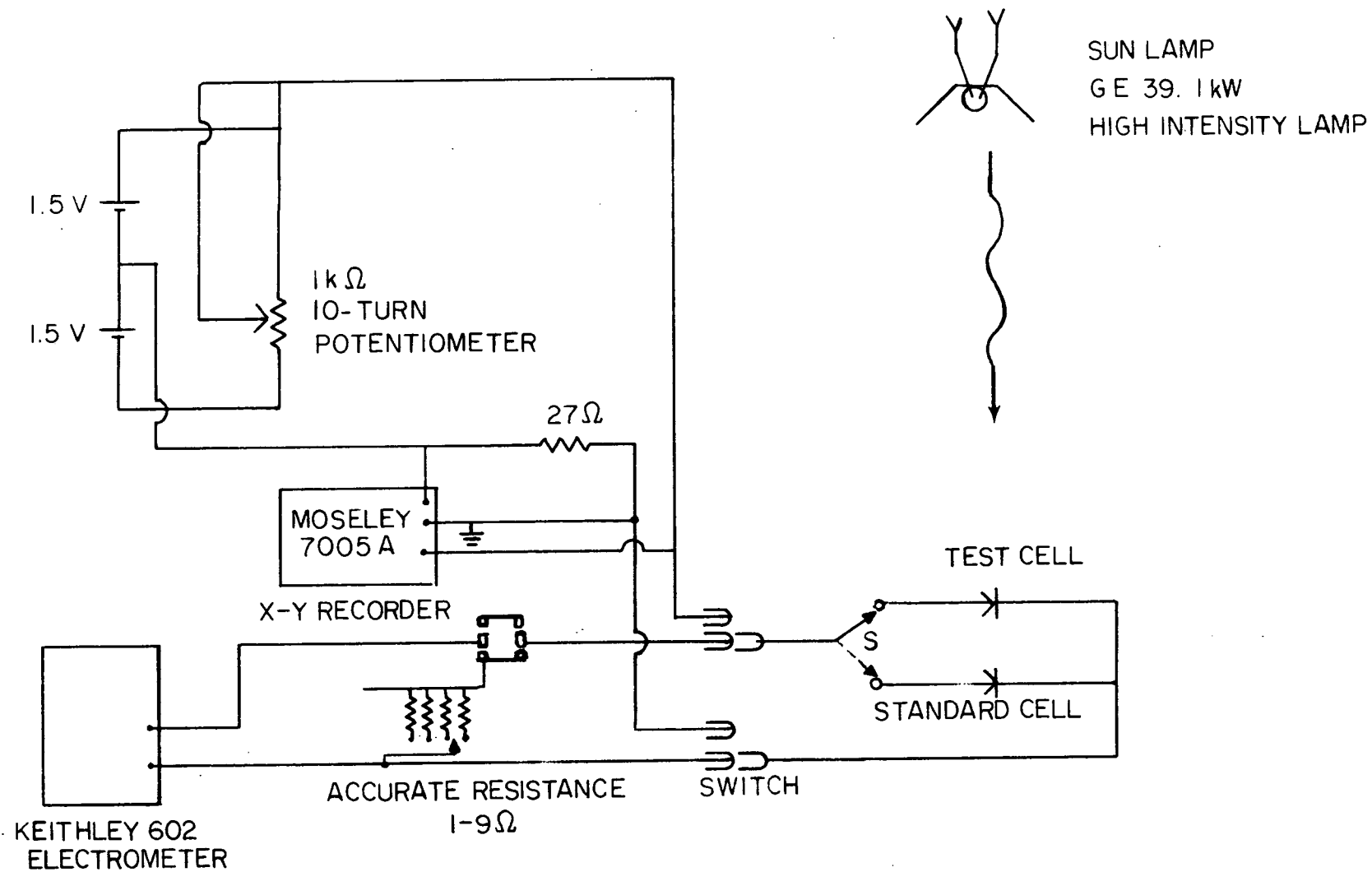
Figure 26. Circuit diagram for OCV, I_{SCC} and I-V measurements.

69
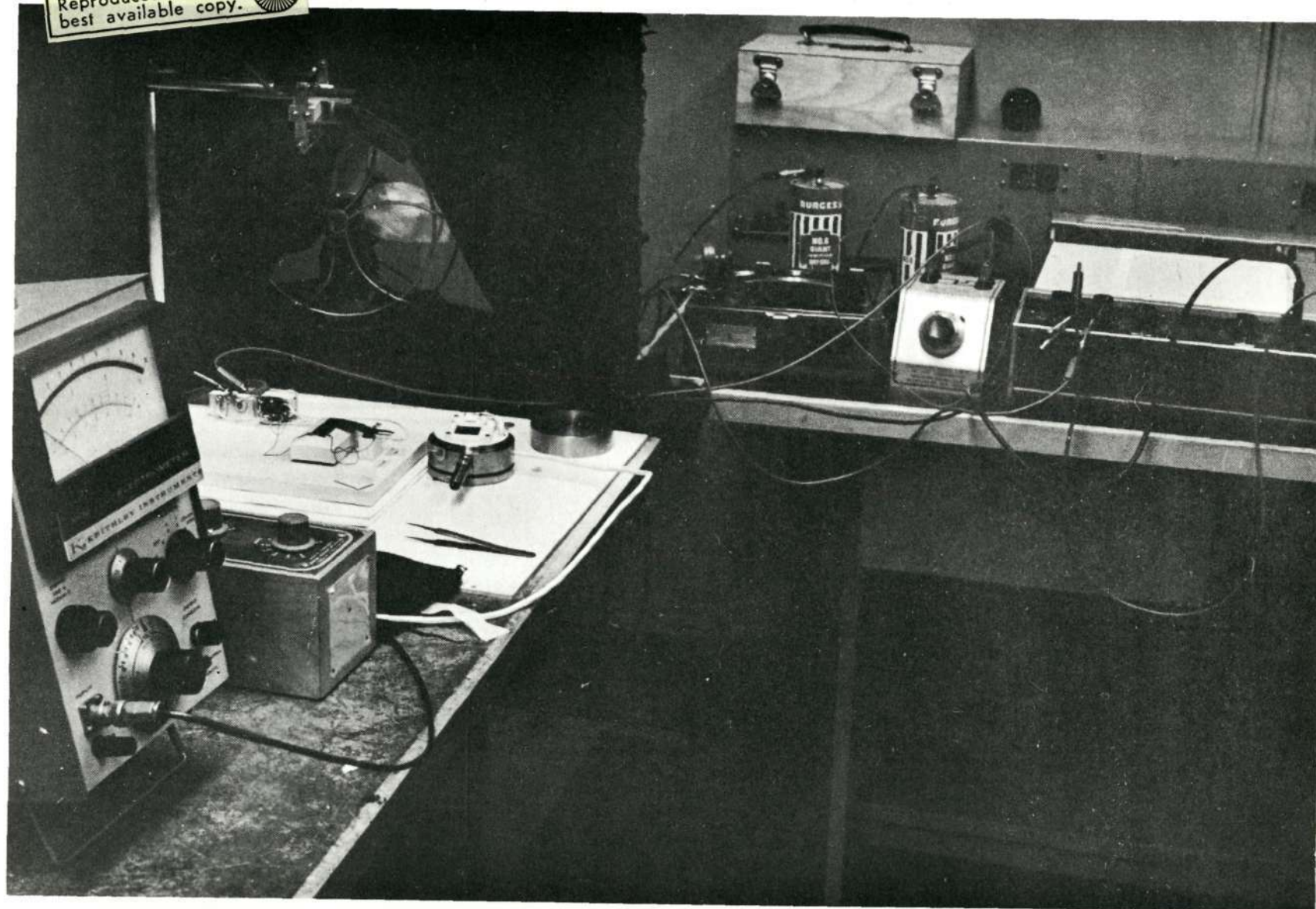
Figure 27. Set-up for OCV, I$_{SCC}$, and I-V measurements.

70
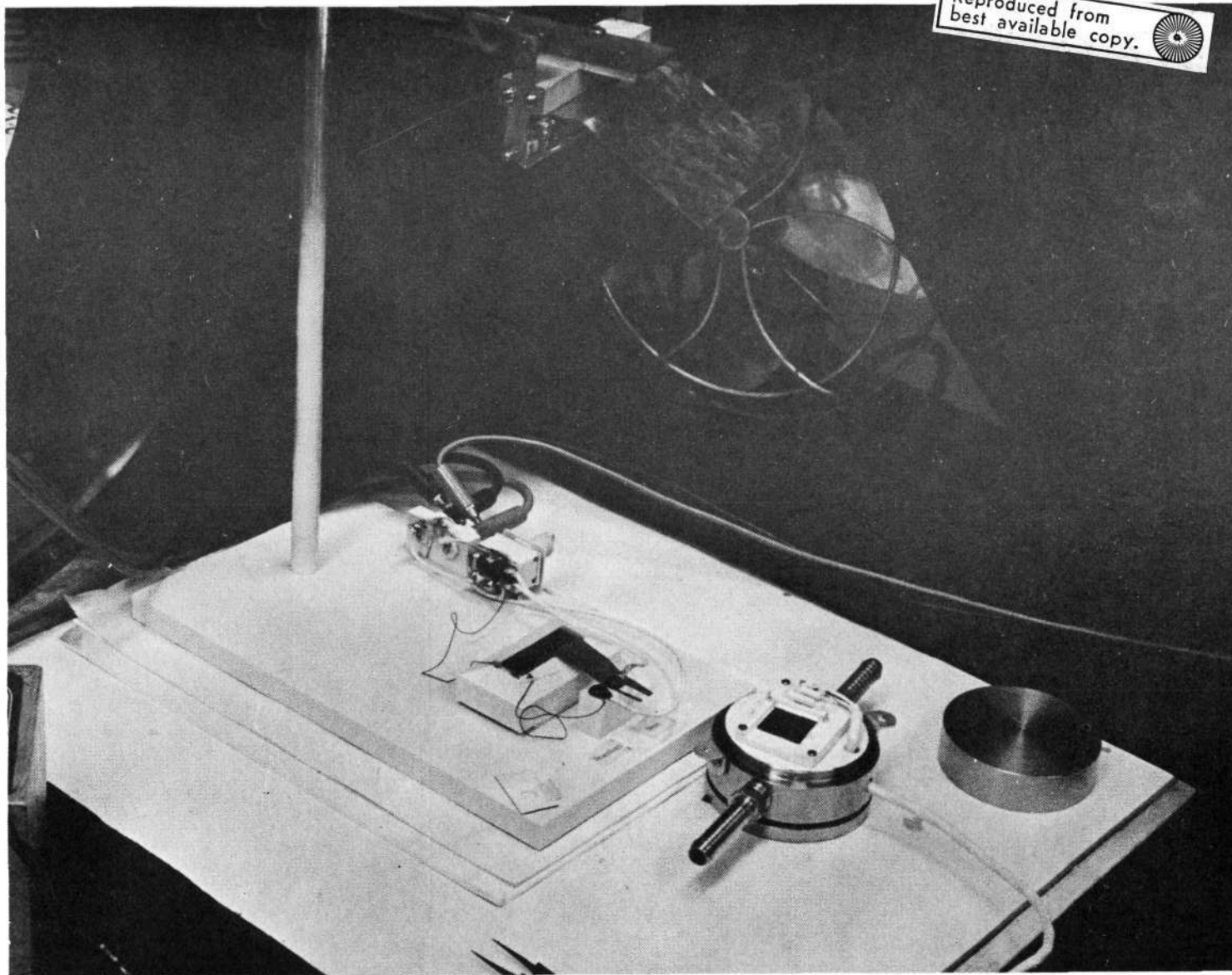
Figure 28. Close-up view of OCV, I_{SCC} and I-V measurement set up.

Apparatus and Technique for Measurement of Reflectance

Since implantation can change the spectral behavior of the cells, measurements were made using a Cary 14 spectrophotometer to determine reflectance changes after ion bombardment. Measurements were made by providing the sample beam with a reflectance attachment. The only slide wire available at the time was for absorbance A, where $A = \ln 1/T$, and T is the transmitted, or for our case, the reflected beam. No means were available however, to obtain a measurement of the amount of incident radiation scattered from induced defects in the oxide or silicon surface layers.

EXPERIMENTAL RESULTS

Nonilluminated Cell I-V Characteristics

In previous experiments in which the current-voltage character-
istics of the solar cells under various levels of illumination were re-
corded, the series resistance was found to be considerably less than 1 ohm.
Thus, no correction was applied to the nonilluminated I-V data for series
resistance. In some cases the data was obtained with a high input impe-
dance battery-operated voltmeter or a d'Arsonval ammeter.

The V vs. log I data for the nonilluminated cells is not linear
in general. The value of A in the expected $I = I_0 \exp(qV/AkT)$ relation-
ship was calculated at room temperature and V = 0.45 volt. For the three
cells measured, this A value was greater than two. I-V characteristics
for various cells and the A value at V = 0.45 volt are shown in Figure 29.
The A values are compared with previous reports for n/p cells in Table 1.
A recent communication* indicates that the measured A value for this type
of cell actually lies in the 1.3-1.35 range. No explanation is presently
available for this discrepancy, unless it is a consequence of neglecting
the series resistance or perhaps an unrecognized circuit factor.

MOS Capacitor Measurements

By comparing the ratio of minimum capacitance in inversion to
the oxide capacitance (strong accumulation), the best fit of experimental
data occurs for $x_0 = 1000$ Å, $N_d = 1 \times 10^{15}$ cm^{-2} [31]. From the ideal MOS
curves[45] $C_{FB}/C_{ox} \approx 0.7$. Aluminum on n-type Si with $N_d = 10^{15}$ cm^{-3} has
a contact potential of $- 0.32$ volt[31].

---

* Dr. Richard Stirn, JPL.
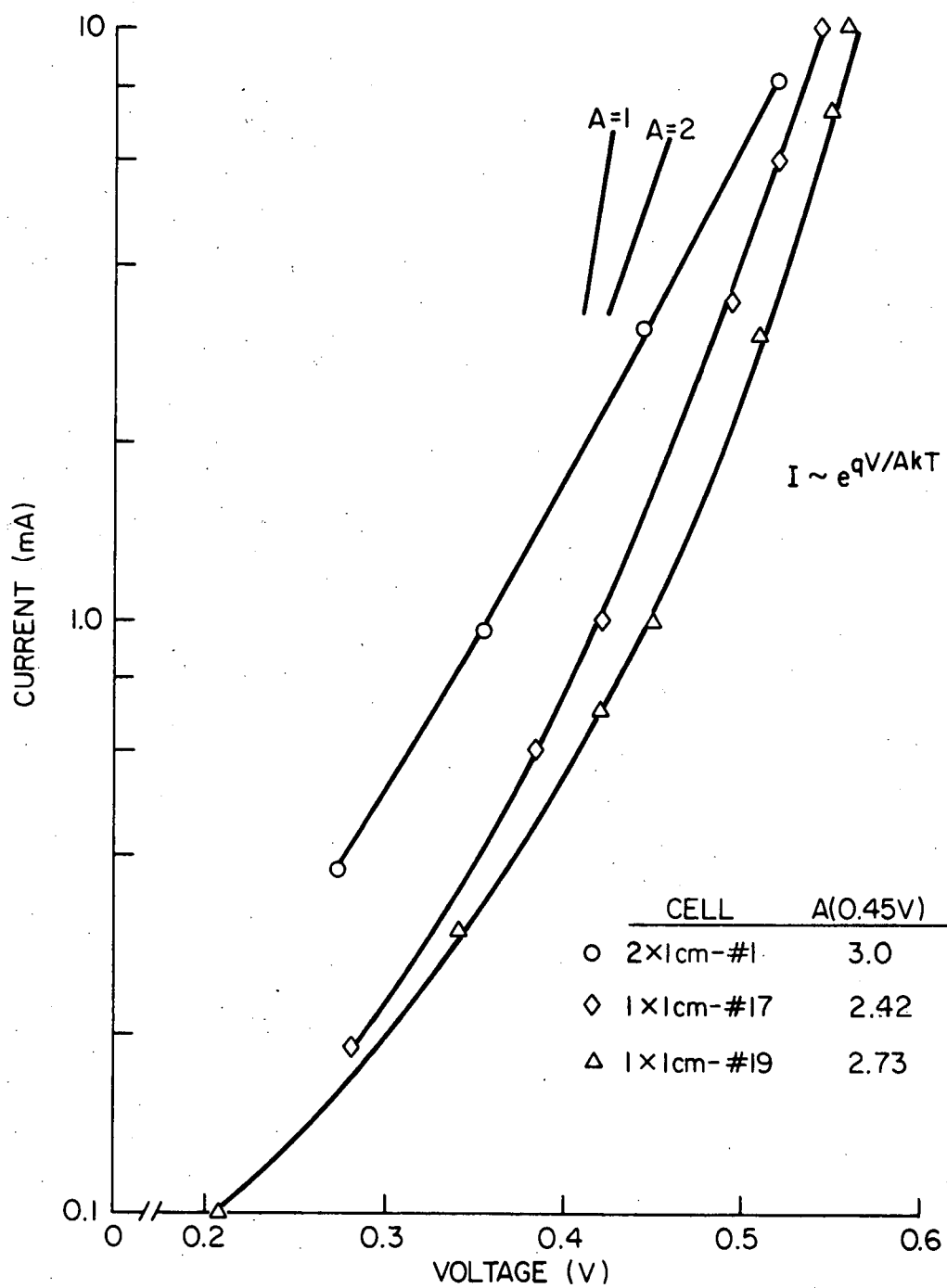
Figure 29. Forward current-voltage curves for Si solar cells.
A-values determined at V = 0.45 V.

73

TABLE 1.   VALUE OF A IN CELL I-V RELATIONSHIP

A	Cell	Reference
1.95	n/p, Mandelkorn	(2)
> 2	n/p, Wolf	(48)
2.4-3.0	n/p, Centralab	This research

TABLE 2.   INFLUENCE OF HEAT TREATMENT UPON FLATBAND VOLTAGE

Heat Treatment	Total ΔV_{FB} (volts)
Initial	$-$ 10.5
10 hr @ 63°C	$-$ 9.5
10 hr @ 106°C	$-$ 5.5

In Figure 30 are the results of C-V measurements on unimplanted MOS devices. With $C_{FB}/C_{ox} = 0.7$, a flatband voltage shift of -2 to -3 volt is apparent. Implanted MOS devices are illustrated in Figure 31 for various energies and fluences. The additional negative flatband voltage of devices in Figure 31 over that in Figure 30 is attributed to the implanted positive charge in the oxide layer. Distortion of the C-V curves is due to fast surface states. Included in both figures is the ideal MOS C-V curve for $x_o = 1000$ Å, $N_d = 10^{15}$ cm^{-3}.

Heat treatments were performed in order to determine the thermal stability of the implanted charge. One 20-KeV implanted device had a total flatband shift of -13.3 volts. After heating in N_2 at 420°C for 15 minutes, the flatband voltage was altered to - 1.0 volt, essentially the same as an unimplanted device.

Device 2-4-4 (see Figure 31) was heated in the atmosphere while open-circuited. The changes in total flatband voltage are shown in Table 2. The changes occurring in the total flatband voltage of unimplanted devices during the treatments listed in Table 2 were not significant. (Device 2-4-6 in Figure 30 is from the same chip as device 2-4-4; the unimplanted flatband voltage is ≃ - 3 volts.)

Device 30-1 was bias-temperature cycled by applying a constant voltage while heating in the atmosphere to 100°C, removing the bias after the sample had cooled to room temperature. With a negative gate bias the charge distribution in the oxide will tend to drift toward the gate electrode, reducing the magnitude of ΔV_{FB}. A positive gate bias will increase
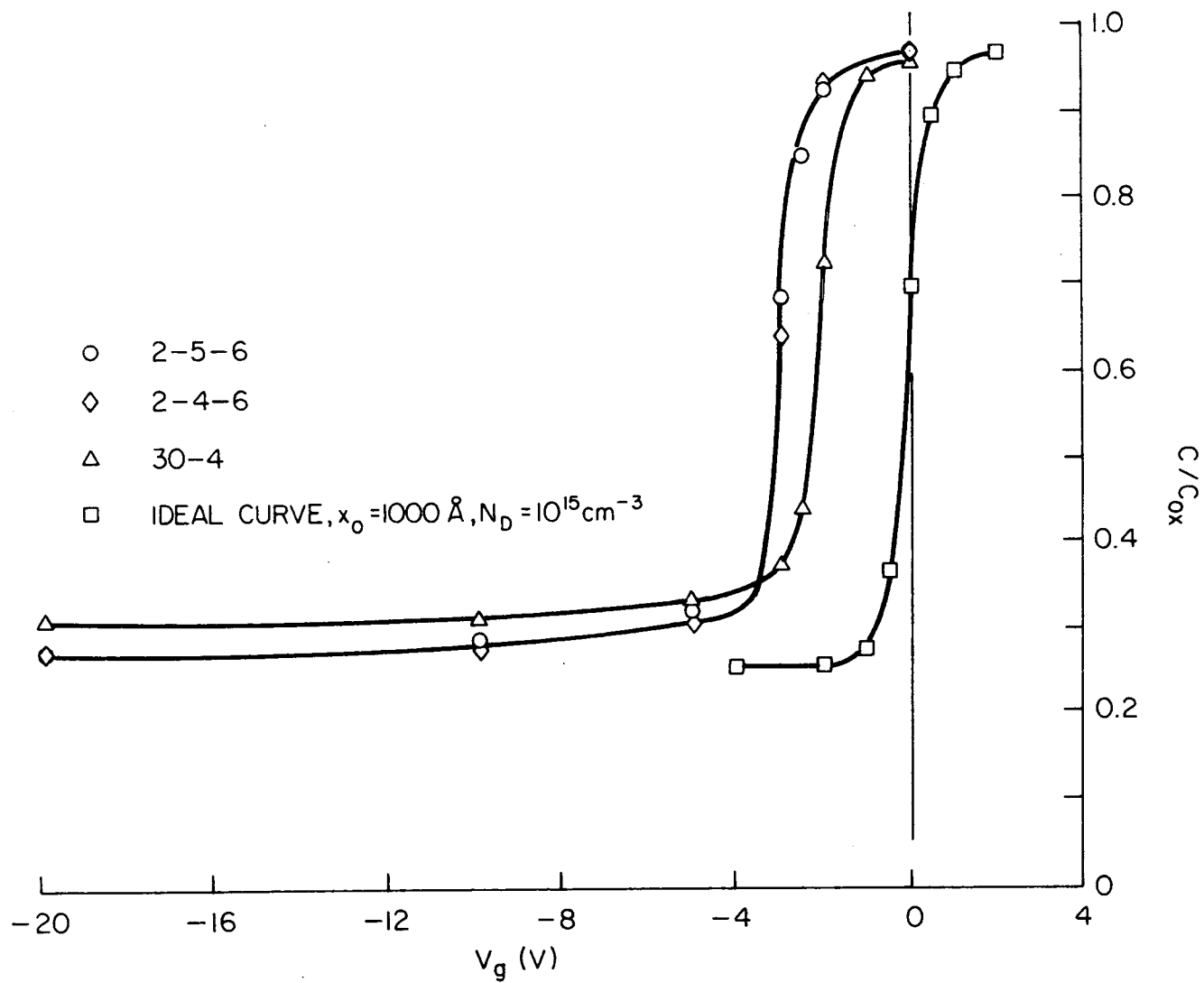
Figure 30. Capacitance vs. voltage for unimplanted MOS capacitors.

The plot legend reads:

- ○ 2-5-6
- ◇ 2-4-6
- △ 30-4
- □ IDEAL CURVE, $x_0 = 1000$ Å, $N_D = 10^{15} cm^{-3}$

Y-axis: C/C_{ox}

X-axis: V_g (V)
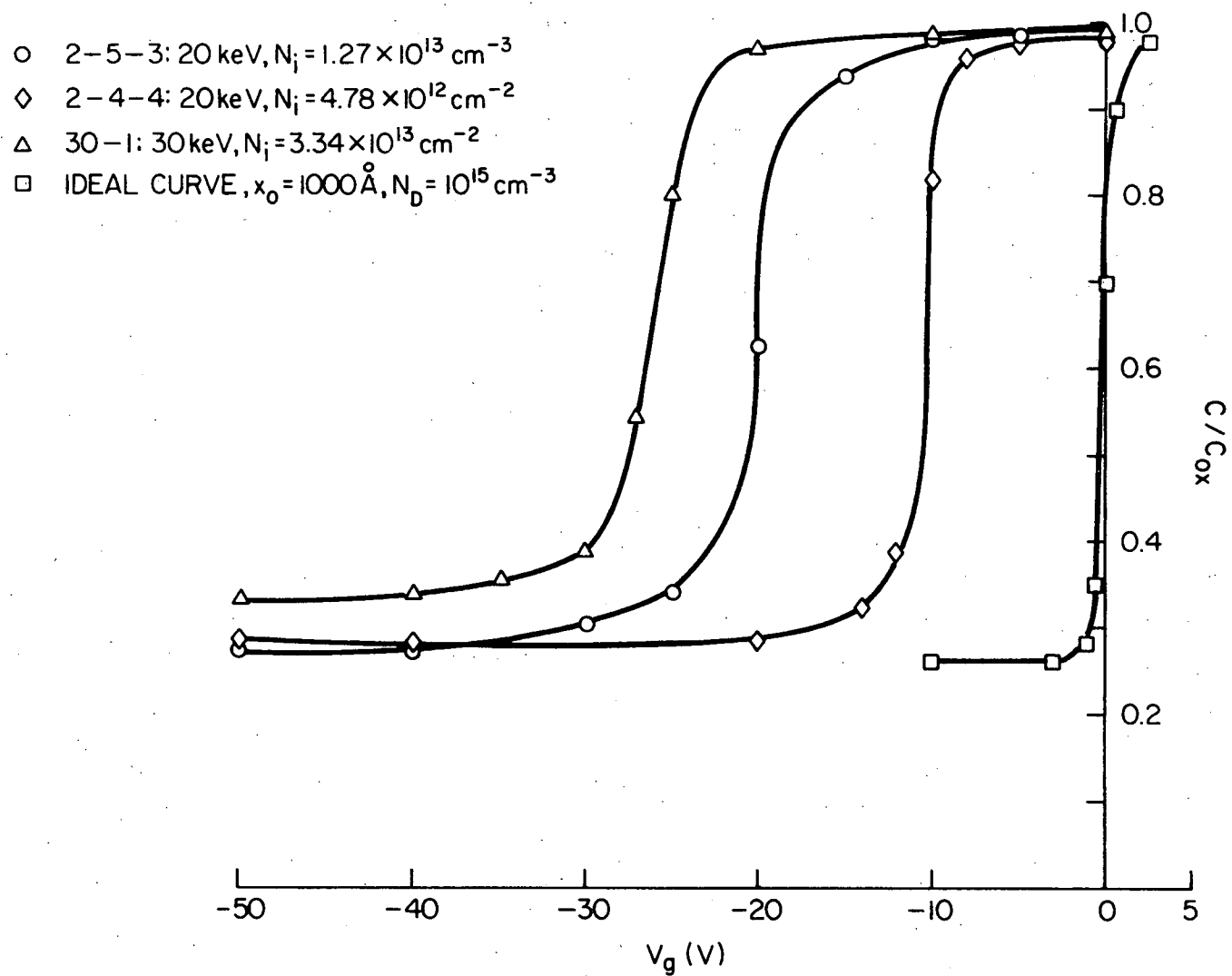
Figure 31. Capacitance vs. voltage for implanted MOS capacitors.

$|\Delta V_{FB}|$ by drifting the charge distribution closer to the oxide-silicon interface. This effect is demonstrated by following the bias-temperature sequence in the C-V characteristics of Figure 32. Curve D was plotted after 40 days of open-circuit room temperature storage. Also observed in the history of device 30-1 are apparent changes in oxide capacitance (heavy accumulation, $V_g = +50$ volts).

Calculated flatband voltages using Equation (18) did not agree favorably with the observed values. Both higher and lower values were calculated for the various implanted samples. In the case of device 30-1 (see Figure 31) for which the oxide-charge induced ΔV_{FB} is -22 volts, the calculated ΔV_{FB} was - 282 volts. The fluence in this case was 2.4×10^{14} ions/cm^2, a value about ten times higher than that predicted to produce dielectric breakdown at the oxide-silicon interface.

Effects of Illuminating of Transparent Field Electrode-Insulator-Solar Cell Structures Under Various Applied Voltages

The external electric field dependence of the cell output was observed by changing the polarity of the transparent electrode with respect to the cell surface contact. Voltages on the order of 200 volts were applied without dielectric breakdown. For the 200-volt electrode polarities no change in the Si cell current was observed. (Microvolt voltage differences can be detected with the K-3 potentiometer.) With the p/n GaAs cells, current changes of $\sim 2 \times 10^{-7}$ A (average current $\simeq$ 4.5×10^{-5} A) were observed; the current increasing when the field

DEVICE 30—I

A: INITIAL
B: FIRST ANNEAL, $V_g = -22.5V$, I hr, 100°C
C: SECOND ANNEAL, $V_g = +22.5V$, 2hr, 100°C
D: AFTER ONE MONTH STORAGE, ROOM TEMP., OPEN CIRCUIT
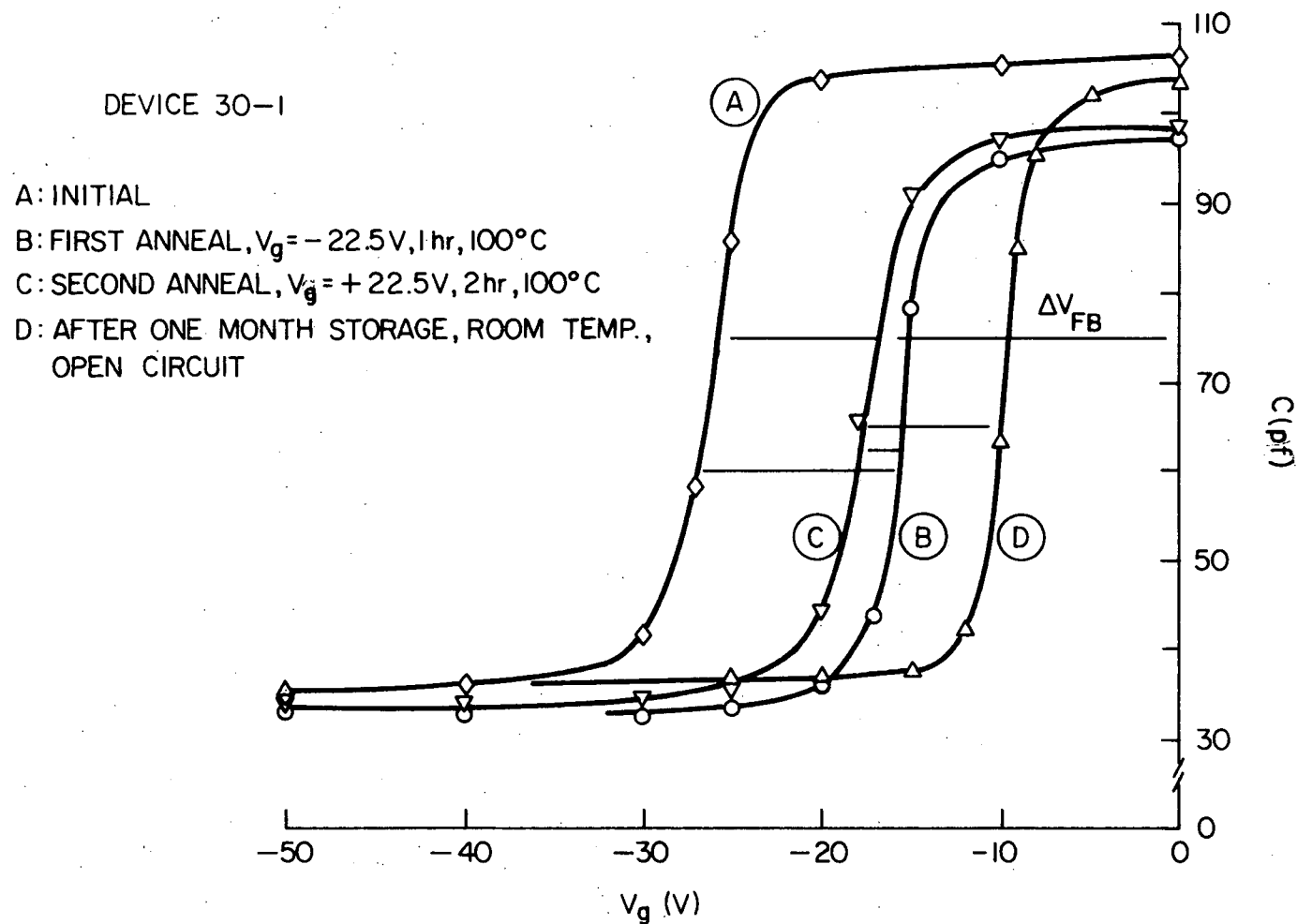
Figure 32. Capacitance vs. voltage of implanted MOS capacitor after bias-temperature stressing.

electrode was negative (accumulation). No changes in output were observed for nonilluminated cells (zero average current).

Investigation of Effects of Phosphorus Ion Implantation Into Oxide Antireflection Coating

In this section, a discussion is given of the implantation conditions and measurements made on the silicon solar cells received from JPL. The selection of the experimental conditions was consistent with the objective of the work which was to make a precursory examination of improving silicon solar cell response to blue light by implantation of charges in the oxide of standard cells. Additionally, selection was based on the amount of time allotted and also allowed expenditure. Although the latter limited the approach to be taken, the data accumulated does however, allow for interpretation and discussion. Annealing of samples could not be done because the cells used were previously contacted. Therefore, any damage in the oxide and the diffused layer could not be removed.

Calibration, Experimental Accuracy and Reproducibility

During the course of data accumulation, emphasis was placed primarily on reproducibility of measurements although the accuracy was of considerable concern. Constant energy from the B and L monochromator was obtained by leaving the entrance and exit slits set at 3.5 and 2.0 mm, respectively, for all wavelengths and adjusting the bulb temperature. This permitted spectral purity and resolution to more approximately remain a constant over all wavelength settings as opposed to the method of changing entrance slit settings.

Monochromator output was recorded and adjusted using an Eppley Laboratory thermopile, Serial No. 7017, calibrated with a standard lamp from the National Bureau of Standards. For the spectral measurements made on all cells, the incident flux was 18.53×10^{-6} watts/cm^2 at all wavelengths. The resolution of the monochromator was 12.8 mμ for the slit settings. The monochromator bulb temperature was set by tabulating its current as a function of wavelength. These data are shown in the first two columns of Table 3.

Reproducibility of this method is also shown in Table 3 where the potential drop across the series 56.2 ohm resistor is given. Measurements were made on one of the experimental cells with a 1/4" diameter mask on 4/15/71 and later on 5/26/71. The selection of the sample used was at random and data are shown for cell # 12. Data of this nature were taken on GaAs cells to set up this measurement apparatus prior to receiving the silicon cells used in this investigation. Similar reproducibility was obtained for GaAs cells.

For the I-V characteristics, an incident flux of 139.6 mW/cm^2 was established for test cells using the BFS 602 obtained from JPL. This cell had a 67.22 mV output at 28°C for the required incident flux level. The size of the standard did not permit using it with the test apparatus constructed prior to receiving it. Therefore, one of the 1" x 2" cells was provided with wire contacts and calibrated against the standard to serve as a secondary standard and located adjacent to the test cell in a holder provided for this purpose. All measurements were made against this standard. The flux level was determined by adjusting, each time a

81

TABLE 3. REPRODUCIBILITY OF SPECTRAL RESPONSE MEASUREMENTS

λ mμ	across 2 ohms V Lamp (volts)	V(56.2 ohms)mv 4/15/71	5/26/71
395	.8685	.0330	.0326
405	.8480	.0470	.0400
415	.827	.0480	.0480
425	.800	.0520	.0515
435	.783	.0590	.0592
445	.761	.0630	.0640
455	.752	.0720	.0739
465	.735	.0770	.0773
475	.719	.0835	.0835
485	.700	.0855	.0974
495	.690	.0958	.0945
505	.678	.100	.0980
515	.668	.106	.105
525	.653	.100	.102
535	.650	.110	.110
545	.644	.110	.112
555	.643	.115	.117
565	.642	.119	.120
575	.641	.122	.122
585	.640	.129	.128
595	.640	.137	.137
600	.638	.138	.139
610	.635	.146	.143
620	.629	.149	.148
625	.621	.140	.139
635	.620	.149	.148
645	.615	.151	.139
650	.610	.150	.150
655	.606	.149	.148
665	.600	.148	.144
675	.595	.146	.143
685	.591	.150	.150
700	.591	.160	.158
750	.576	.163	.161
800	.566	.164	.162

measurement was to be made, the lamp current to give 0.432 volts across a 7 ohm resistor in series with the secondary standard. No provision was made for temperature regulation. It was therefore, left to the experimenter to maintain as carefully as possible near room temperature conditions.

Experience showed that as much as 1.4% error in reproducibility of OCV could be obtained due to temperature changes of the cell under test. For this case, the cell was exposed to the incident flux for a period slightly exceeding any of the normal measurements, thus obtaining an upper limit in error for this data. Care in data accumulation however, was used and it is believed that reproducibility was better than 0.7% in the measurement of OCV.

Since the same arguments apply to the I-V Characteristics, these measurements could have a reproducibility error of the same amount.

Further, but perhaps critical for our work, the absolute values of OCV, I_{SCC}, and I-V characteristics could have a greater error owing to color temperature differences between Centralab and OSU light sources and relative spectral response differences between the tested cells and the calibrated BFS 602 standard cell.

Comparison of Production Solar Cell Characteristics Before
  Implantation Obtained by Centralab and OSU

The results of measured OCV, I_{SCC} and maximum power P_{max} on cells received from JPL are given in Table 4. Shown are results obtained on the 12 cells used to obtain implantation characteristics only. The remaining cells were used for other measurements and experimentation.

TABLE 4. OCV, I_{SCC} AND P_{max} ON PRODUCTION CELLS

Cell No.	Type	OSU			Centralab.	
		OCV in volts	I_{SCC} in ma	P_{max} in mw	OCV in volts	I_{SCC} in ma
6	1 x 2	--	--	--	--	--
7	1 x 2	--	--	--	--	--
8	1 x 2					
9	1 x 2					
10	Secondary Standard	.563	71.3	26.4	Average .585	Average 76
11	Secondary Standard					
12	Secondary Standard					
1	1 x 1	.560	27.7	10.81		30.1
2	1 x 1	.561	28.9	11.69		31.7
3	1 x 1	.563	28.6	11.87		31.2
4	1 x 1	.558	29.2	11.82		31.5
5	1 x 1	.555	29.7	11.84		32.2
6	1 x 1	.556	27.9	11.5		30.4

Our measurements show consistently lower values of OCV and I_{SCC}. As mentioned earlier in the discussion of measurement error, we made no attempt to control the temperature of cells. Emphasis was placed on reproducibility. On the other hand, the color temperature of the lamp used could well have been different from that used by Centralab and the relative spectral response of the BFS 602 and the production cells may have been different. Therefore, even though the flux level set on the basis of the calibrated BFS 602 standard cell was maintained constant; the possible differences in color temperature and relative spectral response may explain the lower values of OCV and I_{SCC} obtained in these measurements.

Measurements were not obtained on all cells for the full cell response since implantation could only be made on a 1/4" diameter region in the bombardment apparatus. Only data before and after implantation over this 1/4" diameter region was considered significant. These results will be shown later, taken before and after implantation on the same region of the cell.

Implantation Conditions and Techniques

Following initial measurements of OCV, I_{SCC} and maximum power (on some of the cells) they were mounted in the implant unit for bombardment at three voltages, 20, 30, and 40 KeV and different total dose of 10^{12}, 10^{13}, 10^{14} and 10^{16} phosphorus ions. Since the cells had a layer of oxide approximately 700 Å thick, the voltages were selected such that the peak of the range distribution was within the oxide layer. This amounted to 250, 370, and 490 Å for the respective energies. The full width at half maximum for these energies were 215, 300 and 385 Å, respectively. These combine to give a maximum range at the distribution half width of 357, 520 and 682 Å, respectively. Therefore, it was expected that little

C2

damage to the silicon would occur providing the oxide layer was free of defects and of uniform thickness. It was observed however, that the oxide layers had pin holes and were also slightly nonuniform in thickness.

Implant dose is determined by taking the beam current-time product. Deposited positive ion phosphorus concentration is approximated by taking the dose area density and dividing by R_{hm}.

Open Circuit Voltage and Short Circuit Current
Before and After Implants

Data giving the OCV and I_{SCC} obtained on all test cells before and after implant is presented in Table 5 for the different bombardment conditions. For ease of reading these have been ordered by increasing voltage and implant dose. These data were taken with the 1/4" diameter mask in place. Recall that reproducibility error in OCV is approximately 0.7% or approximately .004 volts. For the lower implant conditions, the recorded data for some of the cells show an increase well within this limit so an improvement in OCV cannot be inferred. In general, all cells show a decrease in these values as a result of implant.

The change in I_{SCC} resulting from implantation also shows a decrease for all bombardment conditions. The values of I_{SCC} were obtained by extrapolating measured current in decreasing values of series resistance to a zero series resistance value. As expected due to unwanted series resistance in the measurement circuit obtained values at the lower loads of 1 and 2 ohms were in error. Figures 33, 34(a) and 34(b) show the plotted data before and after implantation from which I_{SCC} values were obtained.

TABLE 5. OCV, I_{SCC} AND CELL POWER THROUGH 1/4" DIAMETER MASK.

| Cell No.	Type	Implant V(KeV)	Implant N_S Ions	OCV (Volts) Before	OCV (Volts) After	ΔV	I_{SCC} (ma) Before	I_{SCC} (ma) After	ΔI	Power (mW) Before	Power (mW) After
7	1x2	20	1×10^{12}	.503	.505	+.002	12.12	12.04	-.08	--	--
6	1x1	20	1.41×10^{13}	.530	.530	.∅	10.91	10.50	-.41	4.00	4.00
6	1x2	20	1.0×10^{12}	.501	.501	-.006	11.96	12.36	+.40	--	--
8	1x2	20	1.92×10^{15}	.503	.493	-.010	11.87	9.46	-2.41	--	--
12	1x2	30	1.25×10^{12}	.510	.508	-.002	12.35	11.97	- .38	--	--
5	1x1	30	9.4×10^{12}	.530	.531	+.001	11.40	10.89	- .51	4.05	4.05
11	1x2	30	9.4×10^{13}	.508	.508	∅	12.38	11.68	- .7	--	--
9	1x2	30	7.8×10^{15}	.504	.490	-.014	12.16	6.06	-6.1	--	--
3	1x1	40	1.0×10^{12}	.533	.533	∅	11.13	10.10	-1.03	4.14	3.82
2	1x1	40	9.4×10^{12}	.531	.531	∅	10.87	10.73	- .14	3.87	3.87
4	1x1	40	9.4×10^{13}	.531	.533	+.002	11.34	10.66	- .68	4.18	4.18
1	1x1	40	9×10^{15}	.532	.463	-.069	11.17	6.18	-4.99	3.61	1.91

87
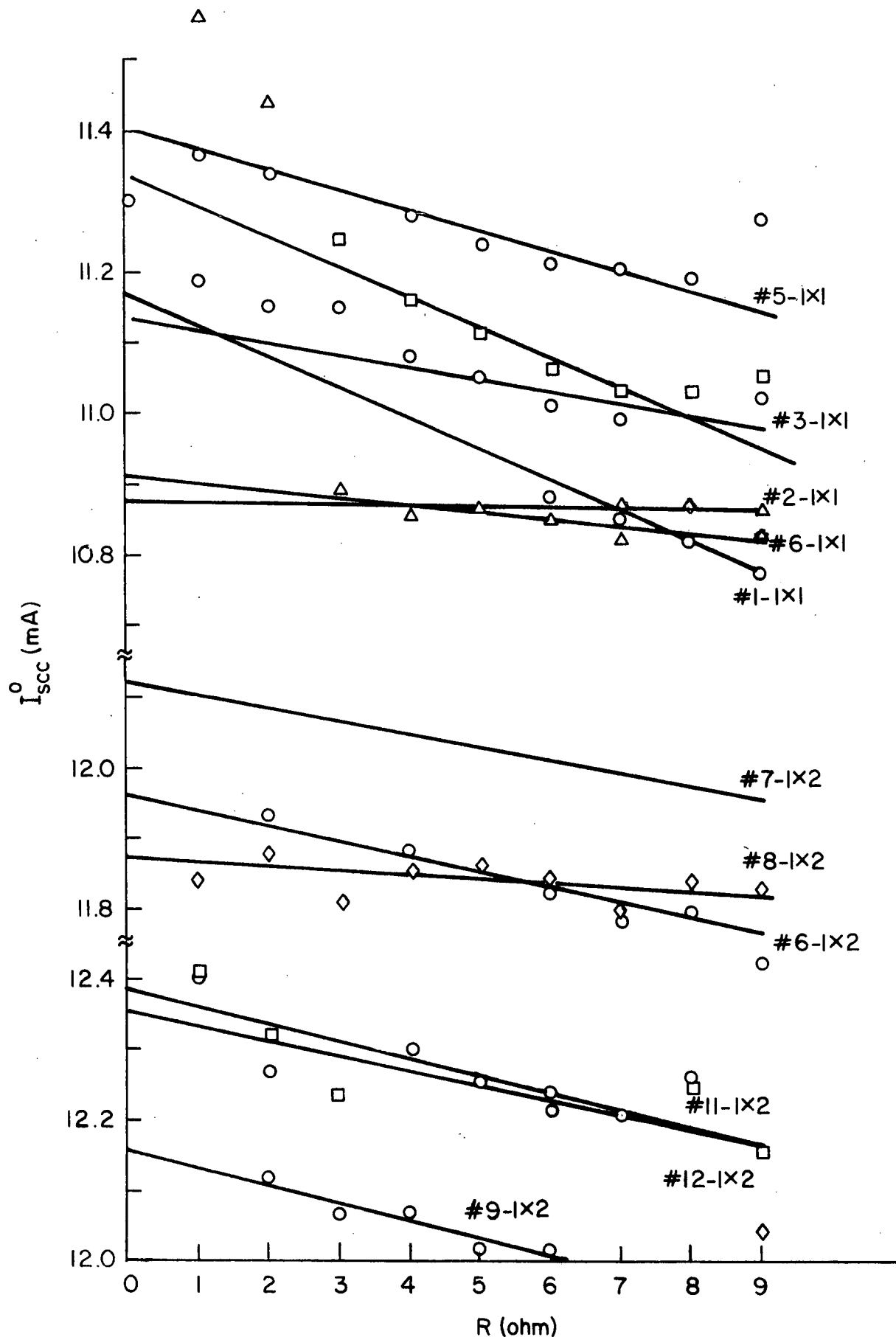
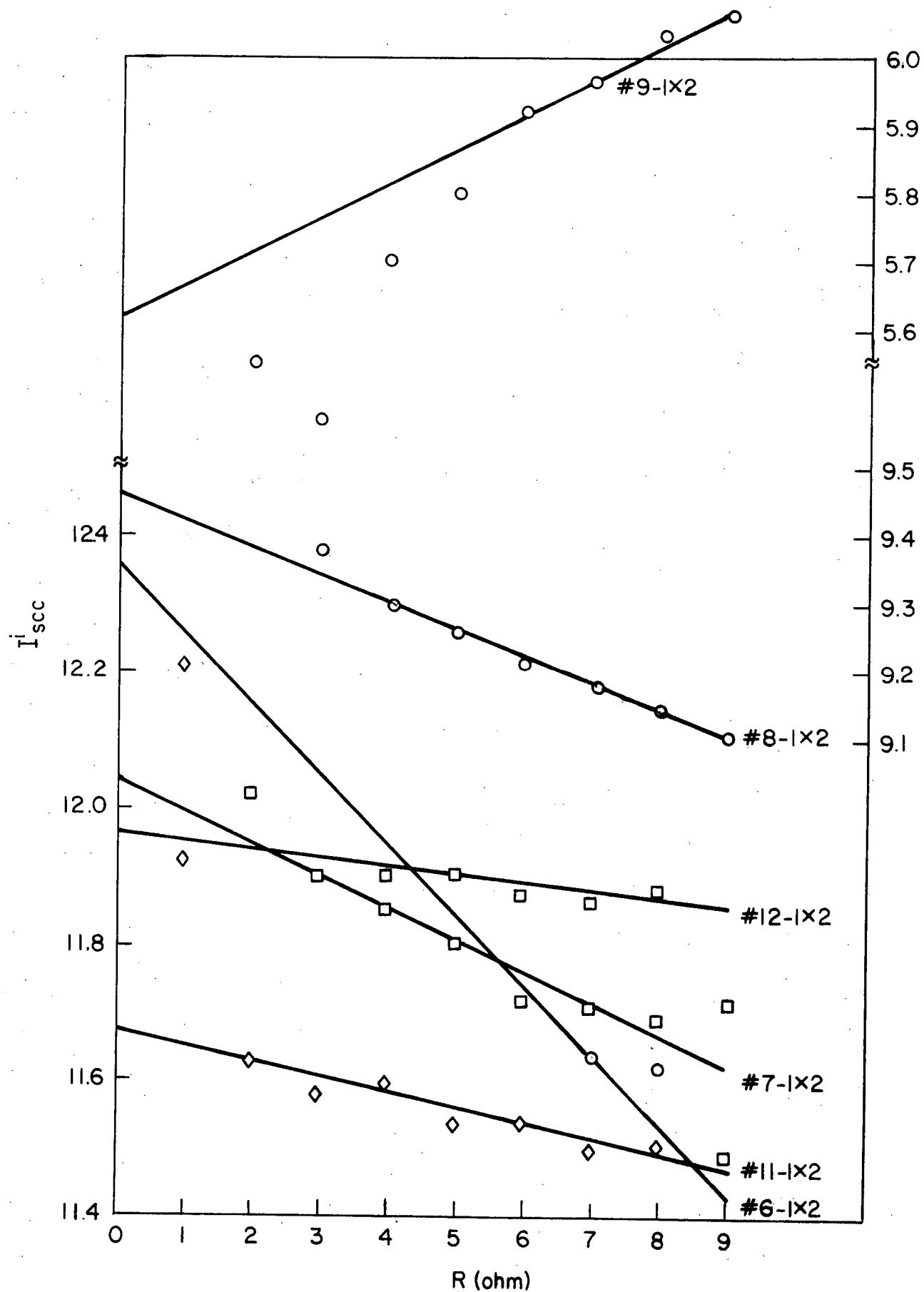Figure 33. Short circuit current before implantation vs. series resistance.

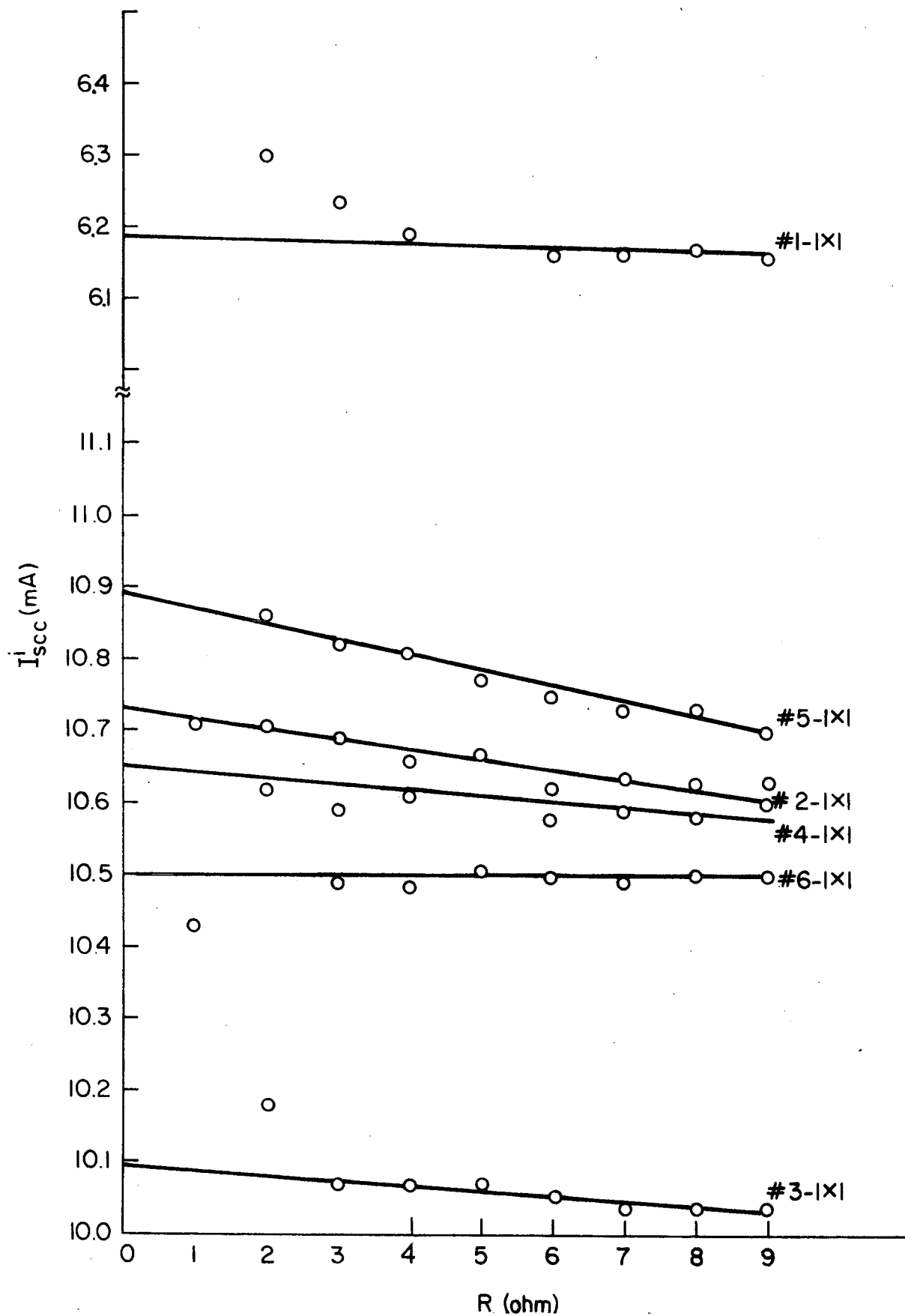Figure 34(a). Short circuit current after implant vs. series resistance.

Figure 34(b).   Short circuit current after implant vs. series resistance.

These correspond well with values obtained on I-V curve plots on the X-Y recorder. However, the latter were less accurate.

There is evidence of large error in determining I_{SCC} after implantation for cells 6 (1 x 2) and 9 (1 x 2) in Figure 34(a). Apparently, sufficient cell damage occurred in Cell 9 to account for this behavior. Cell #6 gives results which are not consistent with other measurements and therefore should be neglected from consideration with regard to this measurement. No cause for these anomalous results could be found.

A plot of $(\Delta I/I_o)$ x 100 vs. implant dose is given in Figure 35 neglecting Cell #6 (1 x 2).

Considerable scatter is observed below 10^{14} ions. Above 10^{14} however, the current after implant I^i_{SCC} can be written as,

$$I^i_{SCC} = I^o_{SCC} \, (1 - aN_s^{1/2}) \tag{19}$$

and is apparently independent of the implant energy. Since N_s, is very approximately proportional to ρ_s, the implant density in the oxide as determined by N_s and the R_{hm} for different energies, then Equation (20) can be written as

$$I^i_{SCC} = I^o_{SCC} \, (1 - b \, \rho^{1/2}) \tag{20}$$

Energy dependence would appear in the determination of the average value of ρ through the R_{hm} values. Since this does not vary greatly in comparison with the accuracy of determining N_s, the plotted data is not expected to show energy dependent behavior.
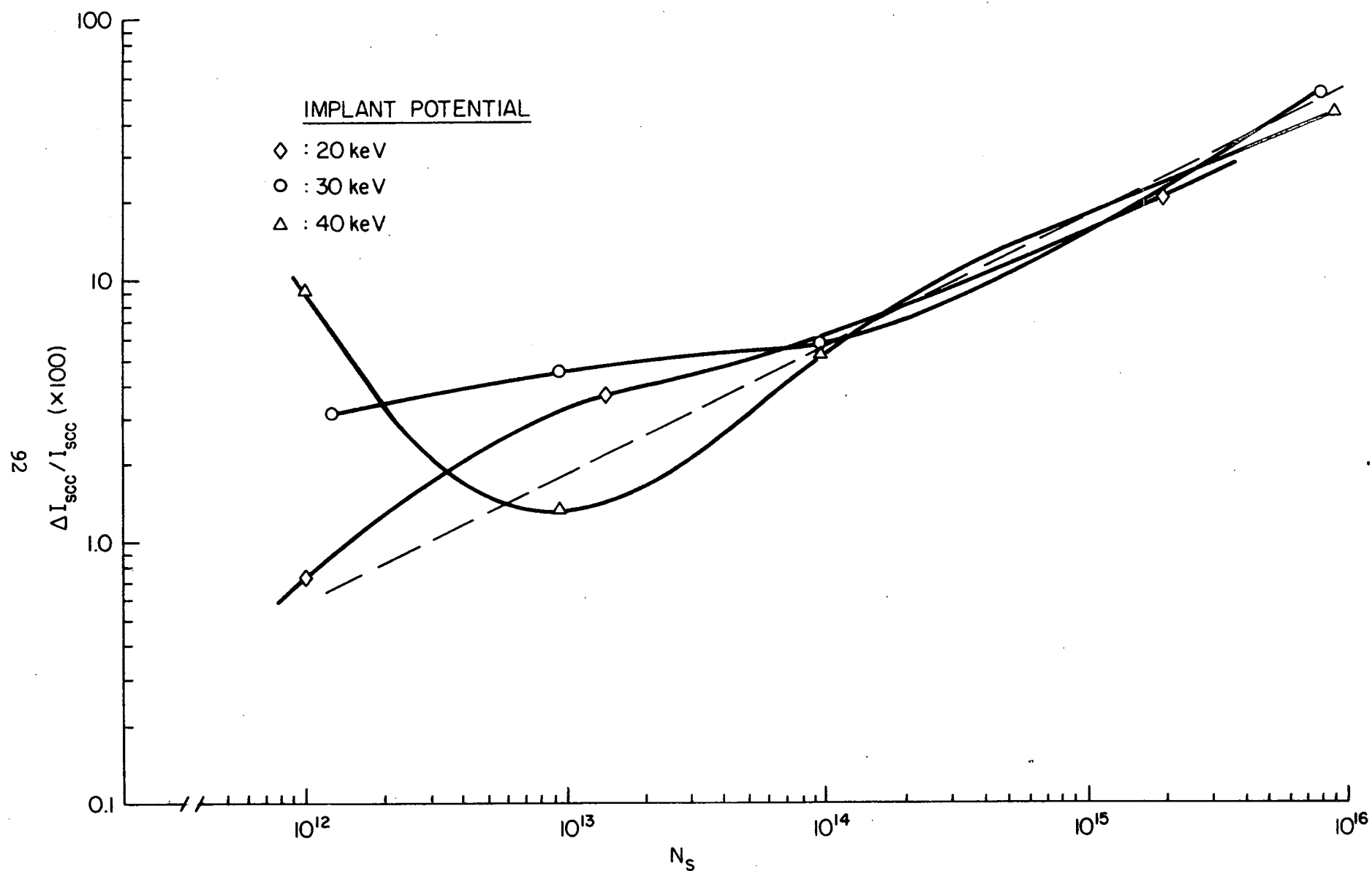
Figure 35. The ratio of the difference in I_{SCC} before and after implantation to I_{SCC} before vs. implant dosage for integrated spectral response.

To be noted is the scatter in data below 10^{14}. This is in the region of small changes in I_{SCC}. Therefore, the error in ΔI is larger and as mentioned is on the order of 1 percent in reproduction. The limited data of one information point per implant conditions is insufficient to determine a mathematical model or to conclude that ΔI is always a negative value.

The density of charge deposited in the oxide as determined by taking N_S and dividing by the implantation area of 0.316 cm^2 and the distribution FWHM as shown in Table 6.

The upper limit implantation was set by the implant density being very nearly equal to the atom density of solids. The lower limit was established by the minimum value that could be reproducibility set with the available implant apparatus. It would have been desirable to extend the lower limit by two orders of magnitude to better approximate the surface state density at the oxide-silicon interface.

Under all conditions of implant the surface of the cell where the beam impinged became visibly different than before implant. The difference increased with increased implant dose and ranged from being just distinguishable to a mirror-like finish which looked much like the surface of polished silicon. More will be said on these differences later when discussing the Cary 14-reflection data.

I-V Characteristics Before and After Implant

I-V characteristics obtained on cells 1-6 (1cm x 1 cm) are shown in Appendix A. These curves obtained with the X-Y plotter served

93

TABLE 6. DENSITY OF POSITIVE PHOSPHORUS IONS IN OXIDE

V (KeV)	N_S	10^{12}	10^{13}	10^{14}	10^{16}
			ρ in N_D/cm^3		
20		1.45×10^{18}	1.45×10^{19}	1.45×10^{20}	1.45×10^{22}
30		1.05×10^{18}	1.05×10^{19}	1.05×10^{20}	1.05×10^{22}
40		0.81×10^{18}	0.81×10^{14}	0.81×10^{20}	0.81×10^{22}

primarily to obtain cell power data as shown previously in Table 5, since accuracy for determining I_{SCC} and OCV using this technique was poorer than for the previously described method. Both full cell and 1/4" diameter masked cell data are presented in Appendix A before and after implant.

Spectral Response Characteristics Before and After Implant

Measurements of spectral response of the 1/4" diameter masked cells were made over the region 3950 Å to 8000 Å and are shown in Appendix B for all the cells tested. Typical of the response is the curve shown in Figure 36. The curve after implant was found to be always below or equivalent to the response before implant. The peak in the curves at about 5200 Å was common among the cells initially. The curve between 4000 Å and 6000 Å became increasingly straighter as N_S is increased to the point of knee inversion observed for the highest implant level as may be seen for Cell #8 in Appendix B.

Also characteristic of these curves are the bumps. These were not present when GaAs solar cells were evaluated during setting up of the equipment. Possible explanation of these are: (1) Possible change in lamp position prior to testing of the silicon cells since other investigators were using the monochromator. These uses preceded the silicon investigation and no perturbations occurred afterwards. (2) Possibly the 1/4" diameter mask which was made from photographic print paper wrapping had a spectral characteristic. The black side of the paper was in contact with the cells. (3) There could be characteristic 1/4" wavelength coupling from the oxide layer. Since the oxide refractive index is $\sqrt{\varepsilon_r}$ where ε_r is nearly equal
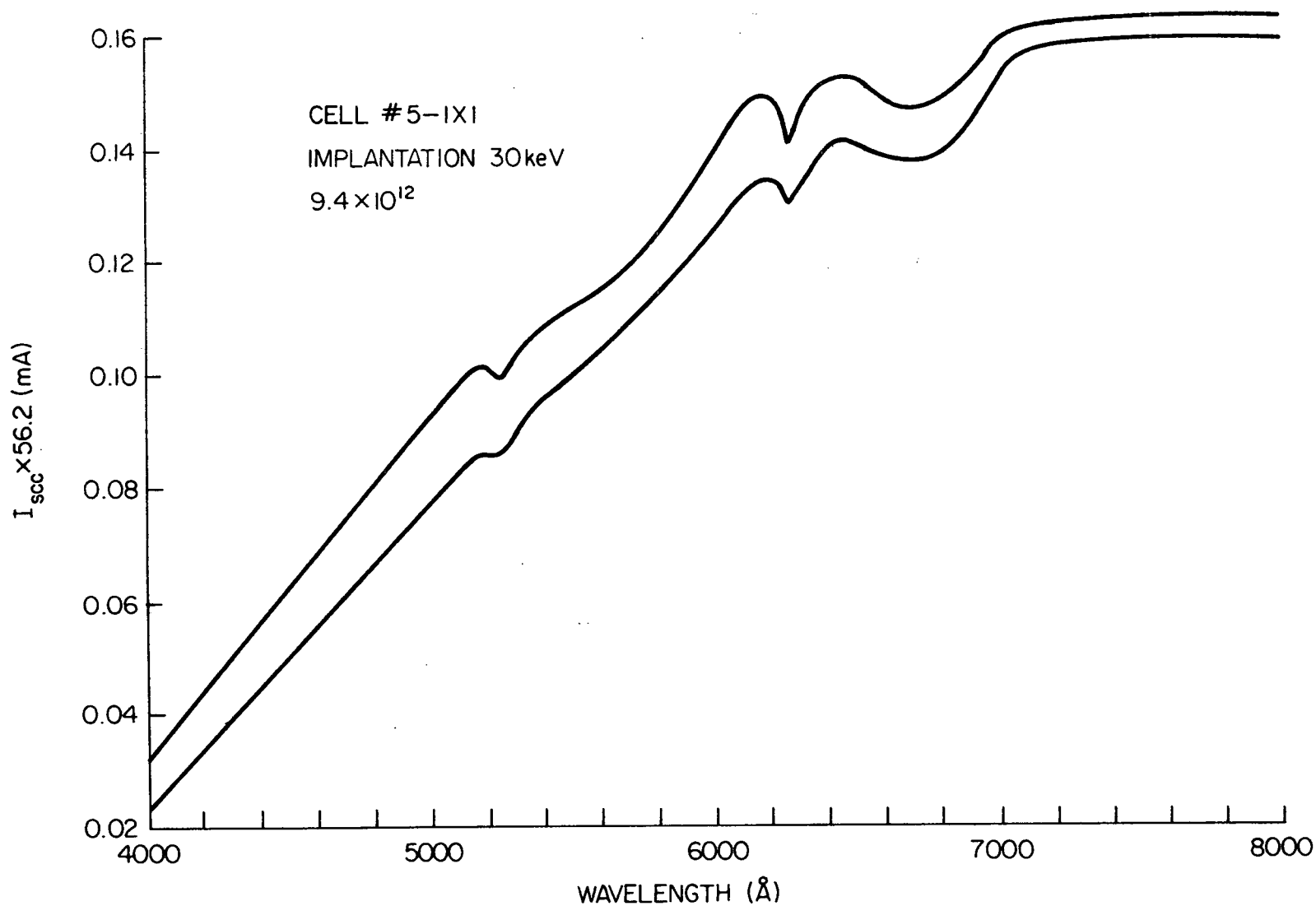
Figure 36. Typical spectral response characteristics for 1/4"
diameter masked cell before and after implantation.

to 3.4, then wavelength in air, characteristic of 700 Å of oxide is $\lambda =$ 4 x 700 Å x $\sqrt{3.4}$ = 5200 Å. This corresponds to the lowest peak position of all curves.

In regard to the objective of this work; however, these peaks can be ignored since changes are of importance only. In general, the greatest change is observed in the position of the original knee between 5000 Å and 5400 Å. A lesser decrease is observed at near 4000 Å and even a lesser decrease at 8000 Å. For most of the lower density implantations, there is no decrease in the spectral response above 6800 Å.

Since the blue region response is of interest the percent change in the relative spectral response curves at 3950 and 4800 Å are shown in Figure 37 and 38. From Figure 6, shown earlier, these two wavelengths are in the front layer (n-layer) response region of the cells. Within experimental error of single data points the percentage decrease in cell response is very nearly the same. Also, any dependence on implant energy is not evident. Further, the very approximately same dependence on N_s is observed as found for I_{SCC} data presented earlier in Figure 35.

The above observations show that blue response is decreased due to implantation of phosphorus ions. This could be due to (1) n-layer damage predominantly, (2) spectral shifting of the oxide layer, (3) charge effect on interface states is in the wrong direction for the highly doped layer of silicon.

Cell Reflectivity Before and After Implant

In order to partially understand the observed behavior, the cells were examined for changes in reflectivity. The Cary 14 strip chart
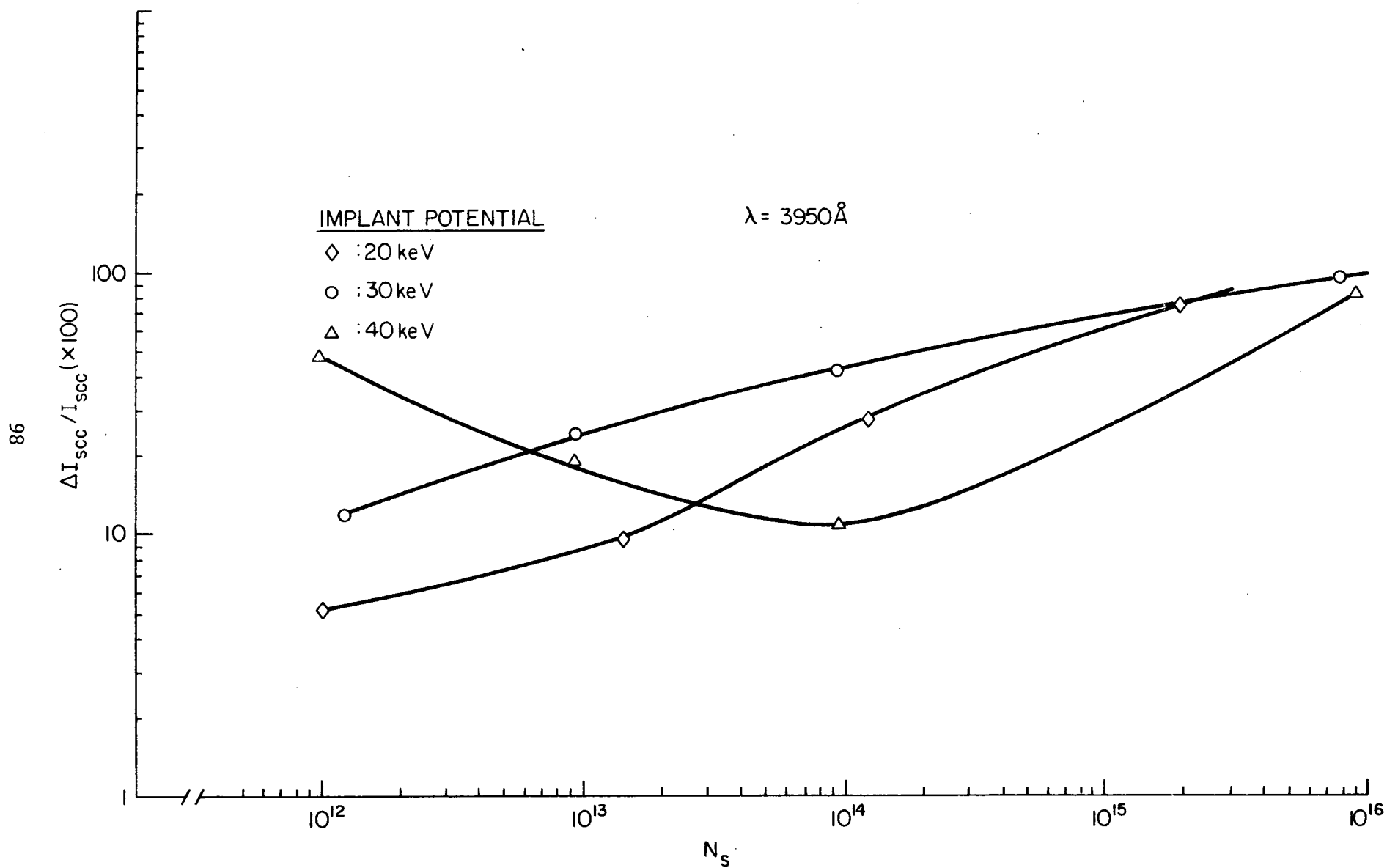
97

Figure 37. The ratio of the difference in I_{SCC} before and after implantation to I_{SCC} before implantation vs. implant dosage at 3950 Å.
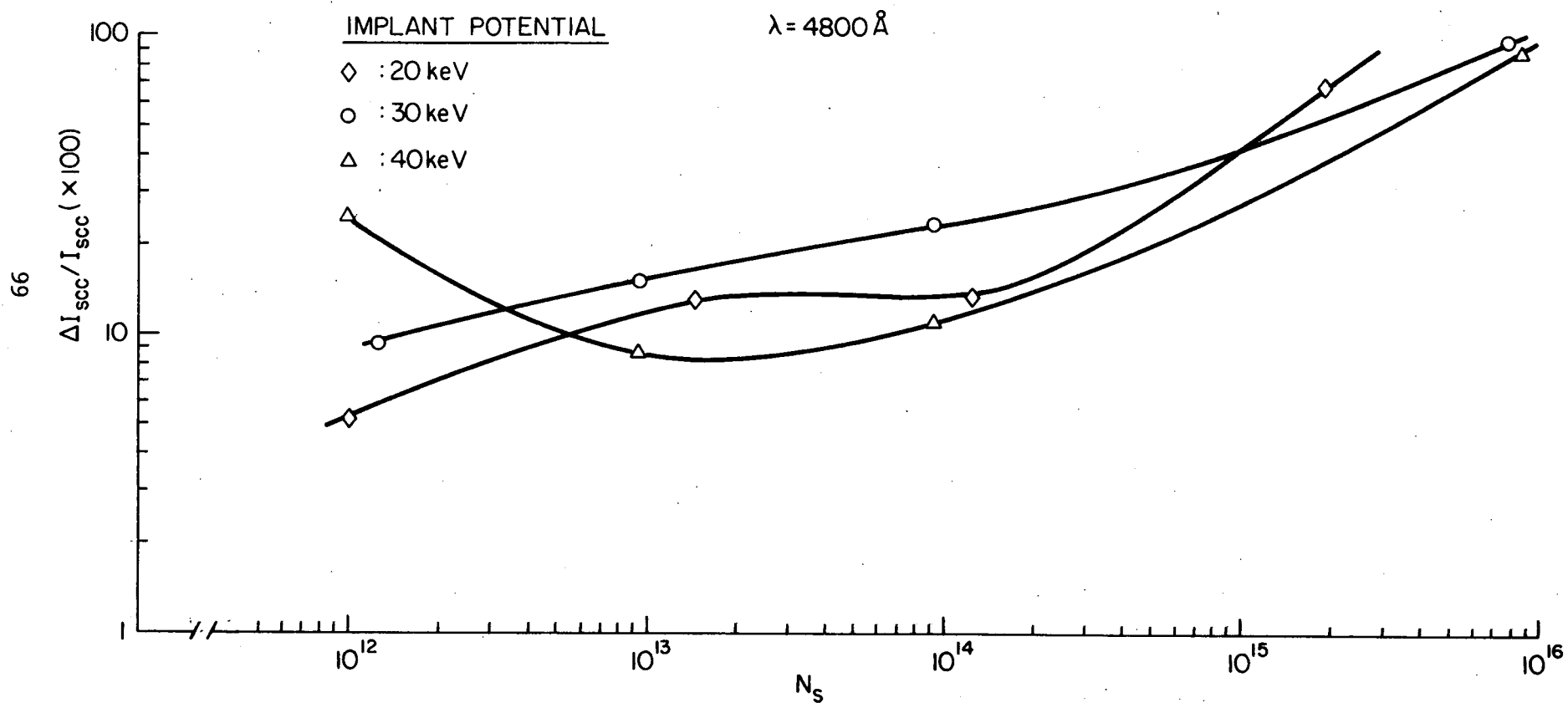
Figure 38. The ratio of the difference in I_{SCC} before and after implantation to I_{SCC} before implantation vs. implant dosage at 4800 Å.

recorder was set up to measure on the log response slide wire resistor. A decrease in light output in the sample side was noted as an increase in recorder response; i.e., the recorder measured absorbance A, as

$$A = \log \frac{1}{I_r} + C$$

where I_r is the cell reflected intensity and since air was used as reference, C is some arbitrary constant. Measurements were made for A_o on a nonimplanted region of the cell over the wavelength region 3000 Å to 6500 Å giving

$$A_o = \log \frac{1}{I_r^o} + C$$

The implanted region was then positioned in the beam and measured for A_i giving

$$A_i = \log \frac{1}{I_r^i} + C$$

The difference $A_o - A_i$ gives then the change in absorbance as

$$A_o - A_i = \log \frac{I_r^i}{I_r^o}$$

Plots of $A_o - A_i$ for the 30 keV and 40 keV implants are shown in Figures 39 and 40, respectively. These data, in general, show that the cells reflect less light at the shortest and longest wavelengths and a decreased reflectance near 6000 Å over a varying region. One exception occurs for cell # 9 in Figure 39 and # 1 in Figure 40. Since an increase in the wavelength response previously discussed is always decreased, the light not reflected after implant must somehow be lost by a mechanism other than the one which increases cell performance. At the shorter
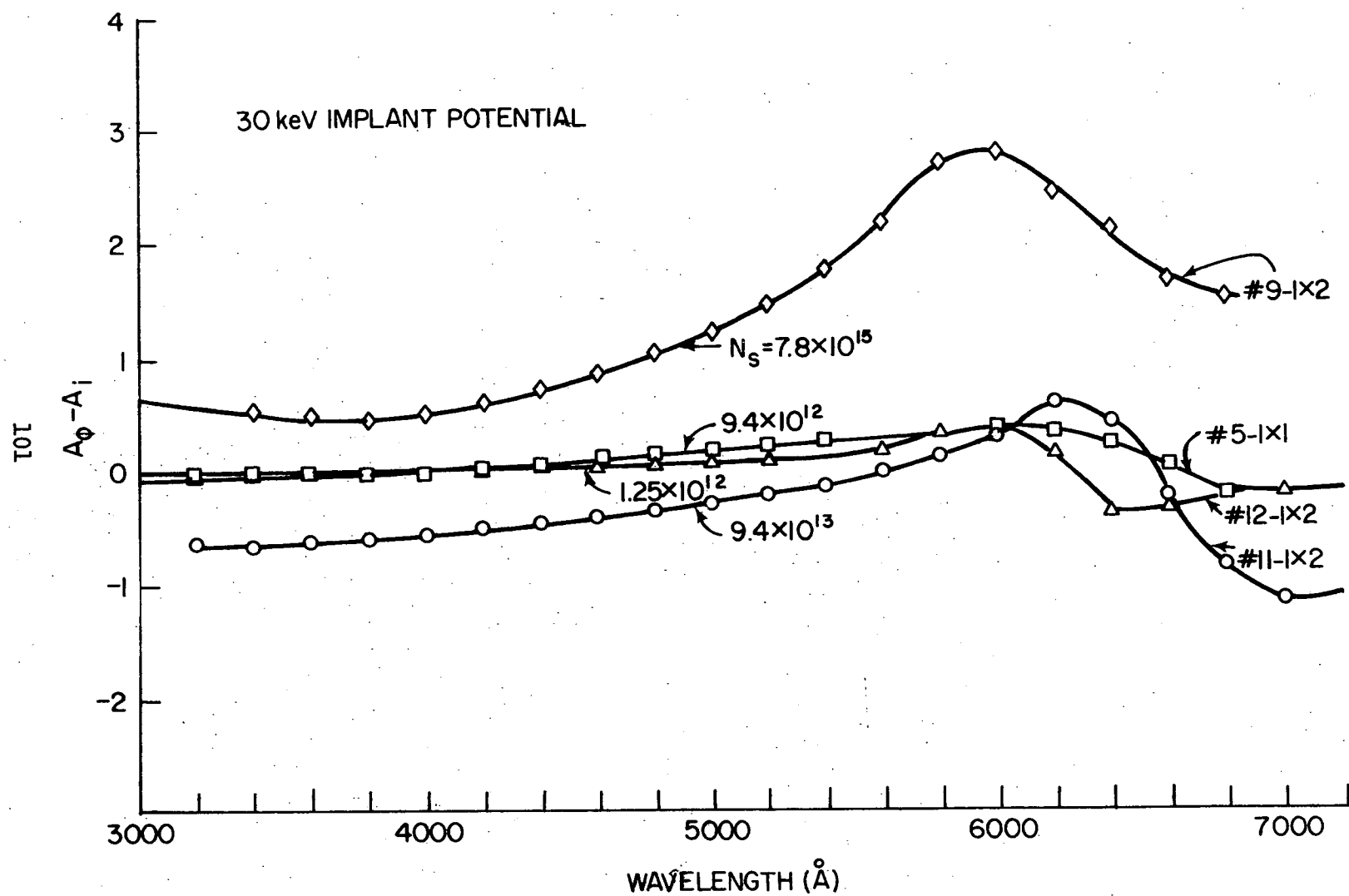
Figure 39. The difference in light absorption of oxide layer before and after implantation as a function of wavelength.
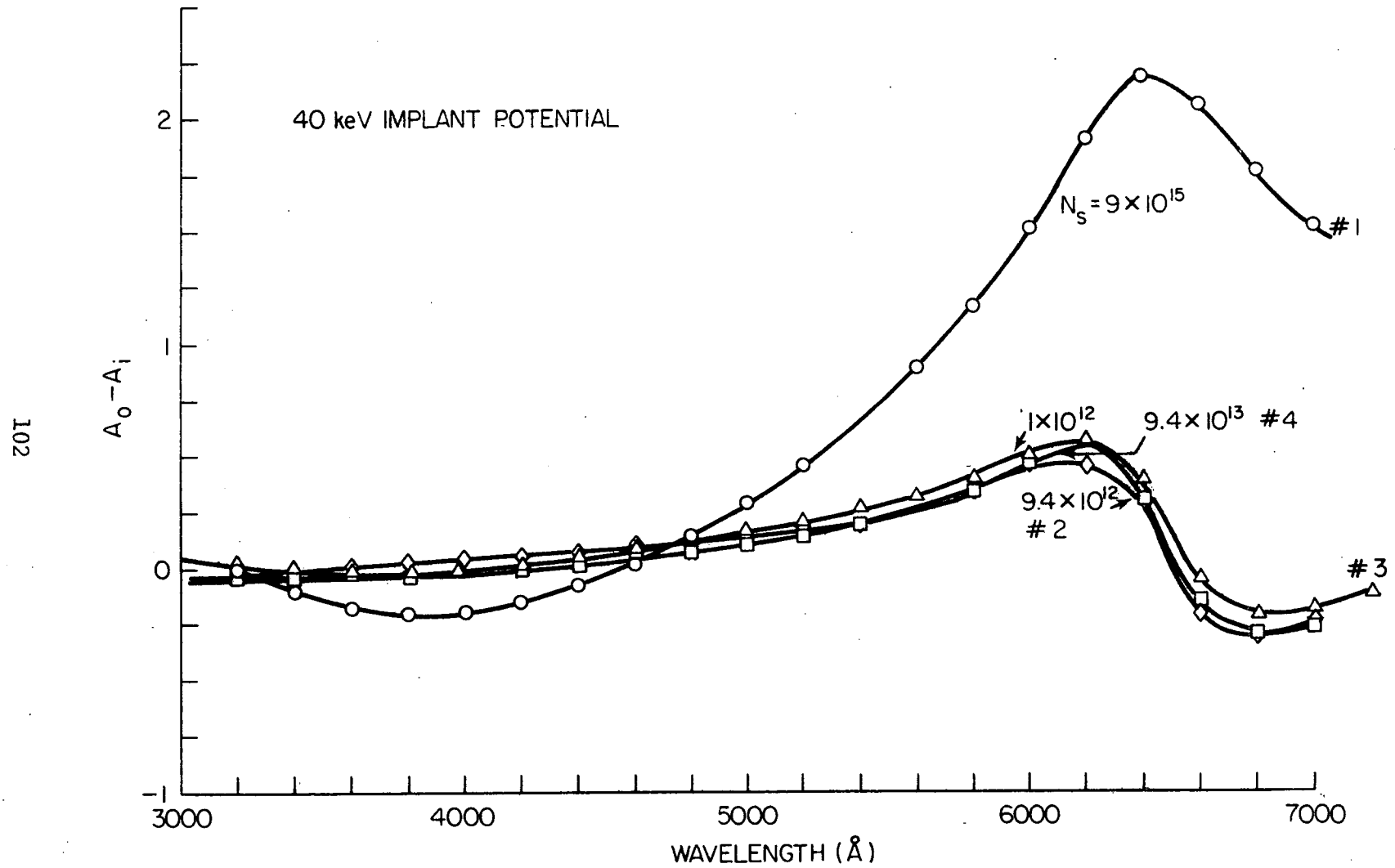
Figure 40. The difference in light absorption of oxide layer before and after implantation as a function of wavelength.

wavelength, it is expected that defects produced by the bombarding energetic ions provide scattering centers which remove photons from the beam thereby decreasing the reflected light intensity which would appear as increased absorption. This need not be totally responsible for cell spectral response degradation since it is possible for deeper penetrating ions causing damage in the silicon. As mentioned before pinholes and nonuniform oxide thickness would allow damage to the silicon to occur.

At the long wavelength where scattering would be minimized and where increased abosrption is observed, which could be due to a change in oxide thickness and dielectric constant, the beneficial effects are perhaps cancelled by the cell surface damage.

DISCUSSION

The primary objective in this research has been to reduce solar cell losses due to surface recombination of excess minority carriers. In silicon cells, the theoretical analyses to date usually consider $0 < s < 1000$ cm/sec as the range of recombination velocities for calculations of the surface region short-circuit current (or efficiency in the Ellis and Moss article). In attempting to match experimental p/n Si solar cell spectral collection efficiencies with theoretical calculations Wolf[6] found it necessary to employ $s = 10^4$ cm/sec either with or without a drift field in the surface region ($x_J = 0.5$ μm). He also states that surface recombination velocities below 10^4 cm/sec do not affect the diffused region collection efficiency with drift fields of 4700 volt/cm, and that $s = 10^4$ cm/sec has little effect on collection efficiency for the field free case.

Thus, the importance of surface recombination in Si solar cells cannot be stated specifically until the actual recombination velocities have been determined. In his gate-controlled surface recombination velocity diodes Rosier[23] observed maximum values for s on 0.8 ohm-cm n-type Si of 3×10^3 to $> 10^4$ cm/sec. In these thermal SiO_2-Si interfaces there are no measurable surface states in the range from 0.15 to 0.55 eV below the conduction band, and there is a significant density of donor states in the 0.15-0.45 eV range above the valence band ($5 \times 10^{12} - 5 \times 10^{13}$ states/cm^2 - eV). The former result is contrary to the results

of Figure 13 in which a large acceptor state concentration is observed ≃ 0.15 eV below the conduction band. Again it is emphasized that the above results refer only to presumably clean thermally-grown oxides on Si.

Since surface recombination is related directly to the fast surface state density, and those surface states closest to the intrinsic Fermi level have the greatest effect on recombination (both in the bulk and at the surface), there are two apparent approaches to reducing surface recombination. In the research reported here the goal has been to introduce excess positive charge into the bulk of the oxide for the purpose of bending the energy bands at the surface and increasing the surface potential (accumulation of electrons at the surface of the n-type diffused layer). As pointed out previously in the theoretical discussion, the anticipated degeneracy of the diffused layer near the surface requires modification or greater development of the theory of recombination.

The second approach to the reduction of recombination involves the overall reduction of the surface state density. According to the Goetzberger hypothesis[24] this requires the elimination of surface charges in the oxide at the SiO_2-Si interface. First, the source of these charges is probably the result of several effects: Excess ionic Si in thermal oxides, ionizing radiation, etc. High temperature annealing in appropriate atmospheres tends to reduce the surface charge in clean thermal oxides[46]. However, surface states are not completely eliminated. Typical surface densities of 10^{12} cm^{-2} imply one surface state in an area 100 Å square.

The effective range of the coulombic field of the surface charge inducing the surface state is on the order of 30 $\overset{\circ}{A}$. This distance is therefore the approximate thickness of the surface charge layer.

Perhaps further consideration and development of this surface charge/surface state theory will indicate the possible reduction of a particular group of surface states (acceptor or donor) by charge compensation. These charges would be introduced in the critical 30 Å oxide layer, by chemical or vapor deposition, or ion implantation, before the remainder of the oxide is deposited.

CONCLUSIONS

Briefly, these investigations have yielded inconclusive results concerning the possibility of improving Si solar efficiency by charge introduction in the oxide antireflection coating. It is concluded however, that phosphorus ion implantation does not meet the requirements for successfully monitoring the charge at the SiO-Si interface.

In this study, the data obtained indicate that as the implantation dosage and energy of phosphorus ions is increased, the cell efficiency in the blue response region decreases.

These results, although apparently negative from the standpoint of the thesis that charge implanted in the oxide should be able to increase cell efficiency to higher values in the blue response region, are considered incomplete and inconclusive.

The incompleteness of this investigation stems from the expectation that negative charge placed at the interface could be expected to decrease Q_{ss} and thus decrease N_{st} while positive charge should increase Q_{ss} and N_{st}. Phosphorus ions implanted in SiO give positive charge thus increasing Q_{ss} and also increasing N_{st}. Ion implantation does not readily lend itself to introducing negative charges. Consequently, to investigate this case, another technique of introducing negative charge at the oxide-Si interface may be needed. There is some evidence available in Chou and Crowder's work[47] on O^+ and Ne^+ implants that negative complex ions were possibly achieved at the SiO-Si interface by ion implantation. It is recommended that further research be conducted on charge effects in the oxide

antireflection coating on blue response since if the above thesis is correct, it would be expected that N_{st} and therefore surface recombination velocity would decrease if negative ions were introduced at the SiO-Si interface.

In addition to the thesis that the sign of charge introduced in this experimental investigation was the wrong polarity for increasing blue region efficiency of solar energy conversion, two other experimental observations in the research lead to the conclusion that the data on implanted charge effects gathered here are somewhat inconclusive.

1. The oxide antireflection coatings of the production cells investigated had pinholes and nonuniform thicknesses. Therefore, although the average oxide thickness was greater than the depth of ion implantation for all the implantation voltages investigated, the thinner regions and particularly the pinholes allowed the impinging ions to be implanted in the Si surface beneath the oxide. Thus, some degree of n-layer Si damage was incurred. Since the cell construction would not allow post-annealing, to remove damage, it was not possible to eliminate such damage that occurred. Radiation damaged Si is known to cause reduction in solar cell efficiency.

2. Ion implantation produced physical changes in the oxide layer. Thickness was increased with increase in implantation dose. The blue color was changed by degrees to the color of the Si surface as dosage was increased to 10^{16}.

In general, the reflectance of cells became less at the shortest and longest wavelengths suggesting more blue light will penetrate to the Si and implying that the observed decrease in cell efficiency is perhaps greater than the experimental results reveal because of the greater number of photons which reach the Si interface.

In order to avoid both the pinhole and nonuniform thickness difficulties characterizing deposited SiO encountered in implantation which can result in surface damage of the Si thermally oxidized Si would be desirable since such oxide has pinholes and nonuniformities. However, the temperatures involved in such processing may be prohibitive for maintaining the impurity distribution desired in a solar cell.

Furthermore, in view of the physical changes which ion implantation introduces in the oxide layer which tend to mask the effects of the charge implanted in the oxide layer on the efficiency of the solar cell, it also appears that ion implantation is not satisfactory for introducing charge.

It follows that a more controllable and positive approach to introducing charge in the oxide layer of the SiO-Si interface is needed which will allow both negative and positive charge introduction and maintenance of oxide physical characteristics.

The apparent negative result obtained in the transparent electrode-insulator-solar cell structure investigation does not preclude that charge at the interface can not affect blue response of Si solar cells. In the transparent field electrode structure, only the interface

109

surface potential is influenced, not the number of charges, Q_{SS} at the interface. On the basis, that Q_{SS} controls N_{st}, a direct interface coupling of the existing Q_{SS} with negative charge in order to lower Q_{SS} is required if N_{st} is to be changed.

RECOMMENDATIONS

This preliminary investigation has essentially demonstrated that ion implantation does not fit the requirements for monitoring charge at the interface of the SiO-Si in Si solar cells. If some means of annealing the cells after implantation were provided, however, the interpretation of the present results could be more completely carried out and the usefulness of ion implantation for charge introduction would be improved.

However, the thesis that monitoring charge at the SiO-Si interface of a solar cell is a reasonable approach to improving blue response of Si solar cells has not been proven or disproven.

Therefore, it is recommended that investigations be conducted on introducing both positive and negative charge concentration at the SiO-Si interface at the start of deposition of the oxide in order to further evaluate the possible benefits of interface charge monitoring on the blue response of Si solar cells. Also, attempts to form negative complex ions by O^+ and Ne^+ charge implantation should be conducted.

The former perhaps could be done by spraying negative and/or positive charges on the Si surface at the start of SiO deposition by evaporation. Another possible way may be by using other insulators than SiO which can produce negative interface charge at the Si surface rather than positive charges.

Since part of the cause of the inconclusive results in this study was the inability to anneal out Si and SiO damage after implantation, it is also recommended that the present studies be continued and

expanded by using nonelectroded solar cell structures to which an annealing step can be applied after implantation followed by oxide masking, etching the oxide and electroding to achieve a completed solar cell.

Further, in view of the in-depth theoretical analysis conducted during this program and presented herein, the following investigations are recommended.

1. Theoretical studies using computer calculations aimed at accounting for degeneracy in the surface region of the Si and the presence of various types of impurity profiles should be conducted.

2. Si solar cells should be made using epitaxial processing and epitaxial doping to vary both the surface concentration of impurity and impurity profile in the surface region from the conditions characterizing diffusion profiles to nondegenerate surface concentration and greater than exponential impurity gradients in the surface region. This experimental effort would not only strike at the problems facing further optimization of the Si solar cell, but also provide experimental data useful in the theoretical study recommended in (1).

It is recommended that the above types of investigation be considered as a follow-on to the present effort.

NEW TECHNOLOGY

No reportable items of new technology resulted from this brief experimental study.

ACKNOWLEDGEMENT

The advice, encouragement, and direct participation of Professor W. W. Anderson in many aspects of these efforts were greatly appreciated.

BIBLIOGRPAHY

1) J. J. Wysocki and P. Rappaport, "Effect of Temperature on Photovoltaic Solar Energy Conversion", J. Appl. Phys., 31, 571 (1960).

2) J. Mandelkorn, et.al., "Fabrication and Characteristics of Phosphorous-Diffused Silicon Solar Cells", J. Electrochem. Soc., 109, 313 (1962).

3) H. J. Queisser, Solid-State Electronics, 5, 1 (1962).

4) M. Wolf, "Advances in Silicon Solar Cell Development", Energy Conversion for Space Power, Academic Press, Inc., New York, 1961, pp. 231-261.

5) B. Dale and F. P. Smith, "Spectral Response of Solar Cells", J. Appl. Phys., 32, 1377 (1961).

6) M. Wolf, "Drift Fields in Photovoltaic Solar Energy Converter Cells", Proc. IEEE, 51, 674 (1963).

7) S. Kaye and G. P. Rolik, IEEE Trans. Elect. Dev., ED-13, 463 (1966).

8) W. M. Bullis and W. R. Runyan, IEEE Trans. Elect. Dev., ED-14, 75 (1967).

9) W. R. Runyan and E. G. Alexander, "An Experimental Study of Drift-Field Silicon Solar Cells", IEEE Trans. Elect. Dev., ED-14, 3 (1967).

10) R. Van Overstraeten and W. Nuyts, IEEE Trans. Elect. Dev., ED-16, 632 (1969).

11) B. Ellis and T. S. Moss, "Calculated Efficiencies of Practical GaAs and Si Solar Cells Including the Effect of Built-In Electric Fields", Solid-State Electronics, 13, 1 (1970).

12) A. S. Grove, Physics and Technology of Semiconductor Devices, John Wiley and Sons, Inc., New York (1967).

12a) R. Sahai and A. G. Milnes, "Heterojunction Solar Cell Calculations", Solid State Electronics, 13, 1289 (1970).

13) V. I. Fistul, Heavily Doped Semiconductors, Plenum Press, New York (1969).

14) V. M. Molovetskaya, et.al., "The Reflection Coefficient of Anti-reflection Coated Surfaces of Silicon Photo Cells", Soviet Phys. Solid State, 1, 1099 (1960).

15) D. B. York, J. Electrochem. Soc., 110, 271 (1963).

16) Iles and Leibenhaut, Solid-State Electronics, 5, 331 (1962).

17) E. Tannenbaum, Solid-State Electronics, 2, 123 (1961).

18) D. D. Kleppinger and F. A. Lindholm, "Impurity Concentration Dependent Density of States at the Fermi Level for Silicon", Scientific Report No. 6, Univeristy of Florida, Electrical Engineering Department, Gainesville, Florida, p. 45 (10 Oct. 1970).

19) W. Shockley and W. T. Read, Phys. Rev., 87, 835 (1952).

20) W. H. Brattain and J. Bardeen, Bell System Tech. J., 32, 1 (1953).

21) Many, Goldstein and Grover, Semiconductor Surfaces, American Elsevier Pub. Co., New York (1971).

22) B. H. Schultz, Physica, 20, 1031 (1954).

23) L. L. Rosier, IEEE Trans. Electr. Dev., ED-13, 260 (1966).

24) Goetzberger, Heine and Nicollian, "Surface States in Silicon from Charges in the Oxide Coating", Appl. Phys. Letters, 12, 95 (1968).

25) Swystun and Tickle, "Instability in Vacuum Deposited Silicon Oxide", IEEE Trans. Elect. Dev., ED-14, 760 (1967).

26) R. H. Kingston (ed.), Semiconductor Surface Physics, Univ. of Penn. Press, Philadelphia, p. 70 and p. 85 (1957).

27) Henisch, Reynolds and Tipple, Physica, 20, 1033 (1954).

28) Thomas and Rediker, Phys. Rev., 101, 984 (1956).

29) G. C. Dousmanis, Phys. Rev., 112, 369 (1958).

30) Alexandrakis and Dousmanis, J. Appl. Phys., 34, 3077 (1963).

31) Raymond Wolfe (ed.), Applied Solid State Science, Vol. 1, Academic Press, New York, p. 154 (1969).

32) D. R. Frankl, J. Appl. Phys., 38, 1996 (1967).

33) O. V. Snitko, Soviet Phys. Solid State, 1, 898 (1959).

34) Seiwatz and Green, J. Appl. Phys., 29, 1034 (1958).

35) Mayer, Eriksson and Davies, Ion Implantation in Semiconductors, Academic Press, New York (1970).

36) J. T. Burril, et.al., "Ion Implantation as a Production Technique", IEEE Trans. Elect. Dev. ED-14, 10 (1967).

37) R. W. Bower, et.al., "MOS Field Effect Transistors Formed by Gate Masked Ion Implantation", IEEE Trans. Elect. Dev., ED-15, 757 (1968).

38) R. S. Nelson and D. J. Mazey, Can. J. Physics, 46, 689 (1968).

39) McGill, Kurtin and Shifrin, J. Appl. Phys., 41, 246 (1970).

40) Southern, Willis and Robinson, "Sputtering Experiments with 1- to 5-KeV Ar$^+$ Ions", J. Appl. Phys., 34, 153 (1963).

41) Whan and Arnold, Appl. Phys. Letters, 17, 378 (1970).

42) V. F. Gianola, J. Appl. Phys., 28, 868 (1957).

43) Snow, Grove, and Fitzgerald, Proc. IEEE, 55, 1168 (1967).

44) Anderson and Mitchell, Appl. Phys. Letters, 2, 334 (1968).

45) A. Goetzberger, "Ideal MOS Curves for Silicon", Bell System Tech. J., 45, 1097 (1966).

46) S. R. Hofstein, "Stabilization of MOS Devices", Solid-State Electronics, 10, 657 (1967).

47) N. J. Chou and B. L. Crowder, "Effects of Ion Implantation", JAP, 41 1731 (1970).

48) M. Wolf, "A New Look at Silicon Solar Cell Performance", Energy Conversion, 11, 63 (June, 1971).

APPENDIX A

X-Y PLOTS OF I-V CHARACTERISTICS BEFORE AND AFTER IMPLANT
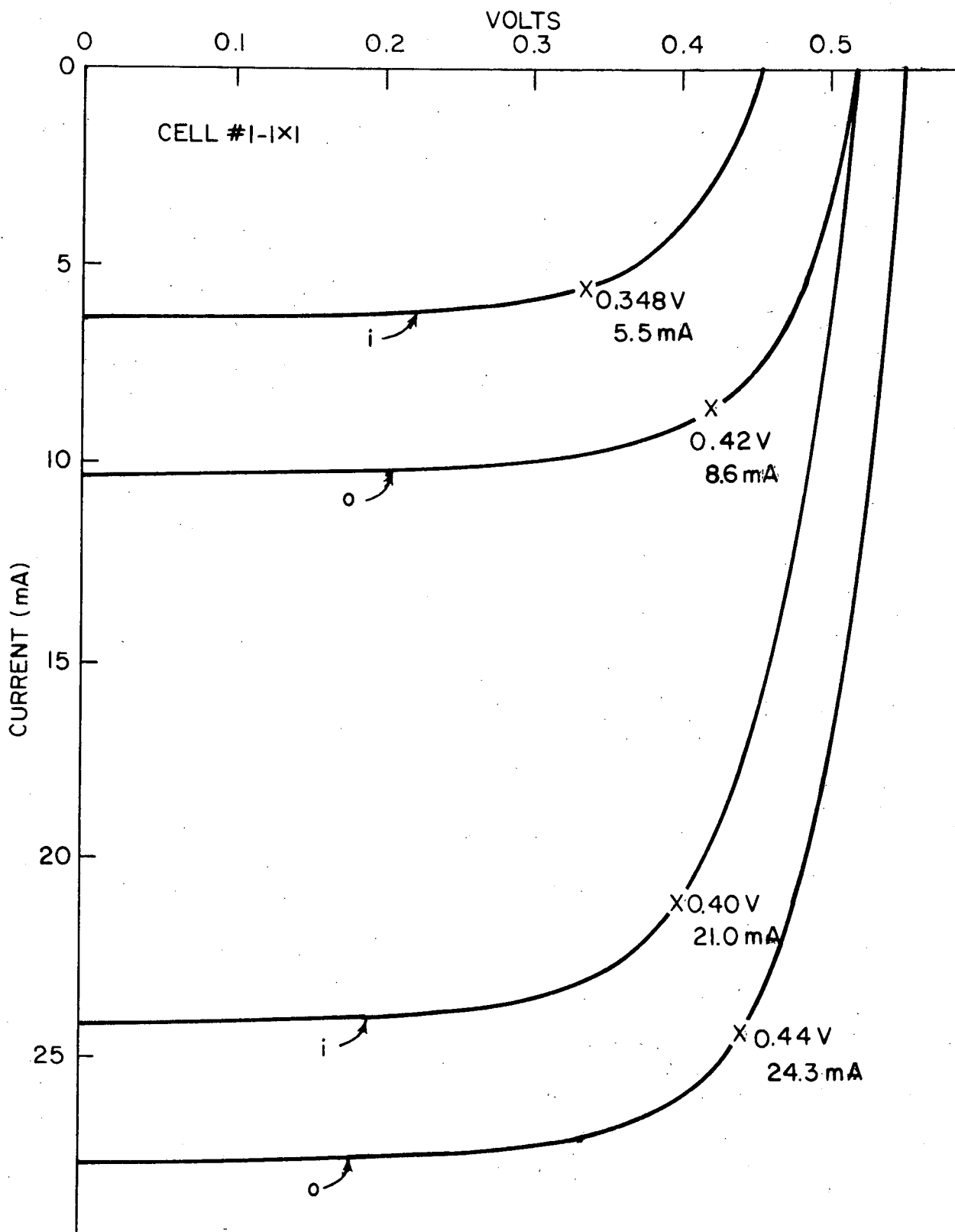
Figure A-1. I-V characteristics for full cell and 1/4"
diameter mask before and after implantation.

119
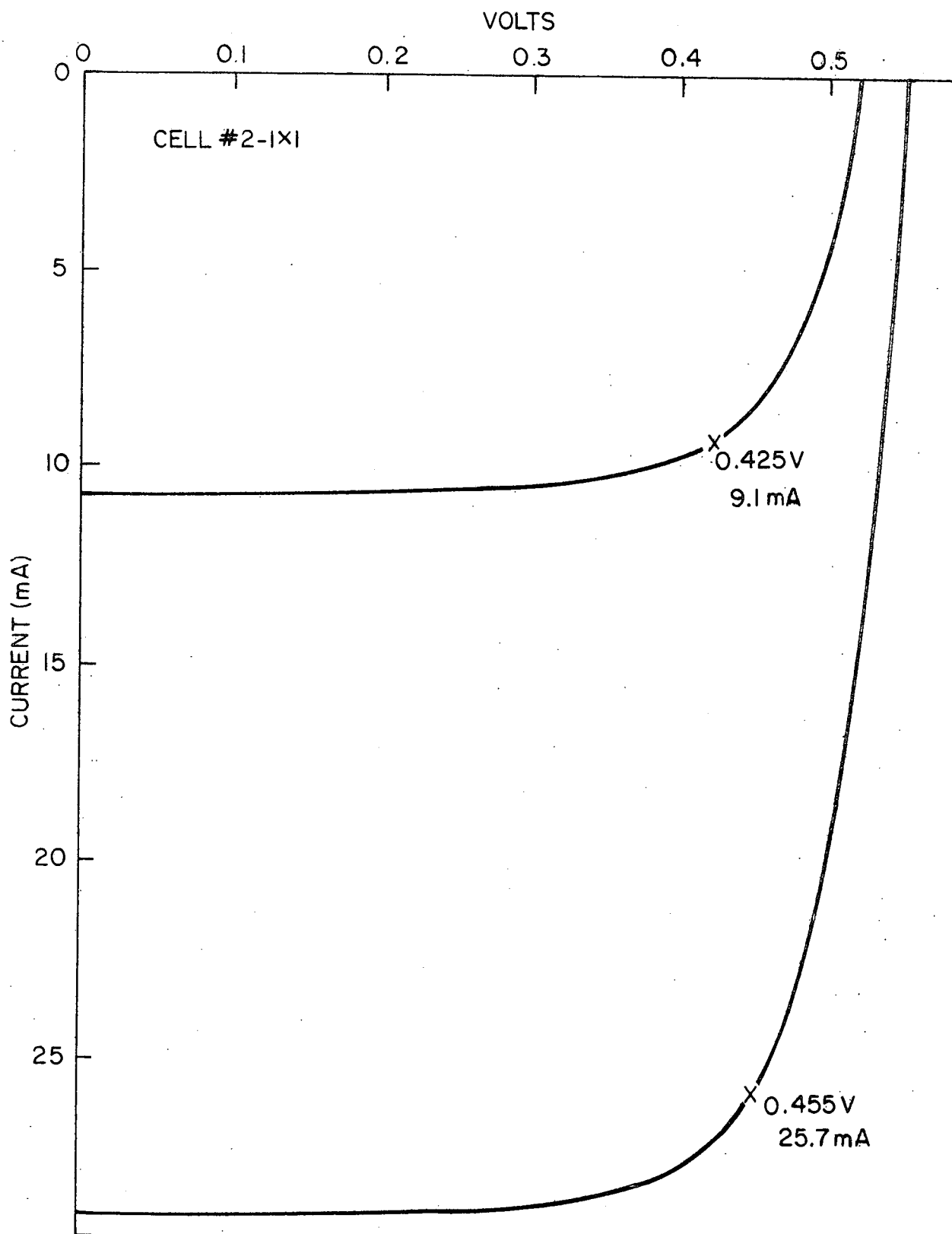
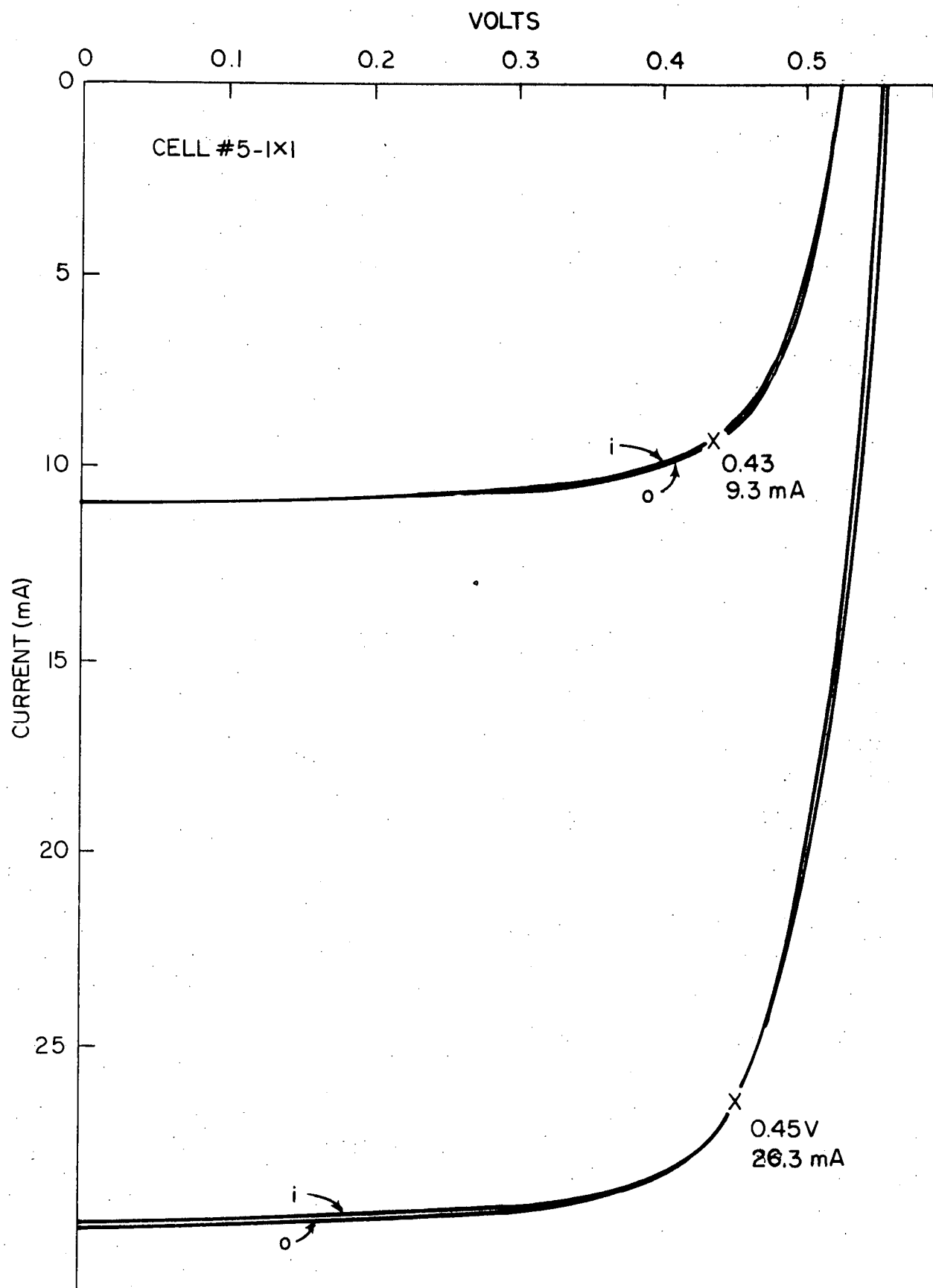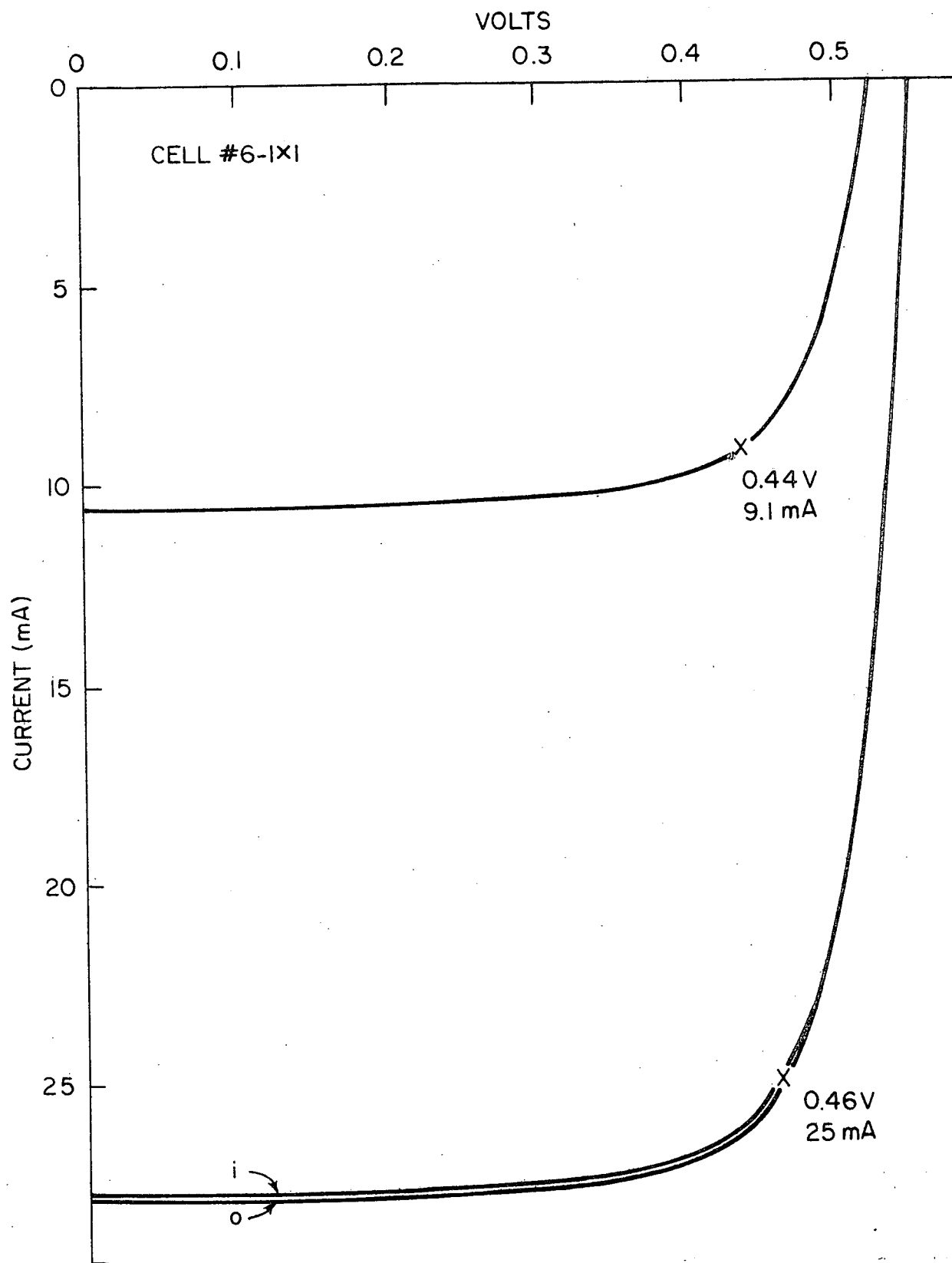Figure A-2. I-V characteristics for full cell and 1/4" diameter mask before and after implantation.

VOLTS

CELL #3-1×1

0.42V
9.1 mA

0.44V
9.4 mA

i

o

0.455V
24.9 mA

0.46V
25.8 mA

i

o

CURRENT (mA)
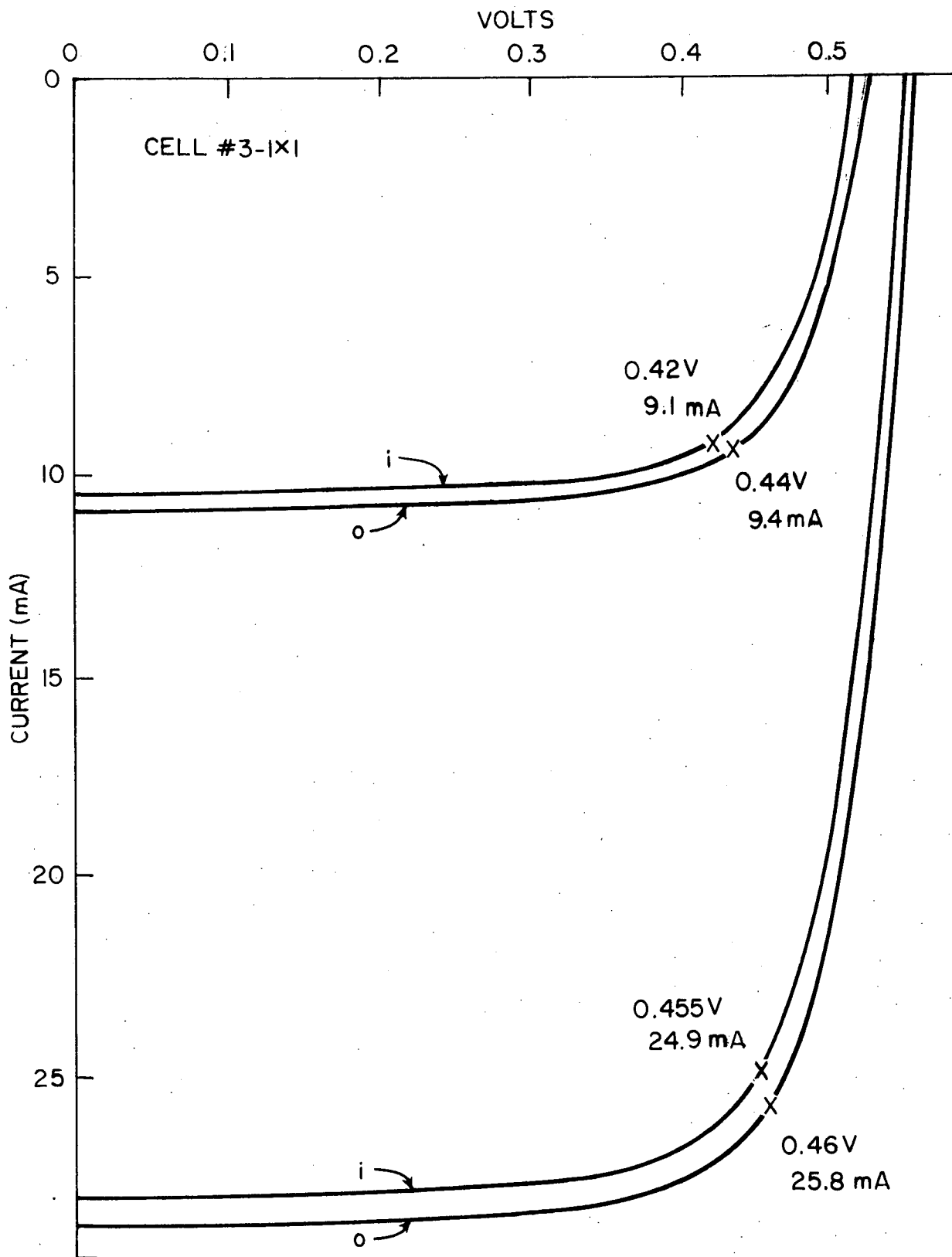
Figure A-3.   I-V characteristics for full cell and 1/4"
diameter mask before and after implantation.

121
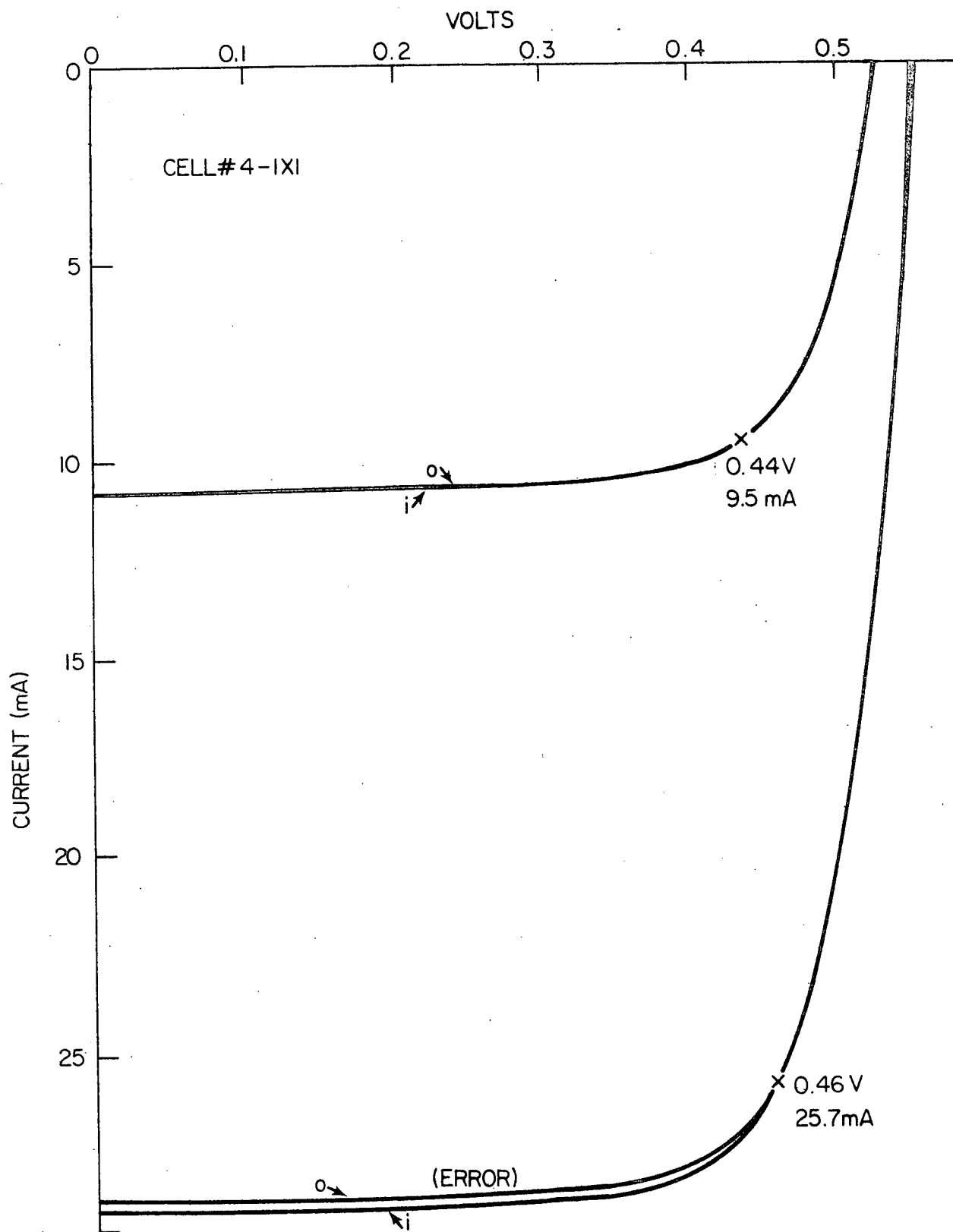
Figure A-4. I-V characteristics for full cell and 1/4"
diameter mask before and after implantation.

122

Figure A-5. I-V characteristics for full cell and 1/4" diameter mask before and after implantation.

Figure A-6. I-V characteristics for full cell and 1/4"
diameter mask before and after implantation.

APPENIDX B

SPECTRAL RESPONSE CHARACTERISTICS BEFORE AND AFTER IMPLANT
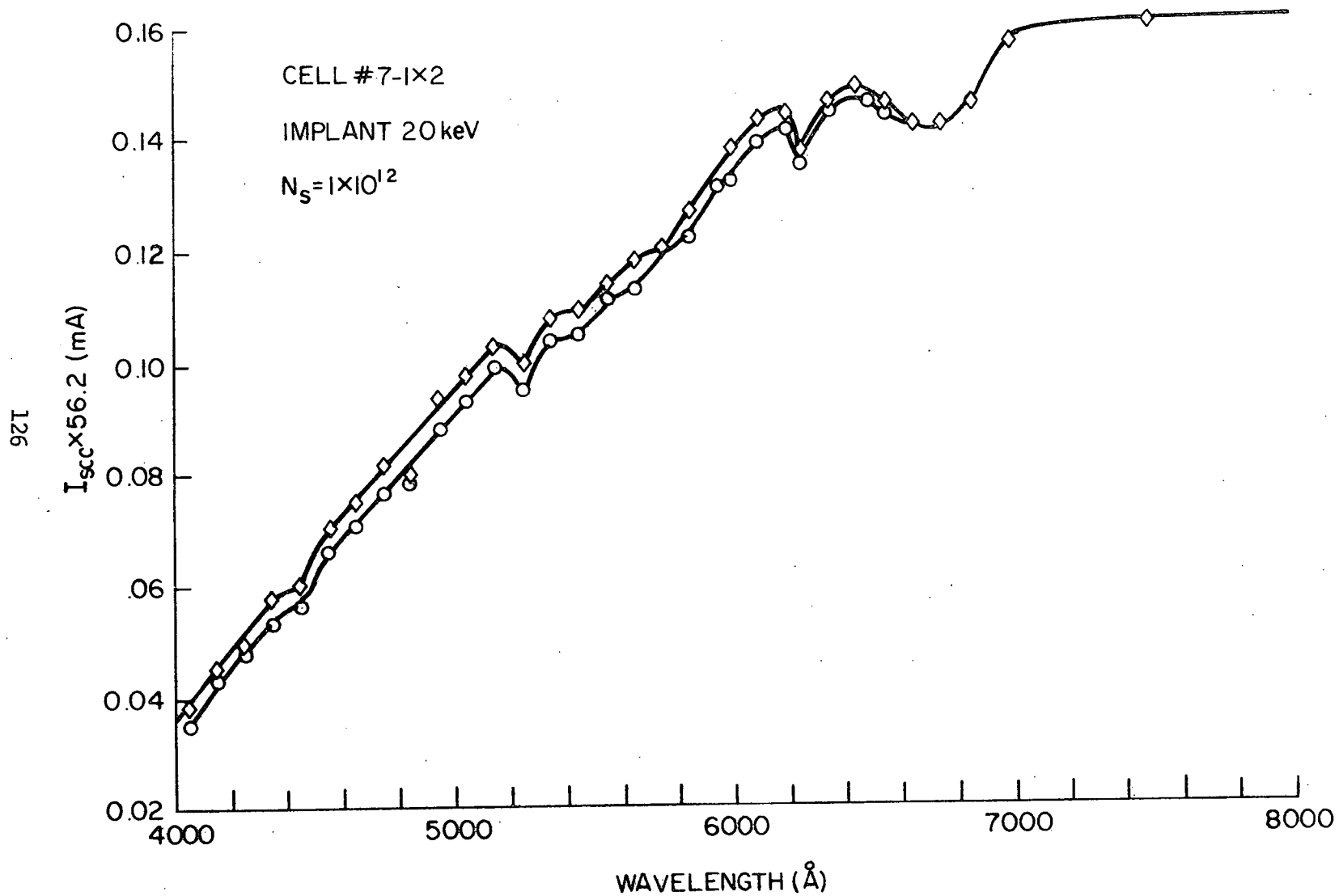
Figure B-1. Spectral response characteristics for 1/4"
diameter masked cell before and after
implantation.
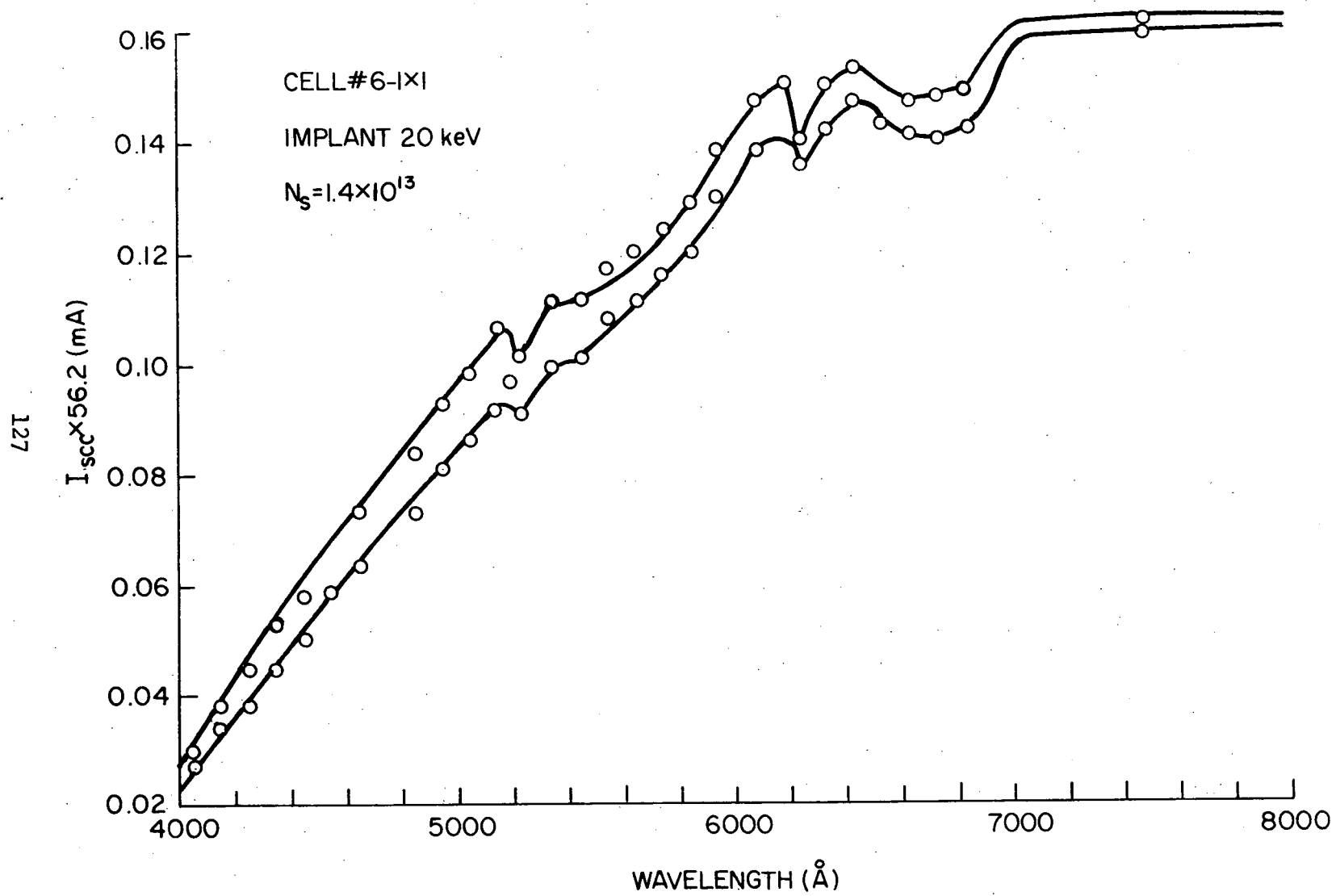
Figure B-2. Spectral response characteristics for 1/4" diameter masked cell before and after implantation.
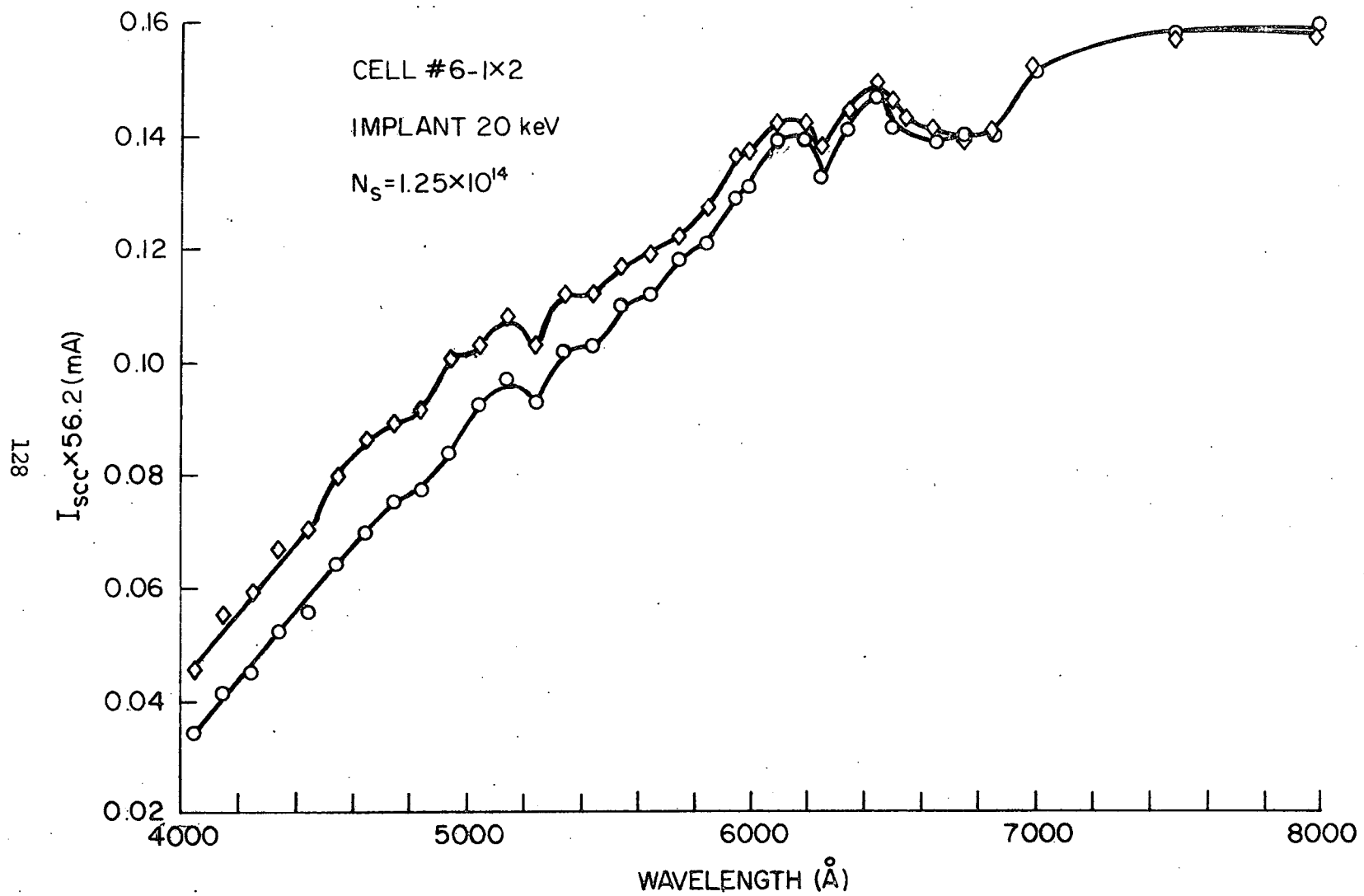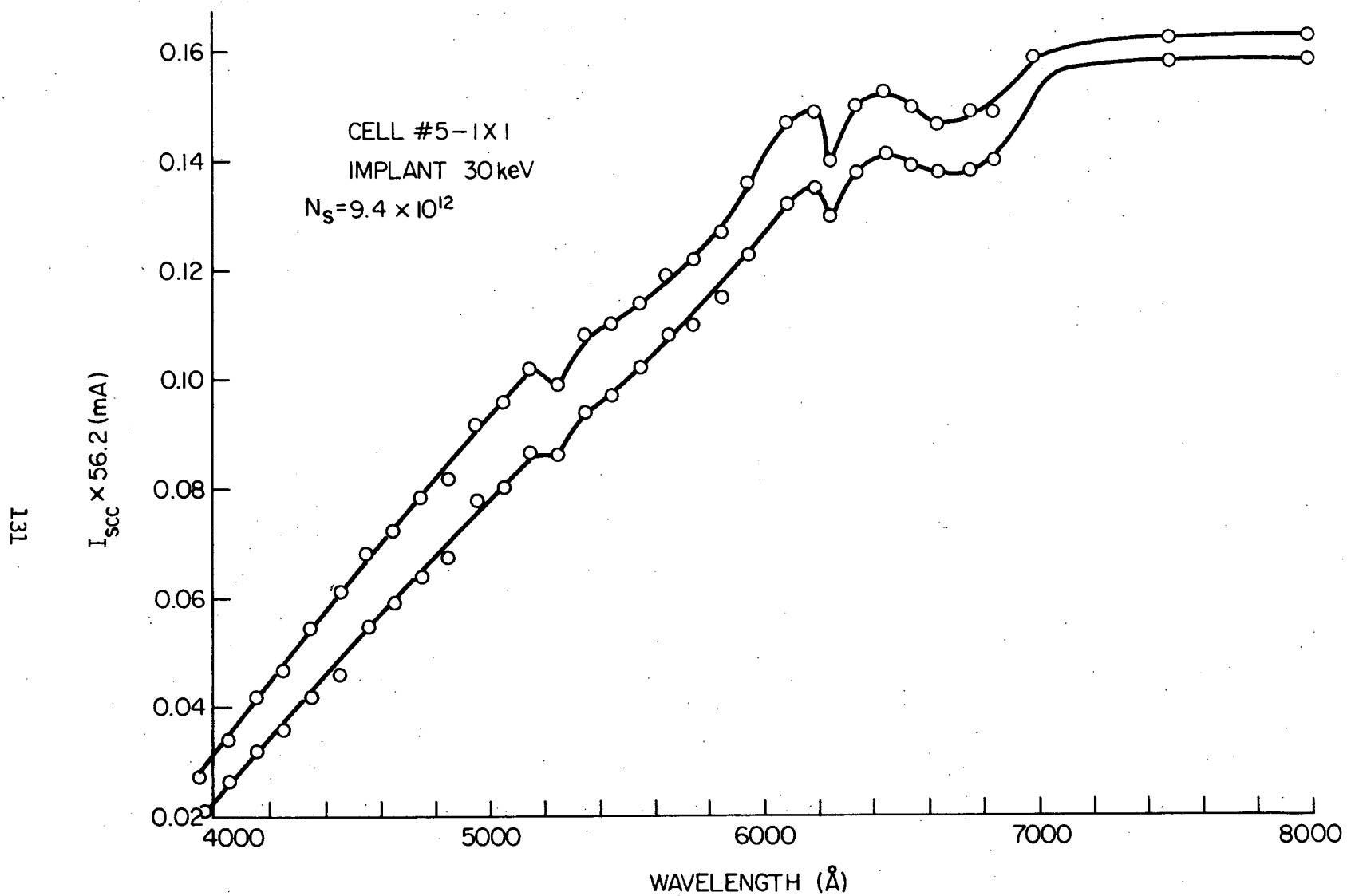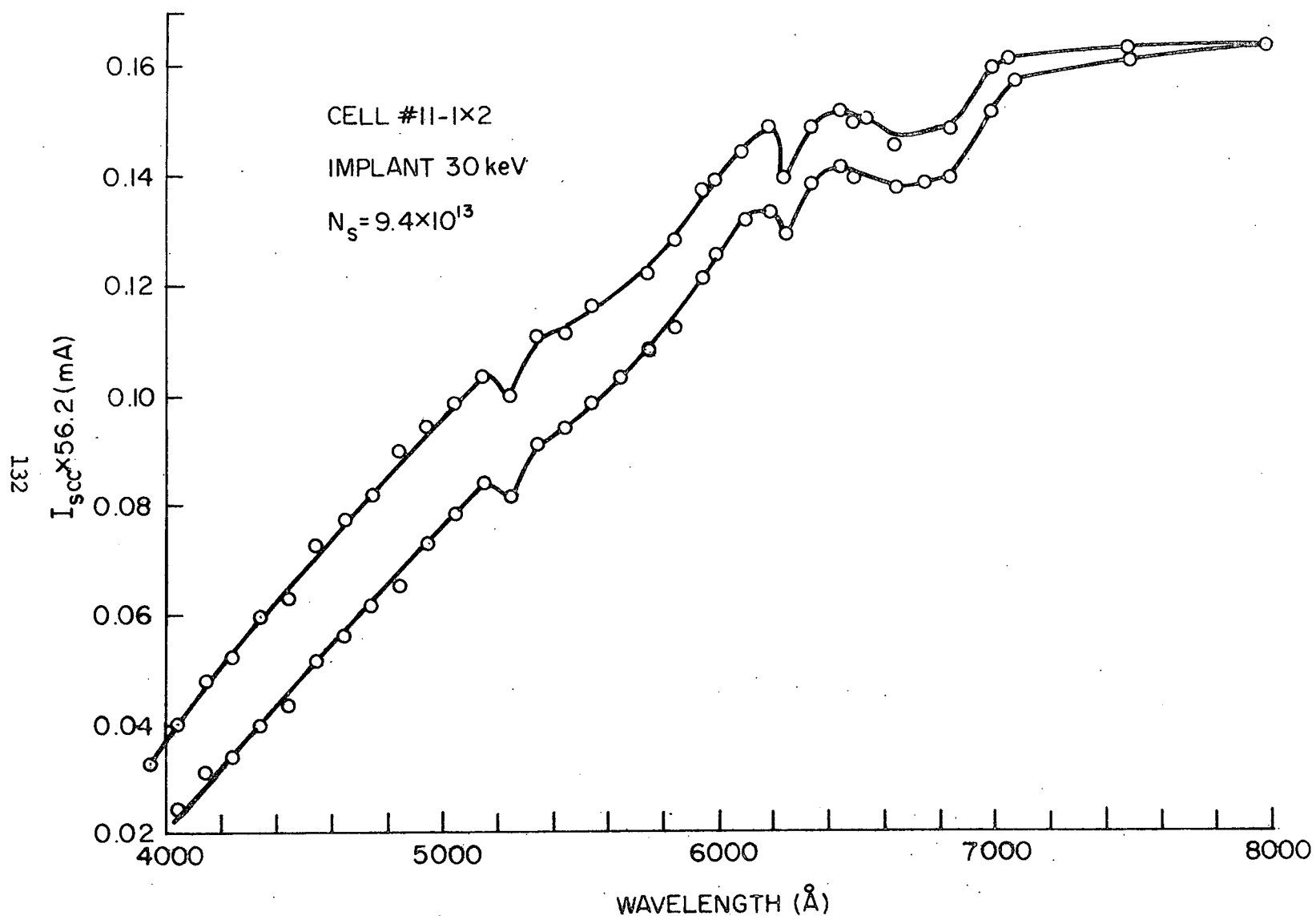
Figure B-3. Spectral response characteristics for 1/4" diameter masked cell before and after implantation.

CELL #8-1×2

IMPLANT 20 keV

$N_S = 1.92 \times 10^{15}$

(y-axis) $I_{scc} \times 56.2$ (mA)

(x-axis) WAVELENGTH (Å)
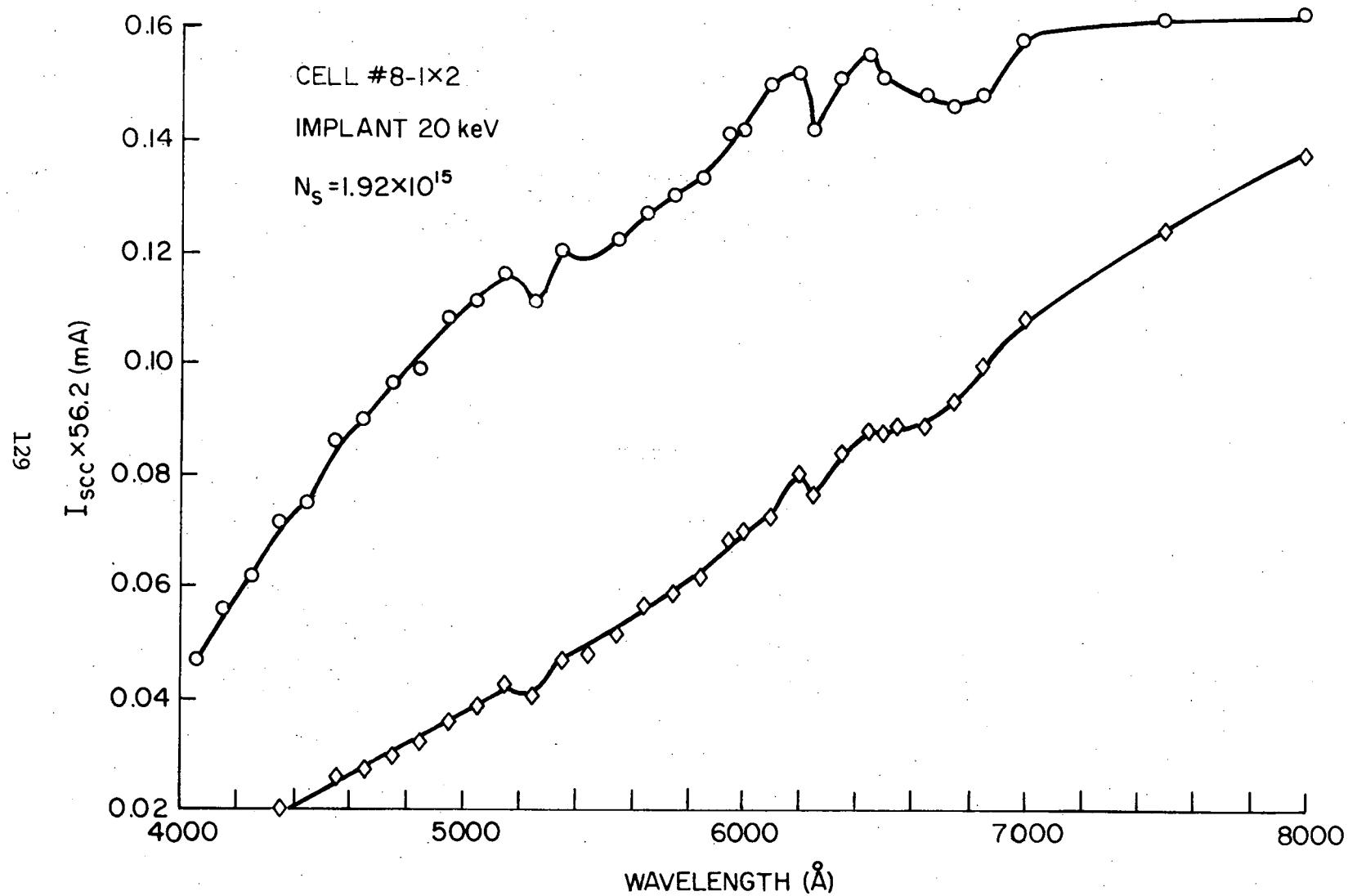
Figure B-4. Spectral response characteristics for 1/4"
diameter masked cell before and after
implantation.
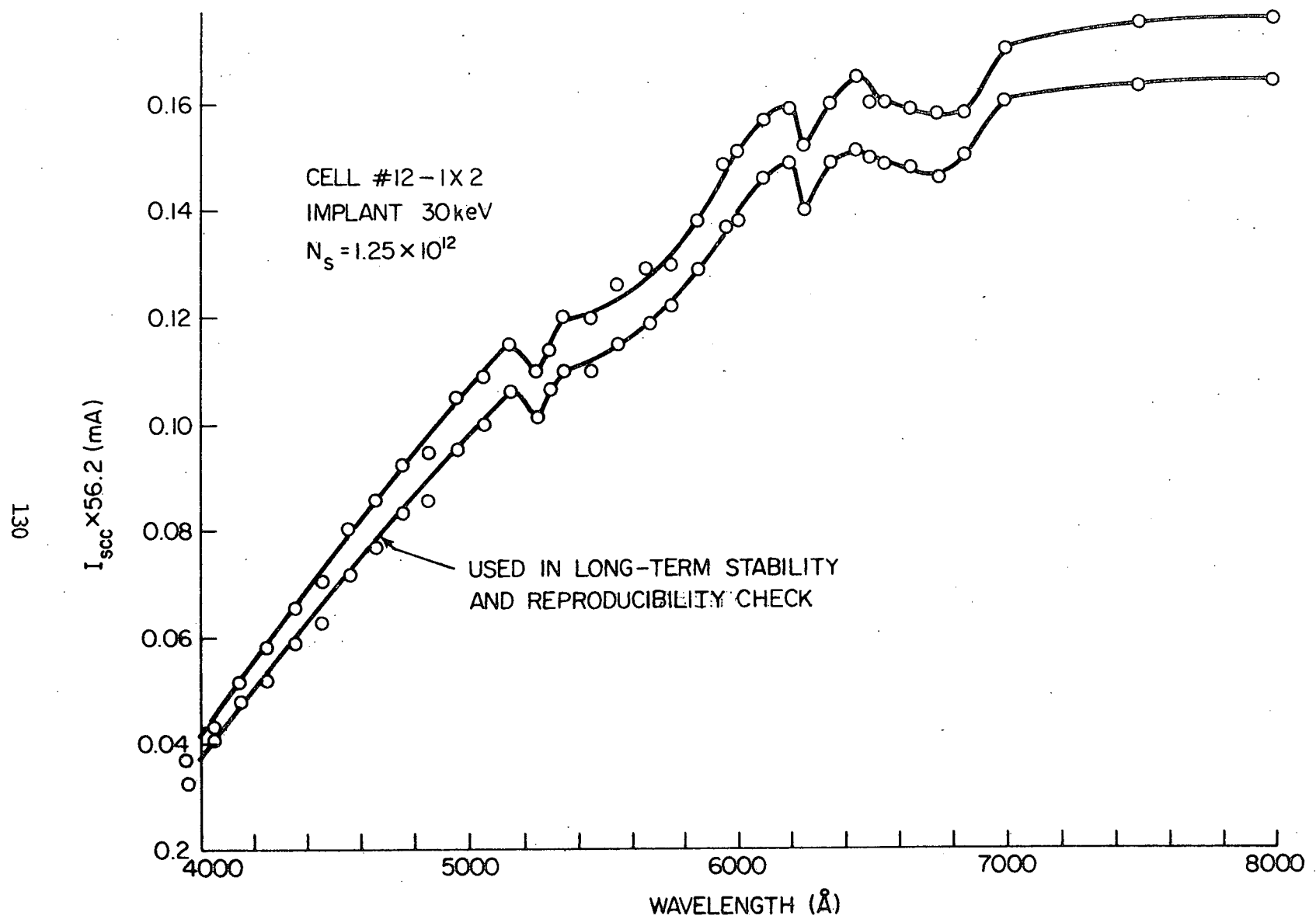
Figure B-5. Spectral response characteristics for 1/4"
diameter masked cell before and after
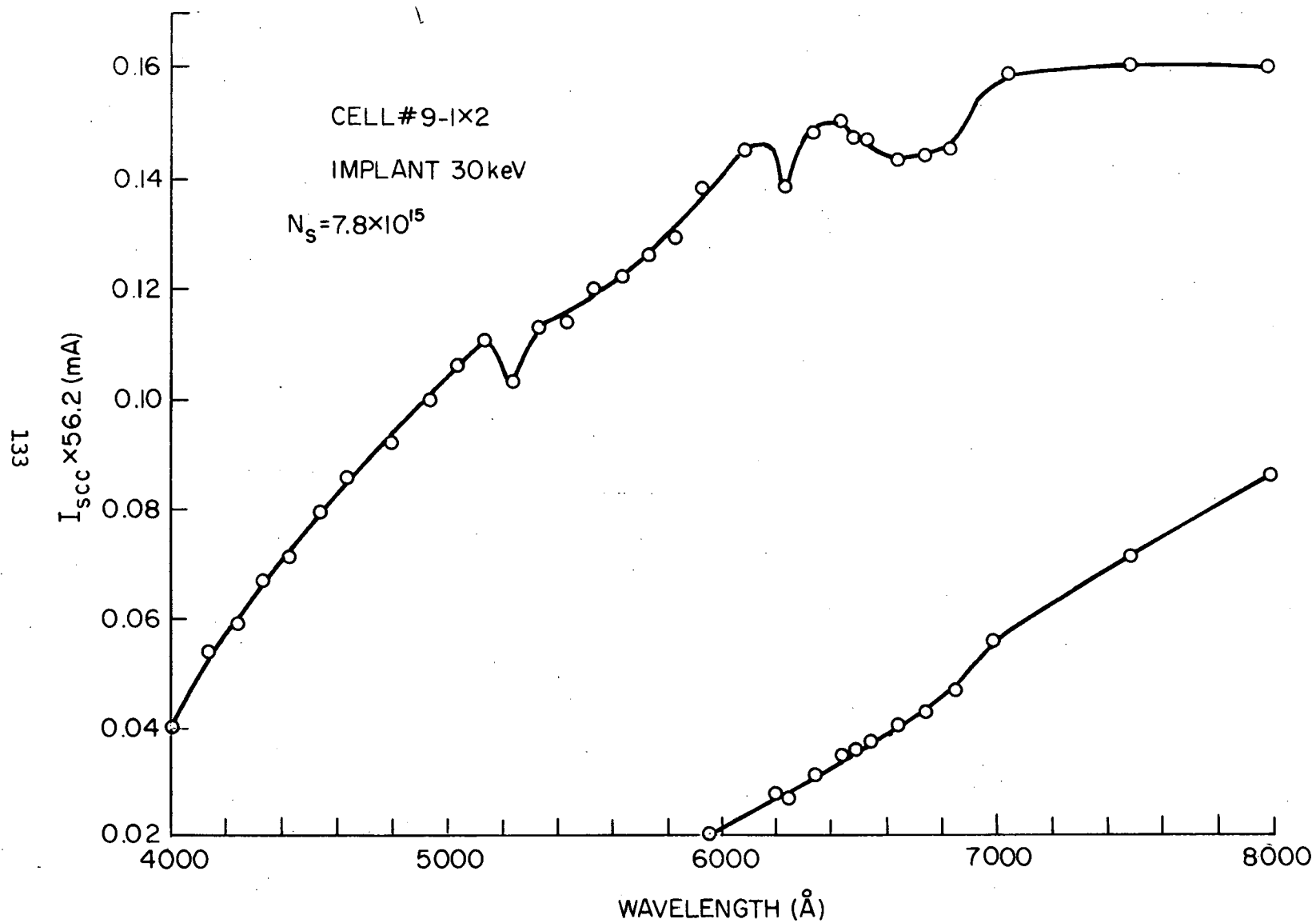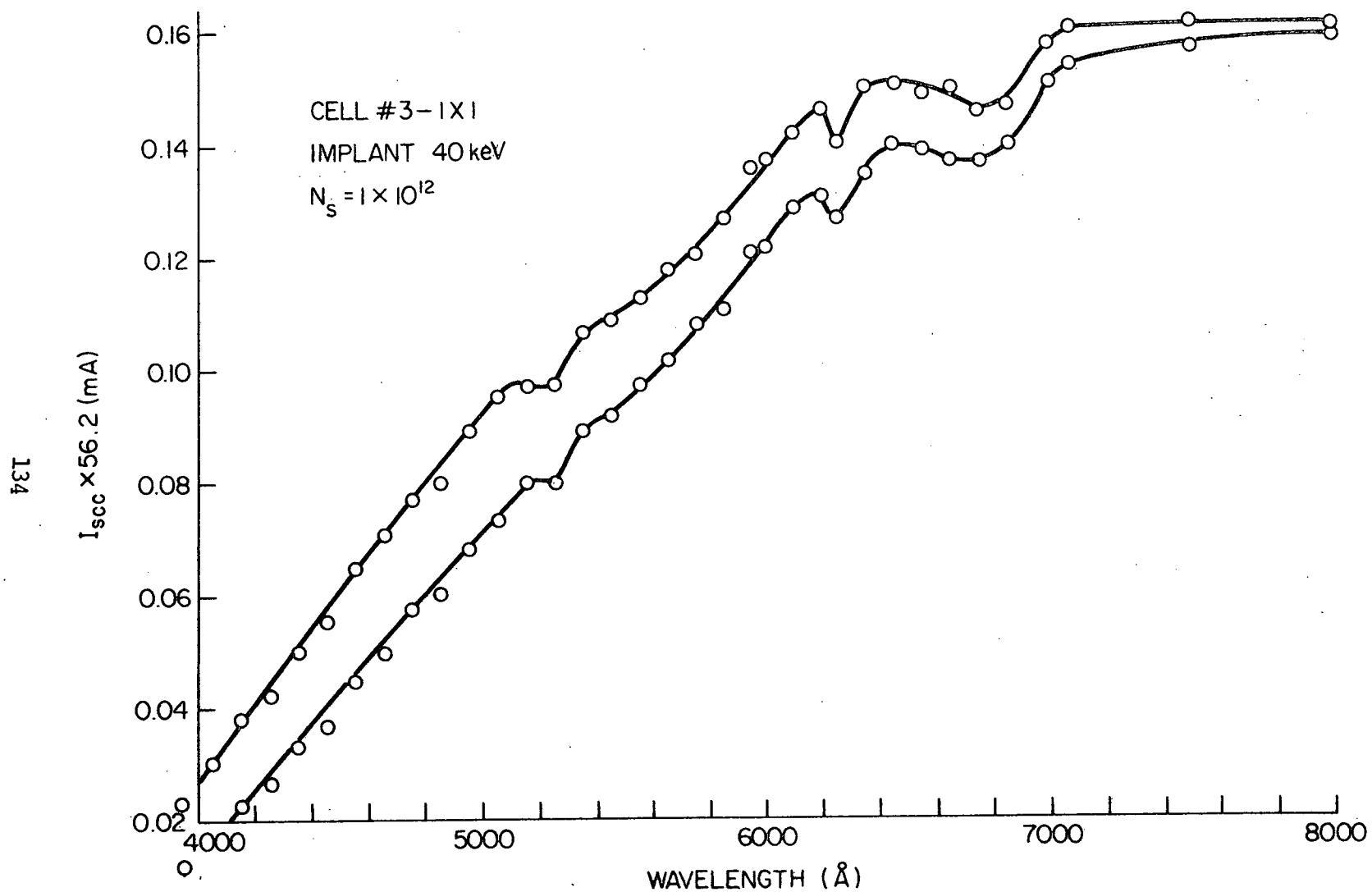implantation.

Figure B-6. Spectral response characteristics for 1/4"
diameter masked cell before and after
implantation.

CELL #11-1×2

IMPLANT 30 keV

$N_s = 9.4 \times 10^{13}$

Figure B-7. Spectral response characteristics for 1/4" diameter masked cell before and after implantation.

132

Figure B-8. Spectral response characteristics for 1/4"
diameter masked cell before and after
implantation.

133

Figure B-9. Spectral response characteristics for 1/4"
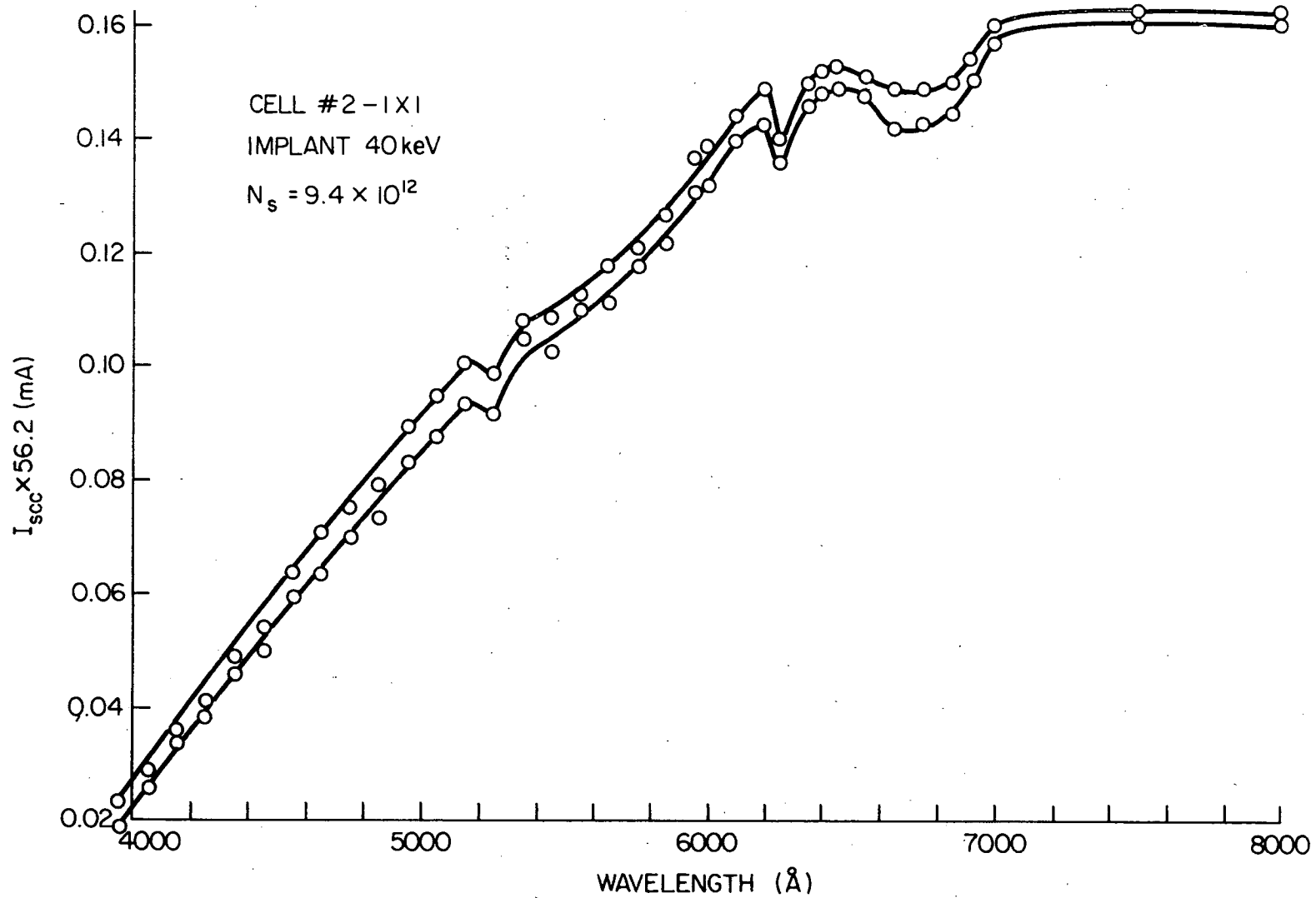diameter masked cell before and after
implantation.

CELL #2 - I X I

IMPLANT 40 keV

$N_s = 9.4 \times 10^{12}$

Figure B-10. Spectral response characteristics for 1/4"
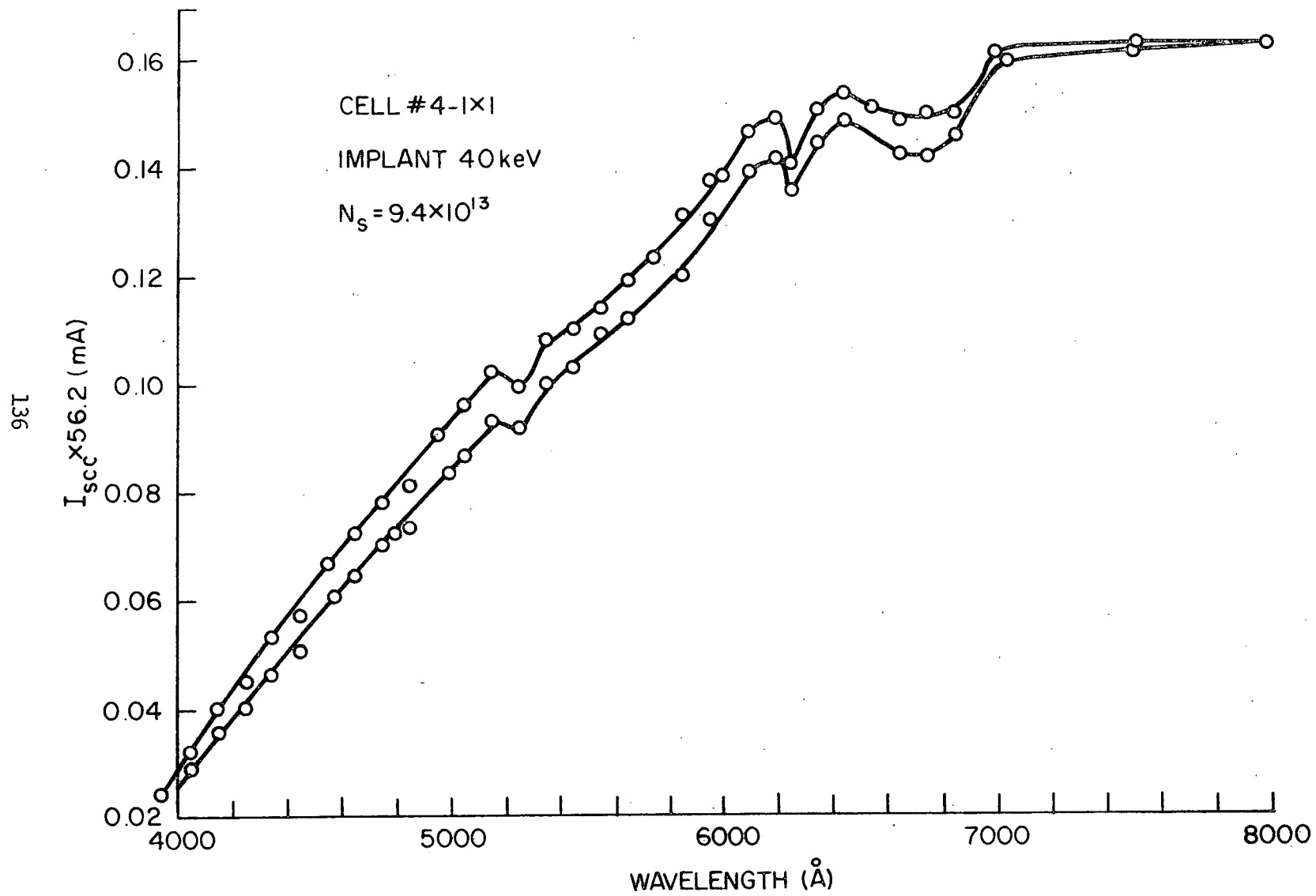diameter masked cell before and after
implantation.

Figure B-11. Spectral response characteristics for 1/4"
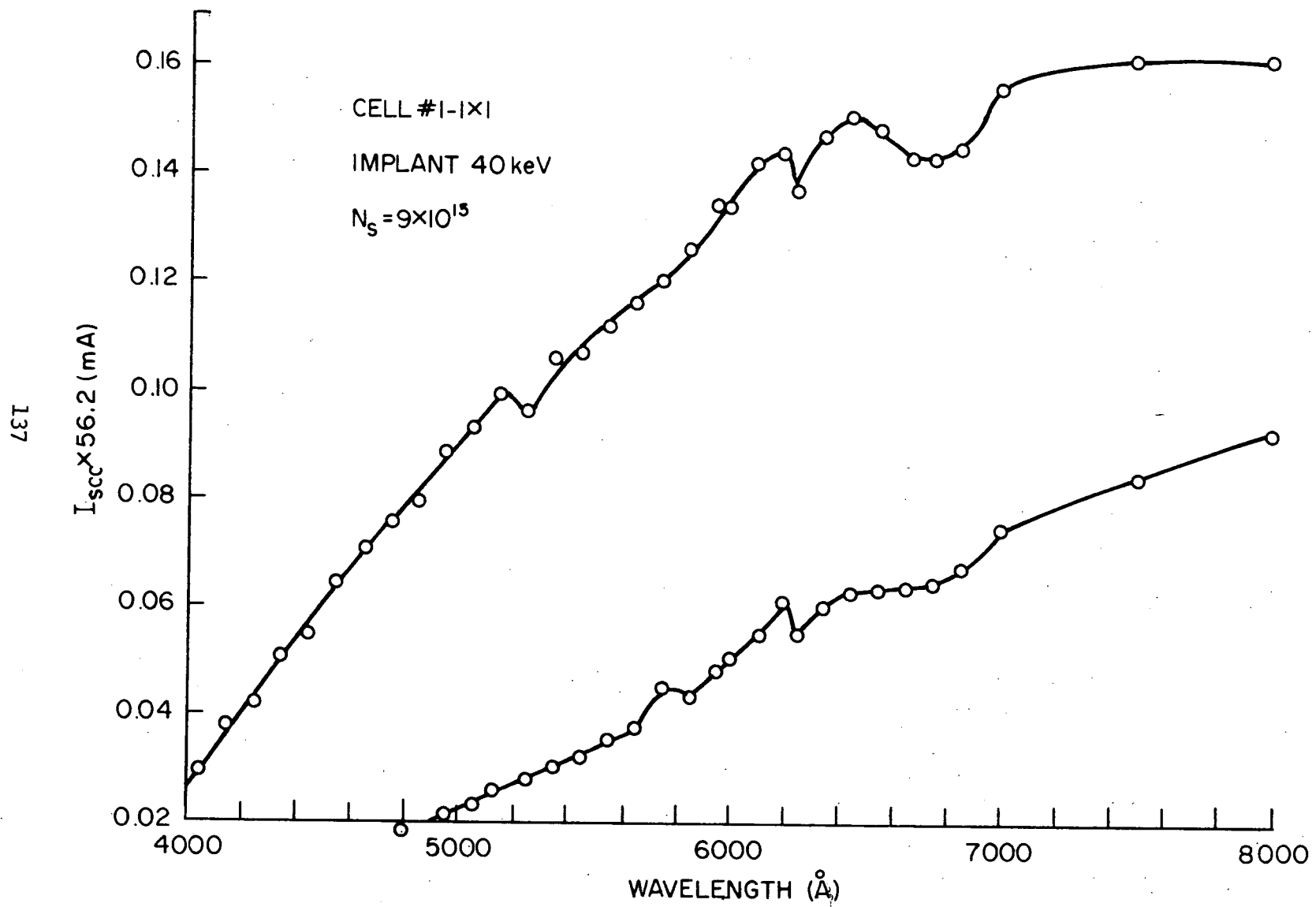diameter masked cell before and after
implantation.

Figure B-12. Spectral response characteristics for 1/4"
diameter masked cell before and after
implantation.